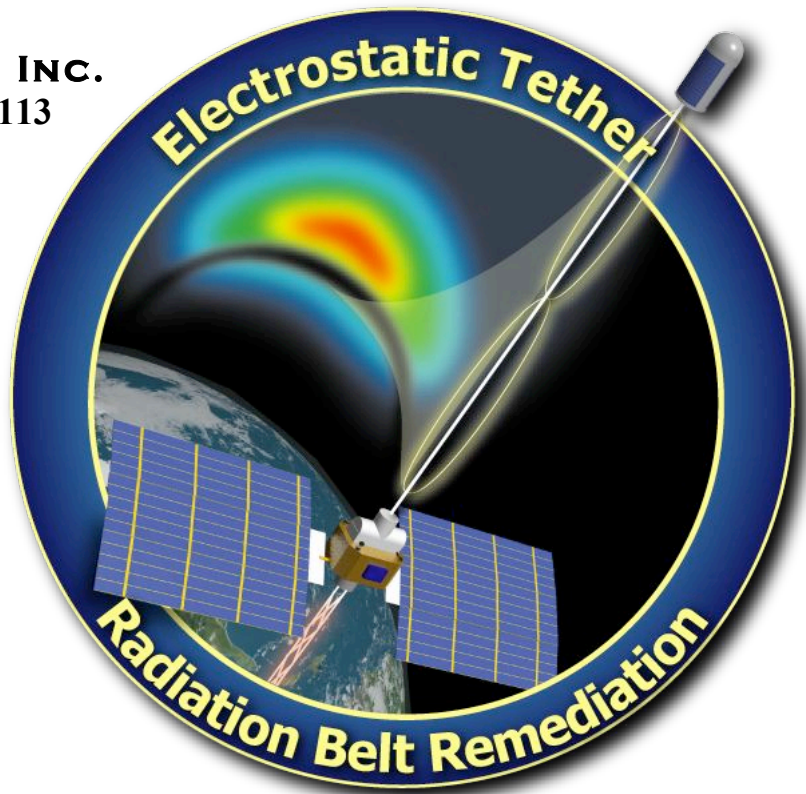


# REDUCTION OF TRAPPED ENERGETIC PARTICLE FLUXES IN EARTH AND JOVIAN RADIATION BELTS

Robert Hoyt  
Michele Cash

**TETHERS UNLIMITED, INC.**  
11711 N. Creek Pkwy S., D-113  
Bothell, WA 98011



1 July 2007

**Final Report**  
Period Covered: 1 September 2006 – 30 June 2007

Subaward 07605-003-061 on Prime Contract NAS5-03110

Prepared for:



**NASA Institute for Advanced Concepts**  
**Universities Space Research Association**  
75 Fifth St NW, Suite 318  
Atlanta, GA 30308

---

## I. ABSTRACT

Using analytical methods and numerical simulations, we investigated the feasibility of using long conducting structures charged to high voltages to remove energetic particles from the radiation belts of Earth and Jupiter. Both approaches indicate that such remediation is feasible, and the number and size of ‘ElectroStatic Radiation Belt Remediation’ (ES-RBR) spacecraft required to reduce electron fluxes in the Earth’s inner electron belt are both very reasonable. A system composed of 24 spacecraft, each of which has a 100-km long, 200-kg tether structure and a power supply on the order of 5 kW, could dramatically lower the radiation doses experienced by spacecraft and personnel flying in low Earth orbit. Investigation of the potential adverse ‘environmental impact’ of such a radiation belt remediation effort indicate that the anticipated side effects on the ozone layer and RF communications will be very mild and short-lived, comparable to a very weak solar storm. Remediation of the Jovian radiation belts is a much more challenging proposition due to its immense spatial extent, but remediation of a narrow band around one of the Galilean moons, such as Europa, may be feasible with a system composed of 100 very high-voltage ES-RBR spacecraft. Because the models used in these analyses rely upon several assumptions regarding the very complex physics of the high-voltage sheaths that form around a multi-wire tether structure in the presence of a plasma, near-term efforts to advance the technology readiness of this concept should focus upon verification of these assumptions through detailed experimental investigation of the size and structure of plasma sheaths around multi-wire structures. Should these investigations validate the models, the ES-RBR concept can then be demonstrated through a relatively low-cost microsat-class flight experiment that would measure the precipitation of energetic electrons into the upper atmosphere caused by a several-kilometer long high-voltage tether structure. The high-voltage, high-power microsat hardware demonstrated in this flight could then serve as a flight-qualified building block for a modular architecture for constructing the two dozen 100-km long electrostatic structures required for an operational ES-RBR system. By dramatically reducing radiation fluxes in the LEO environment, such an ES-RBR system could enable satellites to be built using lower cost, higher performance components while still providing reliable operations on orbit, could enable reusable high-performance solar-electric propulsion tugs to survive repeated transits through the Van Allen belts, and could reduce health risks for manned spaceflight missions in LEO and beyond.

**TABLE OF CONTENTS**

<b>I.</b>	<b>ABSTRACT .....</b>	<b>i</b>
<b>II.</b>	<b>INTRODUCTION.....</b>	<b>1</b>
II.A.	The Radiation Belts.....	1
II.B.	Effects on Spacecraft and Personnel.....	2
II.C.	Prior Work on Radiation Belt Remediation.....	2
<b>III.</b>	<b>ELECTROSTATIC REMEDIATION CONCEPT.....</b>	<b>3</b>
III.A.	Electrostatic Remediation System Concept.....	4
III.B.	Plasma Sheath Effects and the Multi-Wire Tether Concept.....	6
<b>IV.</b>	<b>ELECTROSTATIC REMEDIATION SYSTEM SCALING .....</b>	<b>8</b>
IV.A.	Radiation Flux Decay.....	8
IV.B.	Plasma Sheath Size.....	10
IV.C.	Plasma Flow Effects on Sheath Size.....	11
IV.D.	Depletion Efficiency.....	12
<b>V.</b>	<b>USING MULTI-WIRE STRUCTURES TO MINIMIZE ES-RBR SYSTEM SIZE AND POWER .....</b>	<b>16</b>
V.A.	Electrostatic Tether System Power.....	16
V.B.	OML Current.....	16
V.C.	Electron Emission Due to Ion Bombardment.....	17
V.D.	The Multi-Wire Tether Concept.....	18
V.E.	Plasma Density.....	22
V.F.	ES-RBR System Power.....	22
V.G.	System Sizing for Earth and Jovian Radiation Belts.....	23
<b>VI.</b>	<b>TETHER-PARTICLE INTERACTION FREQUENCY .....</b>	<b>26</b>
VI.A.	Particle Motion.....	26
VI.B.	Particle Sample.....	27
VI.C.	Tether Motion.....	27
VI.D.	Interaction Model.....	27
VI.E.	Analysis.....	30
<b>VII.</b>	<b>ENERGETIC PARTICLE DECAY CALCULATIONS.....</b>	<b>31</b>
VII.A.	Initial Particle Flux.....	32
VII.B.	Tether Orbit.....	33
VII.C.	Magnetic Flux Tubes.....	34
VII.D.	Interaction Rate.....	35
VII.E.	Pitch Angle Scattering.....	36
VII.F.	Particle Decay Rate.....	37
<b>VIII.</b>	<b>RADIATION REMEDIATION SIMULATIONS .....</b>	<b>40</b>
VIII.A.	Tether Orbits.....	40
VIII.B.	Electron Decay Rate.....	40
VIII.C.	Proton Decay Rates.....	49
<b>IX.</b>	<b>EVALUATION OF ENVIRONMENTAL EFFECTS OF ELECTROSTATIC REMEDIATION OF THE INNER ELECTRON BELT .....</b>	<b>52</b>
IX.A.	Increased Particle Precipitation.....	52
IX.B.	Summary of Environmental Impact Assessment.....	60
<b>X.</b>	<b>TECHNOLOGY DEVELOPMENT AND VALIDATION PLAN .....</b>	<b>61</b>
X.A.	Model Uncertainties.....	61
X.B.	Phase A: Verification of Multi-Wire Sheath Potential Structure Model.....	61
X.C.	Technology Development.....	62
X.D.	Phase B: On-Orbit Demonstration of Electron Precipitation by an Electrostatic Structure.....	62
<b>XI.</b>	<b>CONCLUSIONS .....</b>	<b>65</b>

## TABLE OF FIGURES

Figure 1. The dipole structure of the geomagnetic field traps energetic particles in the Van Allen Belts....	1
Figure 2. Concept of operations of an electrostatic system deployed to reduce radiation fluxes in the inner electron Van Allen belt. ....	3
Figure 3. Conceptual configuration of an electrostatic remediation system, showing current balance. ....	4
Figure 4. Concept for a modular architecture for an ES-RBR high-voltage structure system. ....	5
Figure 5. Use of a multi-wire array can enable a larger plasma sheath, with stronger electric fields, to be generated around an electrostatic structure without increasing the bias potential. ....	7
Figure 6. The geometry of the interaction of the electrostatic tether and the radiation belt. ....	8
Figure 7. Variation of the sheath size with bias potential, and probe size calculated by Choinière using his KiPS-1D and KiPS-2D models for plasmas with no flow velocity. ....	11
Figure 8. Schematic of the simplified scattering analysis. ....	12
Figure 9. “Top-hat” pitch angle distribution. ....	14
Figure 10. Variation of total system power with tether voltage <i>for a single-wire tether</i> . ....	18
Figure 11. Illustration of increasing the sheath size and intensity through either increasing the tether voltage or adding additional wires at the same voltage. ....	19
Figure 12. Concept design for a stowable multiline electrostatic tether structure. ....	19
Figure 13. Equipotential contours within the sheath of a 25-wire tether structure. ....	21
Figure 14. Plasma densities predicted by the Global Core Plasma Model for Local Magnetic Noon for 1 June 2002. ....	22
Figure 15. Variation of plasma sheath radius around the electrostatic structure with applied bias voltage. ....	23
Figure 16. Number of ES-RBR systems required to remediate Earth’s inner belt to 1% of original flux within 30 days, as a function of bias voltage. ....	23
Figure 17. Variation of plasma sheath radius around the electrostatic structure with applied bias voltage. ....	24
Figure 18. Number of ES-RBR systems required to remediate a 12,000-km wide section of Jupiter’s radiation belt around Europa’s orbit to 1% of original flux within 90 days, as a function of bias voltage. ....	24
Figure 17. Average number of tether interactions (left) for 1 MeV electrons, (right) in 1 day. ....	29
Figure 18. Average number of tether interactions (left) for 10 MeV protons, (right) in 1 day. ....	30
Figure 19. Illustration of the models combined in the ES-RBR simulation tool. ....	31
Figure 20. Equatorial electron flux profile in the inner belt region. ....	33
Figure 21. Flux tube locations w.r.t. magnetic field lines at L=1.3, 1.5, and 1.7. ....	34
Figure 22. 25 Electrostatic tether structures in orbit around the Earth. ....	35
Figure 23. Evolution of an initial ‘top-hat’ pitch angle distribution for a 10% interaction rate for equal time steps. ....	37
Figure 24. Number of particles removed from the belt at each time step. ....	37
Figure 25. Decay of particle fluxes in the inner belt region for all L-shell values combined. ....	38
Figure 26. Decay of particle fluxes in the inner belt region for discrete L-shell values. ....	38
Figure 27. Linear least-squares fit (red dashed line) for the decay of energetic particles in the radiation belts. ....	39
Figure 28. Decay Rate for Electrons in the Radiation Belts (L=1.3 to 1.7), Natural Source and Sink Terms Not Included. ....	41
Figure 29. Linear Least Squares Fit (red dashed line) for the Decay of Energetic Electrons in the Radiation Belts. ....	42
Figure 30. Decay Rate for Electrons in the Radiation Belts (L=1.3 to 1.7), Natural Sink Terms Included, Source Terms Not Included. ....	43
Figure 31. Linear Least Squares Fit (red dashed line) for the Decay of Electrons in the Radiation Belts due to Natural Loss (blue line) and Remediation (black line). ....	43
Figure 32. Logarithmic Value of the 2-6 MeV Daily Averaged Electron Fluxes from July 2002 to March 2004 (in $\text{cm}^{-2} \text{s}^{-1} \text{sr}^{-1} \text{MeV}^{-1}$ ) ....	44
Figure 33. Logarithmic Value of the 2-6 MeV Daily Averaged Electron Fluxes from Jan 2000 to March 2004 (in $\text{cm}^{-2} \text{s}^{-1} \text{sr}^{-1} \text{MeV}^{-1}$ ) ....	44
Figure 34. Electron flux in the inner belt region during a solar active period, natural source and sink terms included. ....	45

Figure 35. Electron fluxes in the inner belt during a solar quiet period, without remediation. .... 46

Figure 36. Electron fluxes in the inner belt during a solar quiet period, with ES remediation. .... 46

Figure 37. Electron fluxes in the inner belt during a solar active period, without remediation. .... 47

Figure 38. Electron fluxes in the inner belt during a solar active period, with ES remediation..... 47

Figure 39. Electron fluxes in the inner belt measured by SAMPEX during the Spring 2001 storm. .... 48

Figure 40. Electron fluxes in the inner belt during the Spring 2001 storm, with ES remediation. (note color scale is different than in Figure 37)..... 48

Figure 41. Decay of protons in the inner belt region (L=1.3 to 1.7), with ES remediation but no source or sink terms. .... 49

Figure 42. Linear least-squares fit (red dashed line) for the decay of energetic protons in the radiation belts..... 49

Figure 43. Decay rate for protons (L=1.3 to 1.7) during solar quiet periods, natural sink terms included. 50

Figure 44. Linear Least Squares Fit (red dashed line) for the Decay of Protons in the Radiation Belts due to Natural Loss (blue line) and Remediation (black line). .... 50

Figure 45. Proton fluxes in the inner belt region during solar quiet period, with no remediation. .... 51

Figure 46. Proton fluxes in the inner belt region during solar quiet period, with ES remediation. .... 51

Figure 47. Localized increase in precipitation flux resulting from initial radiation belt remediation..... 55

Figure 48. Increase in precipitation flux averaged over 26 hours and L-shell area resulting from initial radiation belt remediation. .... 56

Figure 49. Natural precipitation flux (solid line) and combined precipitation flux (dotted line) plotted at four times during initial radiation belt remediation. .... 57

Figure 50. Decay of particle precipitation flux with time (dotted line) during radiation belt remediation for two L- values. The current, natural radiation belt precipitation flux is plotted with a solid line. . 58

**Figure 51.** Percent change in L-shell averaged precipitation rate for initial radiation belt remediation. .... 59

Figure 52. Concept for electron-beam tomography method to determine the potential structure inside a multi-wire electrostatic structure’s plasma sheath. .... 61

Figure 53. Mission concept for a “Tethered Orbit-Raising & Radiation Remediation QQualification Experiment” (TOR<sup>3</sup>QUE). .... 62

Figure 54. Detection of electron precipitation due to an electrostatic tether structure using the TRIMPI effect. .... 63

Figure 55. Example of a flux tube precipitating electrons will follow after scattering by an ES tether in a 28.5° orbit. .... 63

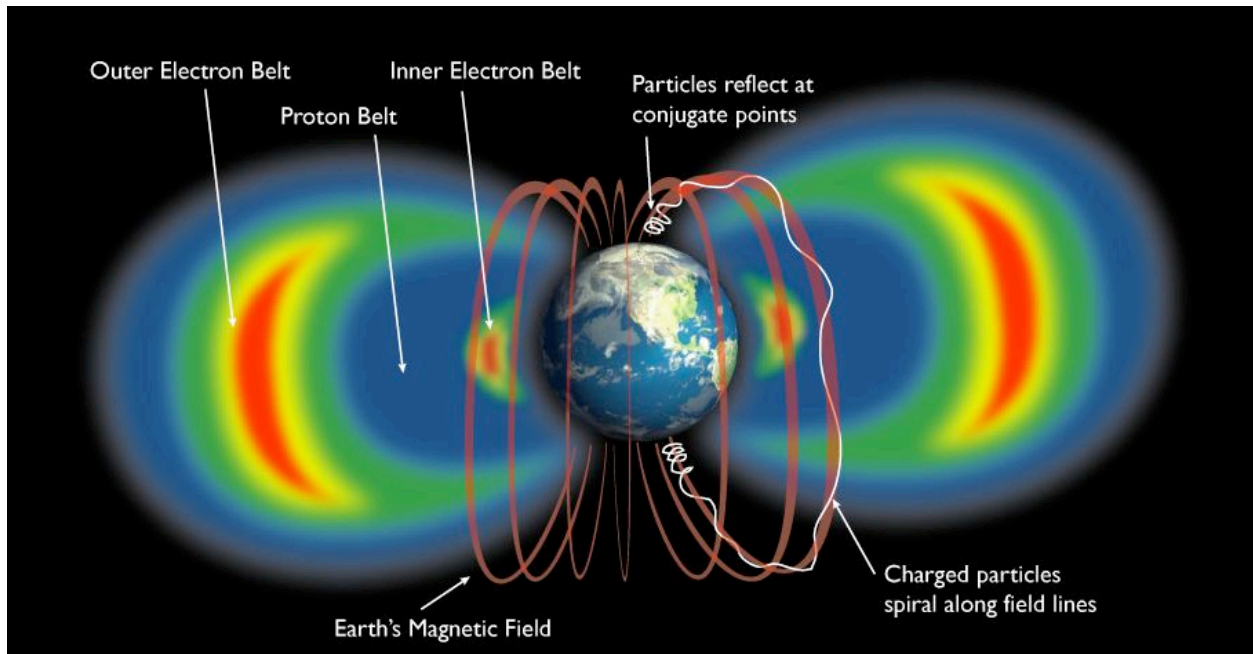
Figure 56. Precipitation tracks (red) that would be expected from a tether orbiting in a 28.5° orbit (yellow). .... 63

Figure 57. Principle of TRIMPI effect detection of electron precipitation ..... 63

## II. INTRODUCTION

### II.A. The Radiation Belts

The magnetic fields of planets such as Earth and Jupiter have a dipole structure that acts as a “magnetic bottle” to trap intense fluxes of energetic charged particles in regions near the planet, as illustrated in Figure 1. Due to the influence of the geomagnetic field, charged particles spiral along the magnetic field lines. As they approach the polar regions where the field lines converge, the increasing magnetic field strength causes their velocity perpendicular to the field lines to increase and their velocity along the field lines to decrease. Those particles that start out at the magnetic equator with a pitch angle greater than a certain value, called the “loss cone angle”, will reflect before they enter the upper atmosphere. As a result, these particles are trapped within crescent-shaped regions of space around the Earth, continually bouncing between the polar conjugate points many times per second. Within these regions, commonly referred to as the Van Allen Radiation Belts, energetic electrons and ions generated through natural and man-made events can persist for many months or years. These high-energy particles pose a significant threat to missions in Earth orbit, degrading electronics and materials in spacecraft systems and causing biological damage in personnel in space. The costs associated with hardening electronics and launching the heavy shielding required to enable humans and electronics to survive and perform reliably in the radiation environment are a major driver in the high costs and risks of space missions.



**Figure 1.** The dipole structure of the geomagnetic field traps energetic particles in the Van Allen Belts.

The mechanisms whereby these charged particles are created and/or injected and become trapped in the radiation belts are complex and not fully understood. The standard theory has been that solar wind particles injected into the magnetosphere through solar storm mechanisms and charged particles created through collisions of cosmic rays with atmospheric particles are accelerated to multi-megavolt energies as they diffuse radially in towards the planet. More

recently, however, the Cluster spacecraft has observed phenomena that indicate that the particles may be accelerated to MeV energies by very low frequency (VLF) waves with frequencies of a few kilohertz propagating in the whistler mode.<sup>1</sup>

## II.B. Effects on Spacecraft and Personnel

Energetic particles with energies greater than about 1 MeV pose a severe threat to spacecraft systems. These energetic particles will steadily degrade electronics, optics, solar panels, and other critical systems by breaking chemical bonds, disrupting crystalline and molecular structures, and by causing localized charge effects. Higher energy particles can cause single-event disruptions or damage to electronics. Spacecraft systems operating in Earth orbit must be hardened to withstand this radiation environment, and typically their electronics must be designed with several layers of redundancy, incurring significant expense and additional mass. Moreover, because microprocessors with very small feature sizes are more susceptible to damage and single-event upsets, space systems typically cannot take advantage of the newest, highest-performance electronics, and instead must rely upon older technologies with larger feature sizes and significantly lower performance. The radiation particles also pose a significant threat to personnel and other biological systems in Earth orbit. As they pass through tissue, they can deposit their energy by ionizing water and proteins, causing cellular damage, modifying DNA, RNA, and proteins in ways that can lead to cancers, immune system disorders, and other maladies. Protecting personnel in space from energetic particles in the MeV range requires a great deal of extra mass for shielding; a 1996 NRC study concluded that the shielding mass required to protect astronauts during a Mars expedition could add \$10B to \$30B to the cost of the mission.<sup>2</sup> The presence of the Van Allen belts requires that manned and unmanned spacecraft traveling to the Moon, Mars, or anywhere above LEO must make the transit through the altitude regions affected by the belts as rapidly as possible to avoid disastrous damage to people, solar panels, and electronics. As a result, many advanced transportation concepts, such as solar electric tugs,<sup>3</sup> solar thermal rockets, and other high-specific impulse systems, which could otherwise greatly reduce the total costs of transporting people and payload to the Moon and other planets, are currently not viable options for the Earth-escape portion of manned missions.

## II.C. Prior Work on Radiation Belt Remediation

One potential method of reducing the dangers of radiation for missions in Earth and Jovian orbit is to deplete the radiation belts by accelerating the rate at which the particles precipitate into the planets' upper atmospheres. The natural lifetimes of particles in the radiation belts are on the order of 100's to 1000's of days. If these lifetimes can be greatly reduced, the average fluxes of trapped particles can also be reduced. To date, the leading concept proposed for increasing the loss rate of the radiation belts and lowering their average intensity has been to use high power VLF (kilohertz frequency) electromagnetic waves. It is known that lightning storms, which generate VLF waves in the ionosphere and above, cause "precipitation" of electrons out of the electron belts. It is hypothesized that the VLF waves cause these electrons to leave the belts by

- 
1. Horne, R.B. *et al.*, "Wave acceleration of electrons in the Van Allen radiation belts," *Nature*, 437(8) Sept 2005, pp 227-230.
  2. *Florida Today Space Online*, Dec 18, 1996.
  3. Fitzgerald, A. "The Effect of Solar Array Degradation in Orbit-Raising with Electric Propulsion," AIAA Paper IEPC-93-207, 23rd International Electric Propulsion Conference, Sept. 1993.

scattering their trajectories, causing some of them to have pitch angles that will result in reflection points inside the Earth's atmosphere so that they will be decelerated through collisions with atmospheric particles. The multi-\$M HAARP facility in Alaska has been developed in part to investigate this mechanism. Detailed analyses of the efficiency of this method, however, indicate that the concept is not likely to be economically feasible if performed from the ground. Some researchers have claimed that spaceborne antennas could affect dramatic reductions in trapped particle lifetimes with total powers as low as 13 Watts,<sup>4</sup> but the VLF frequencies and modes they propose to use to cause electron precipitation are in the same frequency range as those the Cluster spacecraft observations showed *cause* the creation of the MeV electrons!

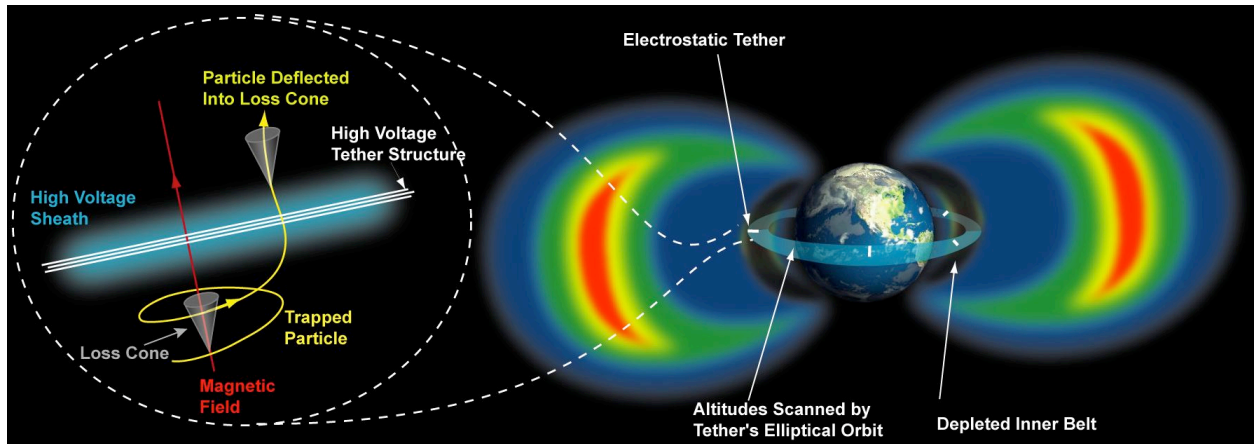


**Figure 2.** Concept of operations of an electrostatic system deployed to reduce radiation fluxes in the inner electron Van Allen belt.

### III. ELECTROSTATIC REMEDIATION CONCEPT

In this Phase I effort, we have investigated the feasibility of using a system of multiple long, high-voltage structures deployed in orbit to cause dramatic reductions in the radiation fluxes in the Van Allen belts. The “Electrostatic Radiation Belt Remediation” (ES-RBR) system, illustrated in Figure 2, would deploy several long tether structures in low-inclination orbits. The tether lengths contemplated are typically in the range of 10-100 km, and each tether structure would be composed of multiple parallel conducting wires, spread apart in a cylinder with a diameter on the order of 20 meters. The eccentricity of the tethers’ orbits would be chosen so that the tethers will scan the altitudes affected by the radiation belt that must be remediated. Once the tethers are deployed, gravity-gradient forces will align them along the local vertical direction, orienting them perpendicular to the magnetic field lines and thus (roughly) perpendicular to the flow of energetic particles. The remediation system will then charge the tether structures to a large negative voltage relative to the local quiescent plasma potential. The voltage will create an intense electric field around the tether. As the trapped radiation particles spiraling along the magnetic field lines pass through the high voltage region near the tether, the tether’s electric field will deflect the charged particles, changing their pitch angle, as illustrated in Figure 2.

4. Inan, U.S., *et al.*, “Controlled Precipitation of Radiation Belt Electrons,” *J. Geophys. Res.*, 108(A5), 2003, p. 1186.

Because the electric field is a central force, the particle will leave the tether's field with the same kinetic energy as it arrived, so no net energy is transferred between the tether and the particle, but the relative angle between the particle's velocity and the geomagnetic field will be changed. The particle's pitch angle has an equal chance of being increased or decreased by the interaction. The depletion of the energetic particle population is thus a diffusive process, in which it may require many interactions between a given particle and the tether to get the particle's pitch angle to "random walk" into the loss cone. Nearly all of those particles whose pitch angle is reduced below the loss cone angle will leave the radiation belt within a bounce period and dissipate their energy through collisions with atmospheric particles.

The concept of using high-voltage wires to influence the radiation belts originated with work performed by Danilov that indicated that wires charged to thousands or millions of volts could produce significant precipitation of electrons from the Van Allen Belts.<sup>5</sup> Robert L. Forward proposed deploying a number of such high-voltage wires to remediate the intense artificial radiation belts that would be caused by a high-altitude nuclear detonation (HAND).<sup>6</sup> In subsequent analysis, Hoyt and Minor found that the single-wire approach proposed by Danilov would require an impractically large voltages (megavolts) and power levels (many gigawatts) to effect a rapid remediation of a HAND belt, but that a multi-wire structure, charged to more reasonable (but still challenging) levels on the order of 100 kV could perform the task with an economically viable total power requirement.<sup>7</sup>

### III.A. Electrostatic Remediation System Concept

Although negligible net energy is transferred between the tether and the relativistic particles in the radiation belt, the presence of the low density cold plasma at the altitudes within the radiation belts will result in current flows in the electrostatic tether structure that will require expenditure of power in order to sustain the voltages applied to the tether. As illustrated in Figure 3, the large negative voltages on the tether will attract ions from the plasma to the tether. In order to prevent these ions from neutralizing the voltage on the tether, each satellite in the system must continually feed electrons to its electrostatic tether. In order to do so, the system will deploy an anode structure opposite to the electrostatic tether. This anode will be charged to a positive voltage to collect electrons from the plasma. Because electrons are far more mobile than ions, a shorter length of tether charged to a relatively low bias can collect the same magnitude

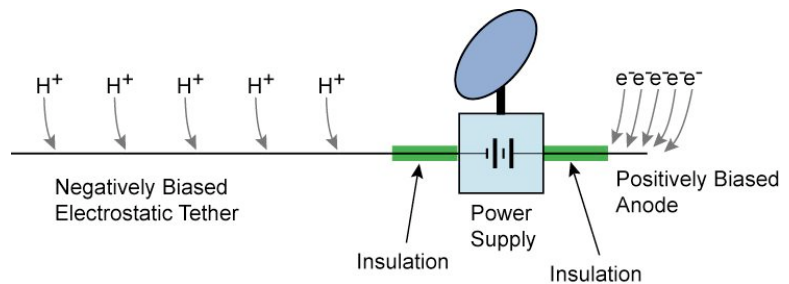


**Figure 3.** Conceptual configuration of an electrostatic remediation system, showing current balance.

5. Danilov, V.V., *et al.*, "High-Voltage Satellite Tethers for Active Experiments In Space", *6th Spacecraft Charging Technology Conference*, AFRL-VS-TR-20001578 (1 September 2000).
6. Forward, R.L., "Radiation Belt Remediation Concepts for AFRL Space Capabilities Protection Study" January 2002.
7. Hoyt, R.P., Slostad, J.T., Minor, B.M., Voronka, N.R., *Electrodynamic/Electrostatic Tether Performance Assessment Program – Tether Payloads Concept Design*, Tethers Unlimited, Inc. final report on DARPA/SPO Seedling contract, 15 Sept 2003.

of electron current as the negatively charged tether at higher bias.<sup>8</sup> The length of the anode section of tether and bias voltage applied to it will be chosen so as to provide the desired negative bias on the electrostatic tether while maintaining the main spacecraft bus as close as possible to the local plasma potential. The “current loop” in the system is expected to be closed by a system of plasma waves as in an electrodynamic tether system.<sup>9</sup> Electrodynamic forces resulting from interactions of the tether current with the geomagnetic field will result in slow changes to the tether’s orbit, raising or lowering it depending upon whether the electrostatic tether is deployed above or below the power supply. This boost/deboost thrust could be used to help the system scan through the altitudes affected by the radiation belt.

### Modular System Design

The nature of the Electrostatic Structure concept makes it readily amenable to implementation using a highly modular architecture, wherein these many-kilometer long structures can be created by combining a number of identical smaller modules in series. In this modular architecture, illustrated in Figure 4, each module would consist of a microsatellite-class bus, a solar power collection system, a tether deployment system, and a multi-kilometer lengths of

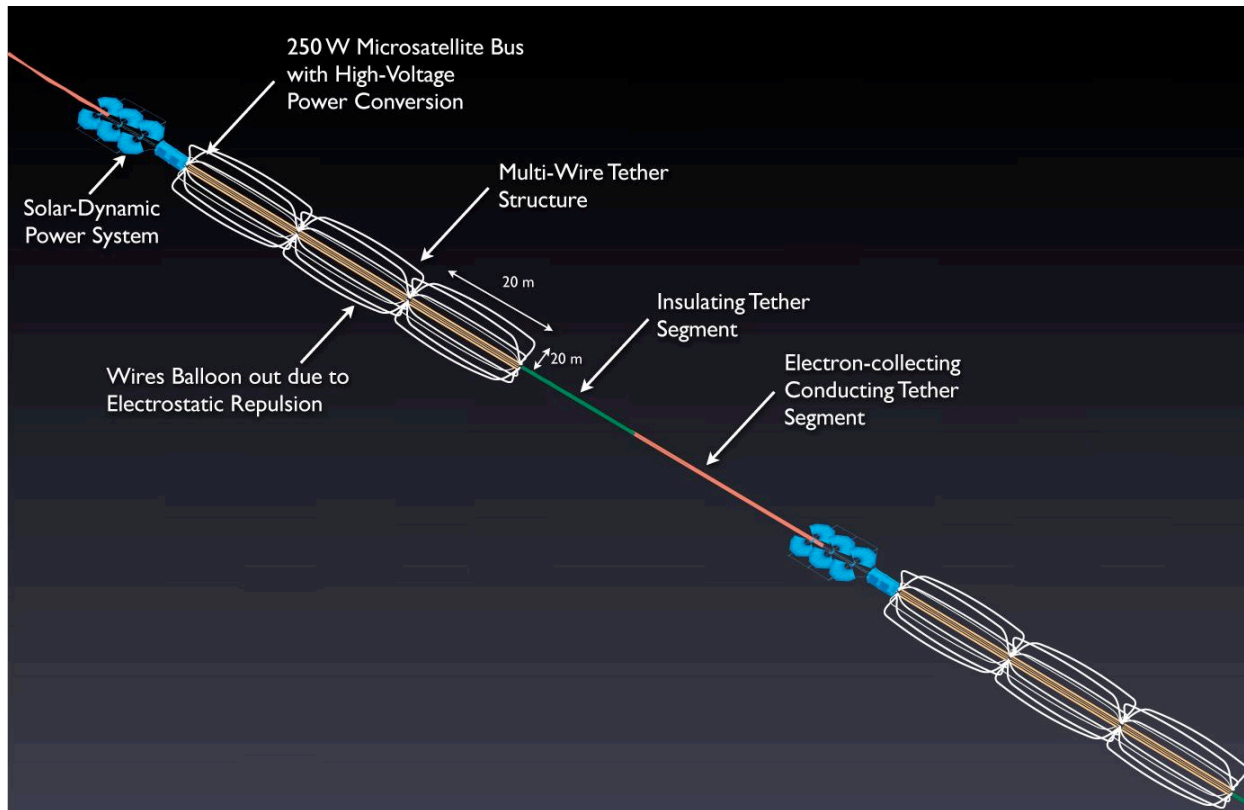


**Figure 4.** Concept for a modular architecture for an ES-RBR high-voltage structure system.

8. Sanmartín, J.R., Martínez-Sánchez, M., Ahedo, E., “Bare Wire Anodes for Electrodynamic Tethers,” *J. Propulsion and Power*, 7(3), pp. 353-360, 1993.
9. Chang, C. L. , A. S. Lipatov, A. T. Drobot, K. Papadopoulos, and P. Satya-Narayana, “Hybrid simulations of whistler waves generation and current closure by a pulsed tether in the ionosphere,” *Geophys. Res. Lett.*, 21, 1015, 1994.

tether. Because this system will orbit in the heart of the radiation belts, a solar power conversion system that is insensitive to radiation doses is necessary. Solar dynamic power conversion may be a strong candidate for this component. Each tether module itself would be divided into three segments: a long length of multi-wire conducting tether to serve as the negatively-biased electrostatic structure, a segment of nonconducting tether to serve as an insulator between segments, and a shorter length of conducting tether, such as a flat braided ribbon of metalized aramid fibers, to serve as the electron-collecting anode. The multi-wire tether structure could be implemented by stringing multiple wires together in parallel, with periodic interconnections, and relying upon electrostatic repulsion between the wires to spread them apart into a periodic ‘egg-beater’ type configuration as illustrated in Figure 4. Although the tether structures utilized would be very long, tens to hundreds of kilometers in length, because they would be constructed with very thin wires, their total masses would be quite low, on the order of several hundred kilograms for a 100-km structure.

Such a modular architecture could minimize system costs by taking advantages of economies of scale in manufacturing and testing, as well as by enabling a large ES system to be deployed using several small, low cost launch vehicles rather than a single large and expensive vehicle.

### **III.B. Plasma Sheath Effects and the Multi-Wire Tether Concept**

The choice of a multi-wire structure for the electrostatic tether is driven primarily by the need to overcome the effects of the cold, low-density plasmas present at the altitudes of interest. The ions and electrons in the ionospheric or plasmaspheric plasma will react to the electric fields generated around the high voltage wires, forming a ‘plasma sheath’ within which charge separation between the ions and electrons will limit the range over which the electric fields are significant. The effectiveness of the electrostatic structure at removing energetic particles from the radiation belt electrons depends both upon the size of its plasma sheath, which determines how large a fraction of the total number of particles in the belt pass are influenced by the electrostatic structure at any given time, and upon the strength of the electric field within that sheath, which determines how large a deflection in pitch angle of each of those electrons experiences. As a result, the effectiveness of the system depends very strongly upon the size of the plasma sheath that develops around the structure. As will be detailed through analytic means in the following section, the single-wire tether approach originally proposed by Danilov requires megavolt level potentials and gigawatt level system powers to achieve significant remediation of the radiation belts.

A tether structure design that arranges multiple small wires in a large-diameter cylinder can dramatically improve the remediation efficiency of the electrostatic tether at a given voltage, enabling a system design with feasible power and voltage requirements. This improvement is due to the fact that the electric field intensity around the tether depends upon the total linear charge density on the tether, and only indirectly upon the voltage of the tether. In order to increase the electric field intensity around a tether, we must increase the linear charge density on the tether. If the a single wire is used, and the diameter of the tether wire is held constant, that additional charge must be packed into the same volume, and so the wire’s voltage must increase. If, however, we divide that additional charge density up amongst several wires, and spread those wires apart in a cylindrical arrangement centered on the position of the original wire, the voltage on the system can be held constant, but by Gauss’ law, the electric field outside the ring of wires is equivalent to the electric field of the single higher voltage wire, as illustrated in Figure 5.

Figure 4 shows a concept for a multi-wire tether structure that could be stowed on a single spool and then deployed from a spacecraft. This concept arranges a number of uninsulated wires in a cylinder around a central, insulated conductor. The insulated conductor in the center of the structure serves as a low impedance path for carrying the collected current along the length of the tether so as to minimize voltage drop along the structure. Electrostatic repulsion between the charged wires will serve to expand them out into a roughly cylindrical arrangement, with the equilibrium shape of the structure determined by the balance of tensions in the line with the electrostatic forces on each wire due to the charge on the other lines, as moderated by the plasma sheath, as well as the attractive forces between the wires resulting from the currents flowing along the wires. The expanded structure is expected to be stable against perturbations due to tether currents because any collapse in the structure due to the current-induced attractive forces would result in a decrease in sheath size and a concomitant decrease in collected current.

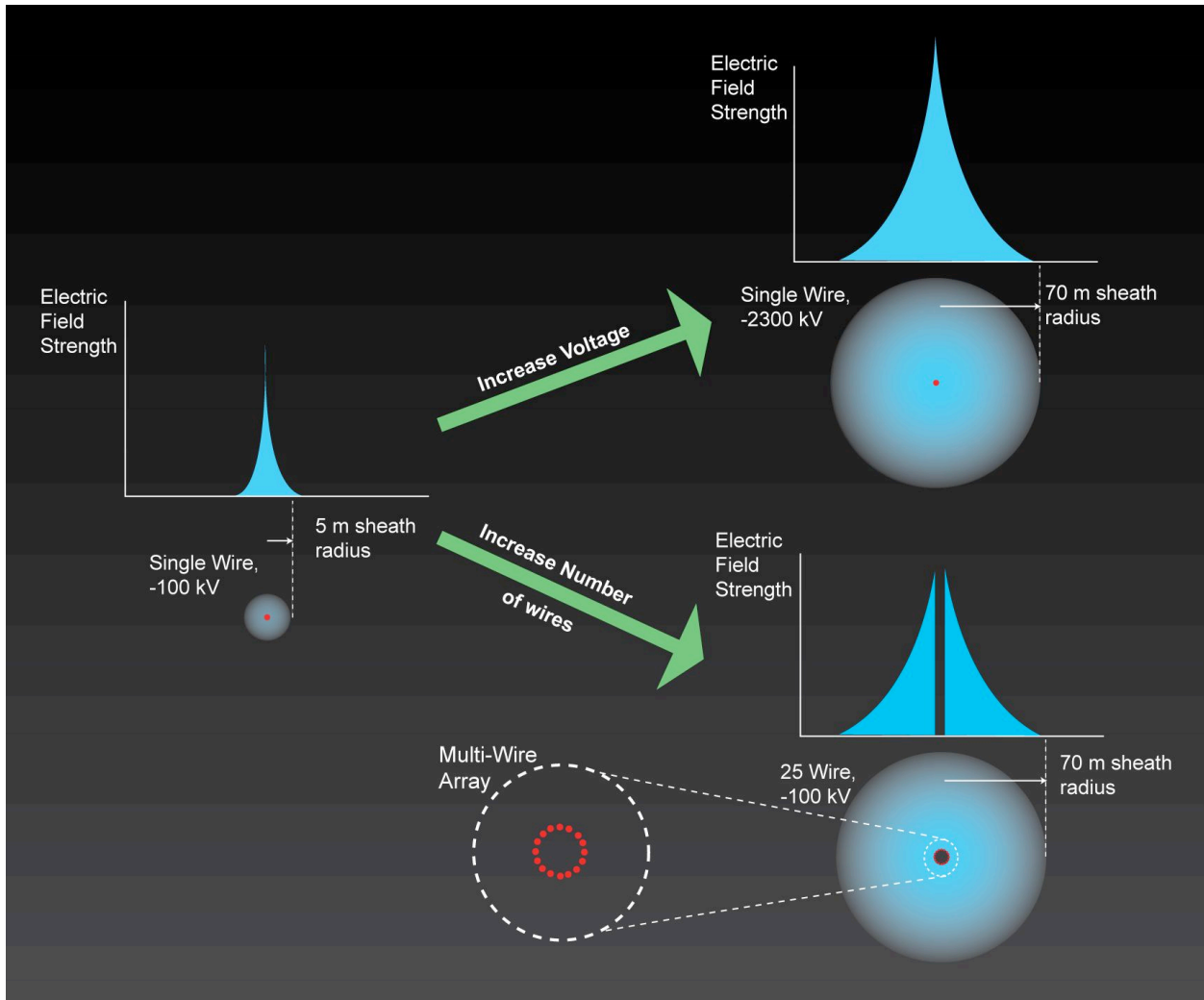


**Figure 5.** Use of a multi-wire array can enable a larger plasma sheath, with stronger electric fields, to be generated around an electrostatic structure without increasing the bias potential.

#### IV. ELECTROSTATIC REMEDIATION SYSTEM SCALING

To provide guidance for the design of an Electrostatic Radiation Belt Remediation System, it is useful to derive several expressions that describe how the system sizing scales with the design parameters. These expressions describe how the high-voltage tether interacts with two distinct populations of particles: the highly relativistic electrons trapped in the radiation belts, and the cold electrons and ions that form the plasmasphere. The objective of the analysis is to determine, to first order, how many electrostatic systems of a given size will be needed to remediate the energetic particle fluxes within a radiation belt within a given period of time. This number of required systems will drive the cost and feasibility of such a radiation belt remediation architecture. This initial analytical treatment will not consider the effects of natural source and sink terms; the effects of these terms will be studied in the numerical analyses presented in Section VIII

##### IV.A. Radiation Flux Decay

In order to derive these expressions in an analytic form that will be useful for quick scaling studies, we will consider the simplified scenario illustrated in Figure 6. The radiation belt is approximated by a toroidal solid encircling the Earth, with a crescent-shaped cross-section. At the equatorial plane, the radiation belt has an outer diameter of  $r_2$  and an inner diameter of  $r_1$ .

Within this radiation belt, the trapped energetic electrons bounce rapidly back and forth between the reflection points near the north and south poles, crossing the equatorial plane twice per cycle. For a 1-MeV electron in the inner electron belt, the bounce frequency is roughly  $15 \text{ s}^{-1}$ , meaning that each electron crosses the equatorial plane approximately 30 times per second.<sup>10</sup> A 1-MeV electron will also drift azimuthally around the Earth with a frequency of approximately 0.3 mHz. In the period of a day, the electron will thus cross the equatorial plane approximately 2.6 million times, with an average azimuthal spacing of 20 meters. If an electrostatic structure with a 100-meter sheath radius were deployed in the equatorial plane at the altitude where the electron crosses the equator, that electron will pass through the electrostatic sheath approximately 10 times per day. Because it may not be practical to deploy a single long tether structure spanning the entire altitude range of the radiation belt, we will instead consider a system composed of a number of shorter tethers.

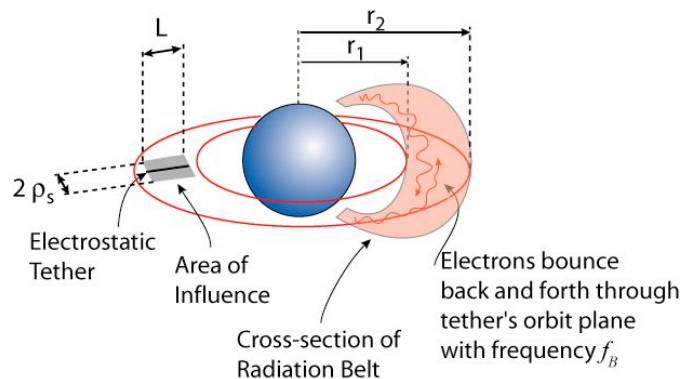


**Figure 6.** The geometry of the interaction of the electrostatic tether and the radiation belt.

If we define  $N_e(t)$  as the total number of energetic electrons trapped in L-value range between  $r_1/R_E$  and  $r_2/R_E$ , where  $R_E$  is the Earth's equatorial radius, the number of electrons crossing the

10. Spjeldvik, W.N., Rothwell, R.L., "The Radiation Belts", Chapter 5 in *Handbook of Geophysics and Space Environment 1985*, A.S. Jurse, Ed., AF Geophysical Lab, p. 5-50

equatorial plane per second is  $2f_B N_e(t)$ . Dividing by the equatorial area of the belt, we can express the average equatorial radiation flux as

$$\Phi(t) = \left[ \frac{N_e(t)}{\pi(r_2^2 - r_1^2)} 2f_B \right]. \quad (\text{IV.1})$$

To remediate this radiation flux, we will place one or more electrostatic tethers into slightly elliptical orbits in the equatorial plane, with the perigee and apogee of the tether's orbit chosen so that the tether's altitude varies between  $r_1$  and  $r_2$ . Because the geomagnetic field is stronger closer to the Earth, gradient drift causes radiation belt electrons to drift azimuthally around the Earth as they bounce back and forth through the equatorial plane. Consequently, each of the electrons in the belt will eventually pass near an electrostatic tether and can potentially be removed from the belt through interactions with the tether. In this section we will use a simple analytical approach to estimate the frequency of tether-particle interactions. In Section VI we will utilize numerical simulations to calculate in detail how frequently an orbiting electrostatic tether will interact with trapped electrons and protons in the radiation belts, taking into account the true orbital dynamics of the tethers and the bounce and drift motions of the particles, and verify that the simple analytical approach is valid to first order.

In order to deplete the radiation belt electrons, the electrostatic tethers will be charged to a large negative voltage relative to their environment. If these tethers were in a perfect vacuum, the voltage on the tether would create an electric field around the tether that would extend out to infinity with an intensity decreasing with radius  $r$  as  $1/r$ . However, because sunlight ionizes the top regions of the Earth's atmosphere, a thin plasma called the plasmasphere exists in the region around the Earth. When a negative voltage is applied to the electrostatic tether, electrons in the plasmaspheric plasma will be repelled from the tether wires and ions in the plasma will accelerate towards the wire. As a result of the responses of the cold plasma particles to the tether's voltage, a region of charge imbalance forms around the tether that limits the range of its electric field. The region within which the tether's electric field is confined is called its "plasma sheath," and it will have a characteristic radius  $\rho_{sheath}$  that we will define as the radius at which the potential due to the charge on the tether drops below the electron temperature of the cold ambient plasma.

Consequently, as an electrostatic tether moves in its orbit, it will affect an area in the equatorial plane with a length roughly equal to the tether length  $L$  and a width equal to  $2\rho_{sheath}$ . If we define the electrostatic tether's "depletion efficiency"  $\eta_s$  as the probability that an energetic electron passing through its area of influence will be scattered into the loss cone and removed from the belt, we can describe the rate at which the total number of electrons in the belt decreases as

$$\frac{\partial N_e(t)}{\partial t} = -N_{sats} (2\rho_{sheath} L) \eta_s \left[ \frac{2f_B}{\pi(r_2^2 - r_1^2)} N_e(t) \right], \quad (\text{IV.2})$$

where  $N_{sats}$  is the number of electrostatic tether satellites in the remediation system.

If we assume that the depletion efficiency is constant over time, Eqn. 2 indicates that the electrostatic tether system will drive an exponential decay of the number of trapped electrons in the belt,

$$N_e(t) = N_e(t=0) \exp[\beta t],$$

$$\text{where } \beta = \left[ \frac{-N_{sats} 2\rho_{sheath} L \eta_s 2f_B}{\pi(r_2^2 - r_1^2)} \right]. \quad (IV.3)$$

Inserting Eqn. 3 into Eqn. 1, we find that the average flux through the equatorial plane also decays exponentially:

$$\Phi(t) = \left[ \frac{2f_B}{\pi(r_2^2 - r_1^2)} \right] N_e(t) = \Phi_o \exp \left[ -\frac{N_{sats} 2\rho_{sheath} L \eta_s 2f_B}{\pi(r_2^2 - r_1^2)} t \right]. \quad (IV.4)$$

So, if our electrostatic tether system must be capable of reducing an initial average radiation flux  $\Phi_o$  to a value  $\Phi_f$  within a remediation time  $T_f$ , we must have

$$\Phi_f = \Phi(T_f) = \Phi_o \exp \left[ -\frac{N_{sats} 2\rho_{sheath} L \eta_s 2f_B}{\pi(r_2^2 - r_1^2)} T_f \right]. \quad (IV.5)$$

Taking the logarithm of both sides and solving for the required number of satellites  $N_{sats}$ , we find

$$N_{sats} = \left[ \frac{1}{T_f} \ln \left( \frac{\Phi_o}{\Phi_f} \right) \pi(r_2^2 - r_1^2) \frac{1}{4f_B} \right] \frac{1}{L} \frac{1}{\rho_{sheath} \eta_s} = F_{BELT} \frac{1}{L} \frac{1}{\rho_{sheath} \eta_s}, \quad (IV.6)$$

where  $F_{BELT}$  is equal to the term inside the brackets and is a constant determined by the severity and extent of the radiation belt, the level to which it must be remediated, and the time allowed for remediation. The number of electrostatic tether systems is therefore inversely proportional to the length of each tether, the size of its plasma sheath, and the efficiency with which it scatters electrons into the loss cone and thereby depletes them from the radiation belt.

In order to put Eqn. 6 into a more useful form, we desire to obtain expressions describing the dependence of depletion efficiency upon the sheath size.

#### IV.B. Plasma Sheath Size

Plasma physicists commonly utilize a rule-of-thumb that the plasma sheath size is “a few times” the Debye length of the plasma,  $\lambda_{De}$ . Because the voltages that will be applied to the electrostatic tether ( $\sim 100$  kV) are many orders of magnitude greater than the electron temperature ( $T_e \approx 0.1 - 0.5$  eV) of the lower plasmaspheric plasma, however, this rule-of-thumb breaks down, and in fact the sheath size of the electrostatic tether can be many times the Debye length of the plasma. The size and structure of the plasma sheath depend primarily upon the tether’s bias voltage  $V$ , the radius of the tether wire  $r_w$ , and the density of the plasma,  $n_{plasma}$ . Unfortunately, simple analytic expressions for the size  $\rho_{sheath}$  and profile  $V(r)$  of a high-voltage ( $V \gg T_e$ ) sheath are not available, and these quantities must be determined through the simultaneous solution of Poisson’s equation and Vlasov’s equations using numerical methods.<sup>11</sup> Such calculations have been performed by

11. Choinière, E., Gilchrist, B.E., “Modeling Long Probes in Flowing Plasmas using KiPS-2D, a Novel Steady-State Vlasov Solver,” *39th Joint Propulsion Conference and Exhibit*, 20-23 July 2003, Huntsville, AL, AIAA Paper 2003-5098.

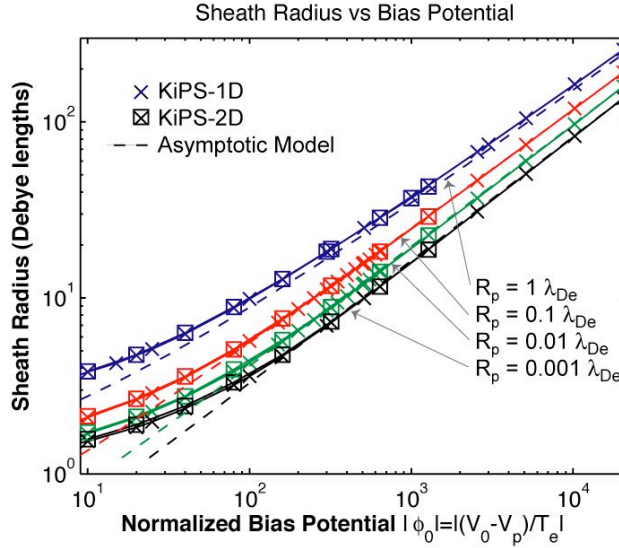


**Figure 7.** Variation of the sheath size with bias potential, and probe size calculated by Choinière using his KiPS-1D and KiPS-2D models for plasmas with no flow velocity.<sup>12</sup>

Choinière using a numerical model called the Kinetic Plasma Solver (KiPS), which is implemented in both 1D and 2D versions.<sup>12</sup> The KiPS-1-D simulations indicate that the sheath size has a weak dependence on the wire radius and a strong dependence on the bias voltage. As illustrated in Figure 7, at higher bias voltages the relationship between voltage and the sheath size in a quiescent plasma,  $\rho_{no\ flow}$ , can be approximated well by an asymptotic fit function:

$$V = 2.554 T_e \left( \frac{\rho_{no\ flow}}{\lambda_{De}} \right)^{1.325} \ln \frac{\rho_{no\ flow}}{r_w}. \quad (IV.7)$$

#### IV.C. Plasma Flow Effects on Sheath Size

The electrostatic tether systems will orbit at high-LEO to mid-MEO altitudes, where the dominant plasma ion species is hydrogen. At these altitudes, the relative flow energy of the hydrogen ions due to the orbital motion of the tether will be approximately 0.3 eV, which is roughly comparable to the 0.3-0.5 eV plasma temperatures that have been measured at those altitudes.<sup>13</sup> This flow velocity can be expected to alter the size and the shape of the plasma sheath. The KiPS-2D model is able to capture the effects of plasma flow, and recent simulations by Choinière of the plasma sheaths of negatively biased wires in flowing plasmas indicate that for flow energies comparable to or greater than the ion temperature, the sheath is distorted by the flow, with a compressed region in front of the tether and an extended “wake” region behind the

12. Choinière, E., *Theory and Experimental Evaluation of a Consistent Steady-State Kinetic Model for 2D Conductive Structures in Ionospheric Plasmas with Applications to Bare Electrodynamic Tethers in Space*, U. Michigan Ph.D. Thesis, May 2004.

13. Craven, P. D., R. H. Comfort, D. L. Gallagher, and R. West, “A study of the statistical behavior of ion temperatures from DE 1/RIMS,” *Modeling Magnetospheric Plasma Processes*, Geophysical Monograph 62, American Geophysical Union, 1991.

tether.<sup>12</sup> If we ignore the lower voltage wake region, the effects of the flow can be accounted for roughly by scaling the sheath size calculated in Eqn. (7) as

$$\rho_{sheath, with\ flow} \approx 0.7 \rho_{sheath, no\ flow}, \quad U_i \approx T_i. \quad (IV.8)$$

Choinière’s simulations also indicate that the electric field within the sheath can be approximated as

$$\vec{E}(r) = -\frac{V}{\ln\left[\frac{\rho_{sheath}}{r_w}\right]} \frac{1}{r} \hat{r}. \quad (IV.9)$$

#### IV.D. Depletion Efficiency

In order to obtain an analytic expression for the depletion efficiency of an electrostatic tether, we will utilize a simplified analysis of the collision of the electrons with the charged tether similar to the derivation of plasma collision frequency in Nicholson.<sup>14</sup> It should be noted here that this simplified analysis is valid only for the purposes of illustrating scaling of the depletion efficiency with tether voltage and other parameters; calculation of accurate depletion efficiencies requires a much more detailed process involving Monte-Carlo simulation of particle trajectories in three dimensions within the region of influence of the tether as well as numerical modeling of the diffusion of the radiation belt particles into the loss cone. Such an analysis has been carried out and is described by Minor.<sup>15</sup> To estimate an approximate depletion efficiency, we will consider an interaction between a relativistic electron and a negatively charged wire as illustrated in Figure 8.

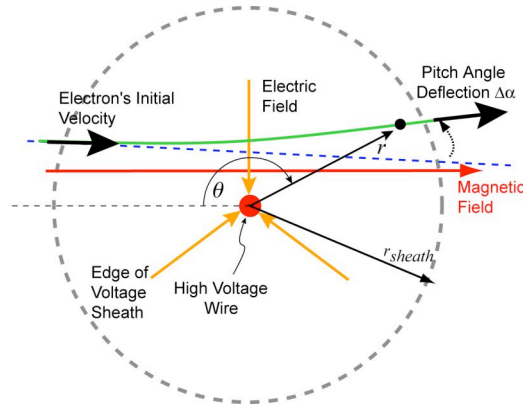


**Figure 8.** Schematic of the simplified scattering analysis.

As the electron passes by the charged wire, it experiences a central force equal to

$$\vec{F}(r) = q\vec{E}(r) = e \frac{V}{\ln\left[\frac{\rho_{sheath}}{r_w}\right]} \frac{1}{r} \hat{r}, \quad (IV.10)$$

where  $e$  is the electron charge.

Here we assume that the gyroradius of the electron is large compared to the sheath so that we can neglect the effect of the magnetic field; this assumption may not be valid for very large ( $> 150$

14. Nicholson, D.R., *Introduction to Plasma Theory*, John Wiley & Sons, NY, 1983, p. 9-11.

15. Minor, B.M., “Simulation of Radiation Belt Remediation Using Electrostatic Tether Structures,” Appendix H in *Electrodynamics/ Electrostatic Tether Performance Assesment*, Final Report on DARPA Seedling Contract, April 2004.

m radius) electrostatic plasma sheaths, and thus higher-fidelity analyses may require detailed simulation of the particle kinetics. We also assume that the particle is deflected by a small angle and that velocity  $v$  along the particle's trajectory is essentially constant, so that

$$x(t) = -r \cos \theta = -\frac{p \cos \theta}{\sin \theta} = v_o t, \quad (\text{IV.11})$$

where the angle  $\theta$ , defined in Figure 8, is related to the velocity by

$$dt = \frac{p}{v_o} \frac{d\theta}{\sin^2 \theta}, \quad (\text{IV.12})$$

where  $p = r \sin \theta$ . Integrating the force the particle experiences in the direction perpendicular to its trajectory provides the change in its perpendicular momentum

$$mv_{\perp} = \int F_{\perp}(t) dt = \int \frac{eV}{\ln \left[ \frac{\rho_{\text{sheath}}}{r_w} \right]} \frac{1}{r} \sin \theta dt, \quad (\text{IV.13})$$

where  $m$  is the mass of the particle.

Using (11) and (12) we can recast this equation as:

$$mv_{\perp} = \frac{eV}{\ln \left[ \frac{\rho_{\text{sheath}}}{r_w} \right]} \frac{1}{v_o} \int_0^{\pi} d\theta = \frac{\pi eV}{\ln \left[ \frac{\rho_{\text{sheath}}}{r_w} \right]} \frac{1}{v_o}, \quad (\text{IV.14})$$

To estimate the deflection angle of the particle, we use:

$$\sin(\Delta\alpha) = \frac{mv_{\perp}}{mv} = \frac{\pi eV}{\ln \left[ \frac{\rho_{\text{sheath}}}{r_w} \right]} \frac{1}{mv_o^2}, \quad (\text{IV.15})$$

For small  $\Delta\alpha$ ,  $\sin(\Delta\alpha) \approx \Delta\alpha$ . Since the tether is oriented perpendicular to the magnetic field, and the particles approach the wire spiraling around the magnetic field with pitch angles randomly distributed between the loss cone angle  $\alpha_{LC}$  and  $\pi/2$ , the component of the particle's velocity in the direction along the magnetic field line is

$$v_o = v_{\text{total}} \frac{\int_{\alpha_{LC}}^{\pi/2} \sin \alpha d\alpha}{\int_{\alpha_{LC}}^{\pi/2} d\alpha} = v_{\text{total}} \frac{(1 - \sin \alpha_{LC})}{\left(\frac{\pi}{2} - \alpha_{LC}\right)} \quad (\text{IV.16})$$

Using the relativistic relationship between the velocity and kinetic energy  $K$  of the electron, we find that the pitch angle of the particle will be changed by

$$|\Delta\alpha| \approx \frac{\pi e}{\ln\left[\frac{\rho_{\text{sheath}}}{r_w}\right]} \frac{\left(\frac{\pi}{2} - \alpha_{LC}\right)}{(1 - \sin\alpha_{LC})} \frac{V}{2K} \left(\frac{K + m_e c^2}{K + 2m_e c^2}\right). \quad (\text{IV.17})$$

Note that the scattering angle depends upon the kinetic energy of the particle. In a full numerical analysis, the scattering must be evaluated across the energy spectrum of the trapped radiation particles, and this scattering must be applied to a realistic pitch angle distribution of particles. For the purposes of this simplified scaling analysis, however, we will assume a single average particle energy. Furthermore, because pitch angle distributions for HAND-induced radiation belts are not publicly available, in order to estimate the scattering efficiency from the change in pitch angle, we assume that the trapped particles have “top-hat” distribution of their pitch angles, in which their pitch angles are evenly distributed between the loss cone angle and  $\pi/2$ , as illustrated in Figure 9.

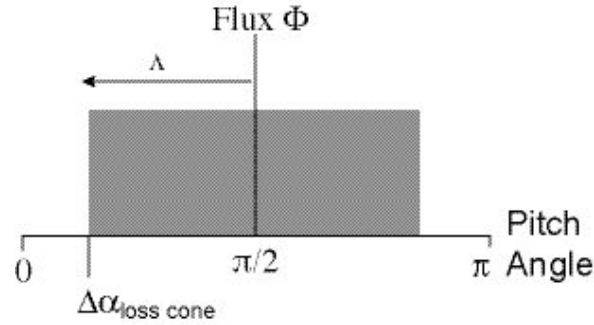


**Figure 9.** “Top-hat” pitch angle distribution.

To deplete this population using a process where the particles interact with a tether and are scattered by a small angle  $\pm\Delta\alpha$  on each interaction with the tether, multiple interactions between the wire and the particle will eventually lead the particles to randomly walk over to the loss cone. On average, we need to change the particle’s pitch angle by

$$\Lambda = \frac{\pi}{2} - \alpha_{LC} \quad (\text{IV.18})$$

The total pitch angle change after N random hops of  $\pm\Delta\alpha$  is

$$\Delta\alpha_{\text{tot}} = \Delta\alpha_1 + \Delta\alpha_2 + \dots + \Delta\alpha_N \quad \Delta\alpha_i = \pm\Delta\alpha \quad (\text{IV.19})$$

The average of  $\Delta\alpha_{\text{tot}} = 0$ , but the ensemble average of the square of the pitch angle change is

$$\langle(\Delta\Lambda)^2\rangle = \left\langle \sum_{i=1}^N \langle(\Delta\alpha_i)^2\rangle \right\rangle = N(\Delta\alpha)^2 \quad (\text{IV.20})$$

So the average number of scattering interactions N needed to scatter the particles into the loss cone is

$$N = \frac{(\Lambda)^2}{(\Delta\alpha)^2} \quad (\text{IV.21})$$

And the average fraction of the particle population that is scattered into the loss cone on each interaction with the tether can be estimated as

$$\eta \approx \frac{1}{N} = \frac{(\Delta\alpha)^2}{\left(\frac{\pi}{2} - \alpha_{LC}\right)^2}, \quad (\text{IV.22})$$

so that

$$\eta \approx \left( \frac{\pi e}{(1 - \sin \alpha_{LC})} \frac{1}{\ln(\rho_{\text{sheath}}/r_w)} \frac{1}{2K} \left( \frac{K + m_e c^2}{K + 2m_e c^2} \right) \right)^2 V^2. \quad (\text{IV.23})$$

Using Eqn. (7) and (8) to obtain an expression for  $V$  in terms of  $\rho_s$ , we can eliminate voltage from the equation and obtain an expression for the depletion efficiency for a single-wire tether in terms of the sheath size:

$$\eta \approx (6.5229) \left( \frac{\pi e}{(1 - \sin \alpha_{LC})} \frac{T_e}{\ln(\rho_{\text{sheath}}/r_w)} \frac{1}{2K} \left( \frac{K + m_e c^2}{K + 2m_e c^2} \right) \right)^2 \left[ \ln \frac{\rho_{\text{sheath}}}{r_w} \right]^2 \left( \frac{\rho_{\text{sheath}}}{\lambda_{De}} \right)^{2.65}. \quad (\text{IV.24})$$

We can then substitute Eqn. 24 into Eqn. 6 to obtain,

$$N_{\text{sats}} = \left\{ 0.1533 F_{\text{BELT}} \frac{1}{L} \left[ \left( \frac{1 - \sin \alpha_{LC}}{\pi e} \right) \frac{2K}{T_e} \frac{K + 2m_e c^2}{K + m_e c^2} \right]^2 \right\} \left[ \ln \left( \frac{\rho_{\text{sheath}}}{r_w} \right) \right]^{-2} \frac{1}{\rho_{\text{sheath}}^{3.65}}, \quad (\text{IV.25})$$

If we choose the tether length  $L$  and the tether wire radius  $r_w$  to be fixed, the number of electrostatic tether systems required can be expressed as a function of only the sheath size

$$N_{\text{sats}} = C_1 \left[ \ln \left( \frac{\rho_{\text{sheath}}}{r_w} \right) \right]^{-2} \frac{1}{\rho_{\text{sheath}}^{3.65}}, \quad (\text{IV.26})$$

where  $C_1$  is a constant representing the terms in the brackets in Eqn. 25. Eqn. 26 shows that the required number of satellites depends strongly upon the size of the plasma sheath that the electrostatic tethers can generate.

## V. USING MULTI-WIRE STRUCTURES TO MINIMIZE ES-RBR SYSTEM SIZE AND POWER

The amount of power required to maintain the bias voltage on the conducting structures in an ElectroStatic Radiation Belt Remediation System (ES-RBR) is a primary driver on the overall feasibility of the system concept. Application of power is required because when the structures are biased relative to their environment, they will attract and collect charged particles from the ambient plasma (ionospheric or plasmaspheric, depending upon altitude). Thus a continual flow of current to the structure must be supplied to maintain the charge on the structure. To minimize the currents in the system, the electrostatic structures will be biased negatively relative to their environment so that they collect protons and other positively charged plasmaspheric ions, rather than the far more mobile electrons. The amount of ion current collected by the high voltage structure will depend heavily upon the local plasma density. It also depends upon the nature of charge collection in the high-voltage plasma sheath structure that forms around the structure. In this document we first develop a model to estimate the collection of current by an electrostatic structure. We next determine nominal plasmaspheric ion densities over the range of altitudes of interest for an ES-RBR system, and then estimate the power required for a concept system. Finally, we present estimates of the number of systems required to remediate radiation belts around the Earth and in the Jovian system.

### V.A. Electrostatic Tether System Power

Although it is tempting to conclude from a quick inspection of Eqns. IV.7 and IV.26 that the number of spacecraft needed for an ES-RBR system can be reduced to a reasonable level by simply increasing the tether voltage to generate a large sheath, in designing an electrostatic tether system, it is important to also consider the power required for each of the tether systems. Because charged tether wires are exposed to the plasmasphere, they will attract ions (primarily protons at the altitudes of interest), resulting in a collection of current along the length of the wire. In order to maintain the voltage applied to the tether, the system must therefore supply power to the tether to support the flow of the current across the tether voltage,  $P=IV$ . In addition, ohmic losses due to resistance in the tether wires will increase the power requirements, but for the purposes of this analysis we will assume that the ohmic losses are small compared to the ion current collection power requirements.

### V.B. OML Current

At the altitudes where radiation belts can form, the plasmaspheric plasma density and temperatures are such that the plasma Debye lengths are on the order of a centimeter, and the plasmas are considered collisionless. Because the electrostatic tether systems will use thin wires with sizes of a millimeter or less, the plasma sheath size can be assumed to be much larger than the thickness of the tether wire. In this regime, the currents collected by the charged wire have an upper bound given by the Orbit Motion Limit (OML) theory.<sup>16</sup> This theory derives its name from the fact that because the charged particles approaching the tether experience no collisions or potential barriers as they move towards the wire, their angular momentum with respect to the wire is conserved, and so those particles with significant angular momentum will follow a

---

16. Chung, P.M., Talbot, L., Touryan, K.J., *Electric Probes in Stationary and Flowing Plasmas: Theory and Application*, Springer-Verlag, NY, 1975, p. 9.

hyperbolic “orbit” around the probe and miss it. For a single wire charged to large negative voltage, the OML theory predicts that the upper bound on the current collected per unit length of wire is

$$\frac{dI}{dl} = n_{plasma} e 2r_w \sqrt{\frac{2e|V|}{m_i}}, \quad (\text{V.1})$$

where  $m_i$  is the ion mass.

Readers familiar with the results of the TSS experiments conducted on the Shuttle Orbiter may question our use of the OML theory to predict the collected current on the bare wires, as the TSS experiments found electron current collections by the spherical tethered satellite were approximately 4 times greater than that predicted by the Parker-Murphy theory.<sup>17</sup> It is important to note, however, that the TSS experiment flew at low-LEO altitudes where the predominant plasma ion species was oxygen, and the orbital motion of the TSS-1R tether with respect to the ionospheric plasma resulted in a relative flow energy of the oxygen ions of 5 eV. At those altitudes, the ionospheric plasma has a thermal temperature of only 0.1 eV. As a result of the flow energy of the plasma being 50 times greater than its thermal energy, plasma “bow-shock” phenomena and plasma sheath instabilities resulted that violated the assumptions of the OML theory, allowing an enhancement of the current that the plasma could carry to the conductors in the experiment.<sup>18</sup>

At the high-LEO to mid-MEO altitudes at which an ES-RBR system will operate, the relative ion flow energy is roughly equal to the local plasma temperature. Consequently the orbital motion of the tether results in more of a plasma “drift” than a “flow” relative to the tether, and is less likely to result in significant instabilities that will enhance ion collection by the charged wire. For this reason, we anticipate that the OML theory will provide a reasonable estimate of the currents the electrostatic tether will collect.

### V.C. Electron Emission Due to Ion Bombardment

At the many-kilovolt bias voltages necessary to effect significant scattering of MeV-class particles, emission of electron current from the tether wires due to bombardment by the energetic ions must be taken into account. The emitted current is strongly dependent upon the wire material and the ions bombarding it. A review of available literature on electron ejection due to ion bombardment indicates that molybdenum or nickel wire conductors may provide a relatively low electron emission yield. For 100-1000 KeV hydrogen ions, the yield of molybdenum and nickel is approximately  $Y_{secondary} \approx 1.5$ .<sup>19</sup>

Using the OML model, the total power for a system of several electrostatic tether satellites *using single wire tethers* is

- 
17. Dobrowolny, M, *et al.*, “Current-voltage characteristics of the TSS-1 satellite,” *J. Geophys.Res.*, 100(23) p. 953, 1995.
  18. Stone, N.H., Raitt, W.J., Wright, K.H., “The TSS-1R Electrodynamic Tether Experiment: Scientific and Technological Results,” *Adv. Space Res.*, 24(8) pp. 1037-1045, 1999.
  19. Krebs, K.H., “Electron Ejection from Solids by Atomic Particles with Kinetic Energy”, *Fortschritte der Physik*, 16, p 419-490, 1968.

$$\begin{aligned}
 P_{system} &= L_{tether} \frac{dI}{dl} V \\
 &= L_{tether} N_{sats} 2r_w (1 + Y_{secondary}) e n_{plasma} \sqrt{\frac{2e}{m_i}} V^{3/2}
 \end{aligned}
 \tag{V.2}$$

Eqn. V.2 illustrates that there is a strong dependence of the total system power upon the system voltage. However, the term  $N_{sats}$  in Eqn. VI.26 also has a dependence upon voltage, because the sheath radius and depletion efficiency also vary with voltage. We can use Eqns. VI.6 and VI.23 to express Eqn. V.2 as:

$$P_{System} \approx \frac{\left[ 2(1 + Y_{secondary}) F_{BELT} r_w e n_{plasma} \sqrt{\frac{2e}{m_i}} \right]}{\left[ \frac{\pi e}{(1 - \sin \alpha_{LC}) \ln(\rho_{sheath}/r_w)} \frac{1}{2K} \left( \frac{K + m_e c^2}{K + 2m_e c^2} \right) \right]^2} \sqrt{\frac{1}{V}} \frac{1}{\rho_s}
 \tag{V.3}$$

Due to the dependence of the sheath size  $\rho_{sheath}$  on voltage, as expressed in Eqn. VI.7, this equation must be solved implicitly; if, however, we ignore the term  $\ln[\rho_{sheath}/r_w]$  in Eqn. VI.7 as much more slowly varying than the  $[\rho_{sheath}/\lambda_{De}]^{1.325}$  term, we find that the system power varies roughly as  $V^{-4/3}$ .

Eqn. V.3 indicates that high system voltages are optimal for minimizing the system power. Unfortunately, however, in real-world implementation the cost and technology risk of the system will increase dramatically with both the system voltage and the total system power. Consequently, there are technical and economic limits on the system voltage and the system power. For the design studies conducted in this effort, we have used 1 MW as the “economically feasible” upper bound on the system power, and 200 kV as the “technically feasible” upper bound on the system voltage. Figure 10 shows the total system power computed using Eqn. V.3 for a scenario in which the ES-RBR system must provide a 1/e reduction in the 1 MeV flux of a 1000 km thick radiation belt within a period of 12 days. This figure illustrates that a *single-wire* tether design cannot perform the required remediation with a system design (voltage and total power) that falls within the region of technical and economic feasibility

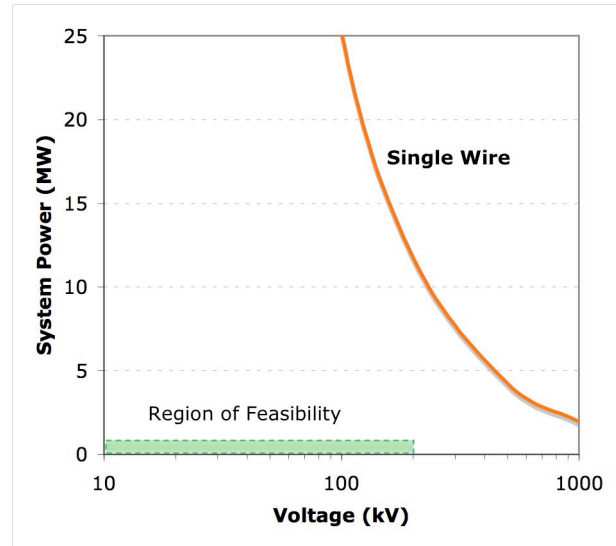


**Figure 10.** Variation of total system power with tether voltage **for a single-wire tether.**

#### V.D. The Multi-Wire Tether Concept

Although a single-wire tether design appears unable to achieve a viable system design, a tether structure design that arranges multiple small wires in a large-diameter cylinder can dramatically

improve the depletion efficiency of the electrostatic tether at a given voltage, enabling a system design with feasible power and voltage requirements. This improvement is due to the fact that the electric field intensity around the tether depends upon the total linear charge density on the tether, and only indirectly upon the voltage of the tether. The dependence of the electric field upon the voltage expressed in Eqn. VI.7 is a result of an implicit relationship between the linear charge density of a wire upon the voltage of the wire. In order to increase the electric field intensity around a tether, we must increase the linear charge density on the tether. If the diameter of the tether wire is held constant, that additional charge must be packed into the same volume, and so the wire's voltage must increase. If, however, we divide that additional charge density up amongst several wires, and spread those wires apart in a cylindrical arrangement centered on the position of the original wire, the voltage on the system can be held constant, but by Gauss' law, the electric field outside the ring of wires is equivalent to the electric field of the single higher voltage wire, as illustrated in Figure 11. Figure 12 shows a concept for a multi-wire tether structure that could be deployed from a spacecraft. This concept arranges a number of uninsulated wires in a cylinder around a central, insulated conductor. The insulated conductor in the center of the structure serves as a low impedance path for carrying the collected current along the length of the tether so as to minimize voltage drop along the structure. Electrostatic repulsion between the charged wires will serve to expand them out into a roughly cylindrical arrangement, with the equilibrium shape of the structure determined by the balance of tensions in the line with the electrostatic forces on each wire due to the charge on the other lines, as moderated by the plasma sheath, as well as the attractive forces between the wires resulting from the currents flowing along the wires. The expanded structure is expected to be stable against perturbations in tether currents because any collapse in the structure due to the current-induced attractive forces would result in a decrease in sheath size and a concomitant decrease in collected current.

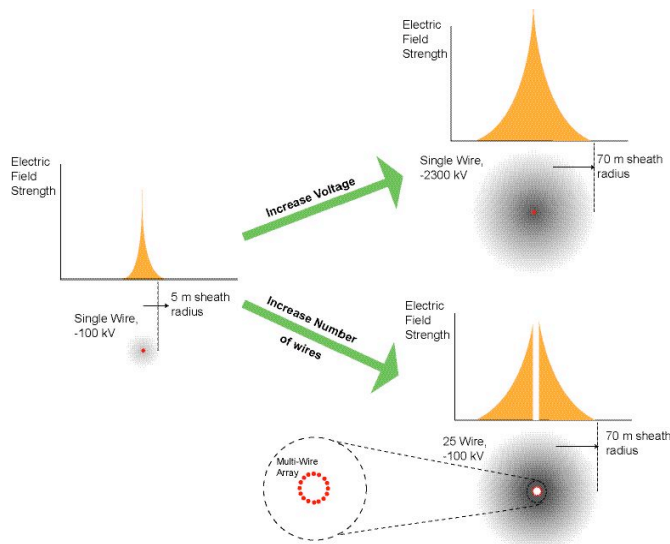


**Figure 11.** Illustration of increasing the sheath size and intensity through either increasing the tether voltage or adding additional wires at the same voltage.

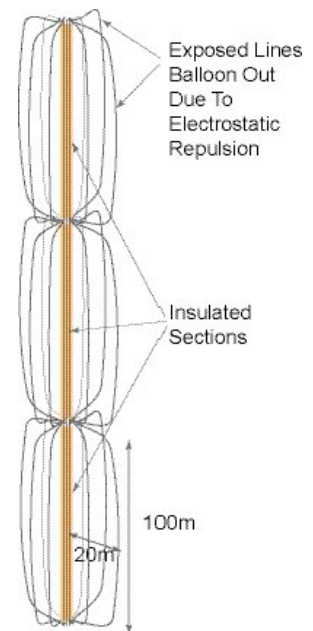


**Figure 12.** Concept design for a stowable multiline electrostatic tether structure.

In calculating the electric field strength of  $n_{wires}$  at a potential  $V$ , arranged in a cylinder of radius  $R$ , we must account for the fact that a portion of the potential on each wire is due to the charge on the other wires in the cylinder. Inside the ring, the electric field is zero. Outside the ring, a straightforward induction analysis shows that charged particles passing by the ring of wires will experience an electric field that can be approximated as the field of a single wire at a higher voltage  $GV$ , where  $G$  is a “geometric gain” factor:

$$G(n_{wires}) \approx \frac{n_{wires}}{1 + \frac{(n_{wires} - 1) \ln \rho_{sheath,1} - \sum_{i=2}^{n_{wires}} \ln \left( 2R \left| \sin \frac{(i-1)\pi}{n_{wires}} \right| \right)}{\ln \left( \frac{\rho_{sheath,1}}{r_w} \right)}}, \quad (V.4)$$

where  $r_{s,l}$  is the sheath radius of a single wire at voltage  $V$ . For a tether cylinder radius of 20 m, a wire diameter of 0.05 mm, a plasma density of 5,000/cc, and a plasma temperature of 0.5 eV,  $G(5) \approx 4.35$ ,  $G(25) \approx 16.6$ , and  $G(50) \approx 21.9$ .<sup>15</sup>

With this geometric gain, Eqns. VI.7, and VI.22 for the sheath size and depletion efficiency become:

$$GV = 2.554 T_e \left( \frac{\rho_{sheath, multewire}}{\lambda_{De}} \right)^{1.325} \ln \frac{\rho_{sheath, multewire}}{r_w}. \quad (V.5)$$

$$\eta_{multi-wire} \approx \left[ \frac{\pi e}{(1 - \sin \alpha_{loss\ cone})} \frac{1}{\ln \left( \rho_{sheath, multewire} / (r_w) \right)} \frac{1}{2K} \left( \frac{K + m_e c^2}{K + 2m_e c^2} \right) \right]^2 (GV)^2. \quad (V.6)$$

Again, we must scale the sheath size predicted by Eqn. V.5 by a factor of 0.7 to account for flow effects.

One potential concern for this multi-wire concept is the possibility that the azimuthal components of the electric field near the individual wires may result in some fraction of the ions that fall into the sheath will have a portion of their radial energy converted to azimuthal energy. These ions will then persist for multiple orbits in ‘psuedo-trapped’ trajectories within the sheath, increasing the average charge density in the sheath and thus decreasing the sheath radius. It is important to note, however, that the electrostatic tether’s plasma sheath will be in the collisionless regime, and in the absence of collisions or other transient phenomena there is no mechanism for these ions to jump to truly bounded orbits; all of these ‘psuedo-trapped’ ions will either eventually leave the sheath or intersect with the surface of a wire. The KiPS model used to conduct the simulations upon which our sheath model approximation is based does account for the flow of ions in these long-duration trajectories. Simulations of single and double-wire geometries, with plasma flow velocities representative of orbital velocities, have not observed only moderate reductions in sheath size due to these ‘psuedo-trapped’ ions, and these reductions are accounted for in the factor of 0.7 used in Eqn. VI.8.<sup>12</sup> Simulations of the plasma sheath structure of the 25-wire tether geometry will be required to determine the effect upon the

proposed system with high fidelity. Nonetheless, if the rate of population of these ‘psuedo-trapped’ trajectories is small, one potential solution would be to periodically modulate or turn off the bias voltage so as to allow these particles to escape from the sheath.

*Multi-Wire Tether Power Requirements*

The multi-wire geometry also improves system performance by reducing the amount of power needed to sustain the plasma sheath. When the individual plasma sheaths of the wires coalesce into a single, much larger sheath, outside of the cylinder of wires the equipotential lines are very nearly circular, as shown in Figure 13. Thus ions falling in from the sheath edge see electric fields that accelerate them towards the center of the structure until they are very close to the wires, and only then do the fields of the individual wires pull the ions towards the wires. By the time the ions reach the vicinity of the wires, however, they will already have fallen through a large fraction  $F$  of the total voltage on the system. Thus the wires will collect ion current like wires biased to a voltage of  $V(1-F)$  in a beam of ions with energy  $FV$ . Using the OML theory for probes in ion beams developed by Mott-Smith and Langmuir,<sup>20</sup> we can estimate the current collection of the  $N_{wires}$  as:

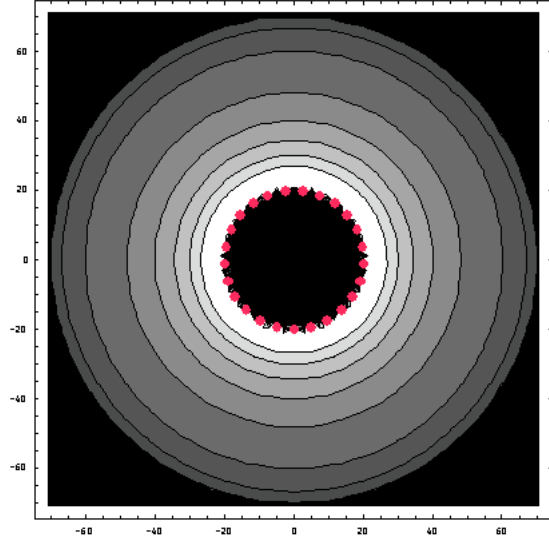


**Figure 13.** Equipotential contours within the sheath of a 25-wire tether structure.

$$I_{wire}^{multi-} = 2n_{wires} L_{tether} 2r_w (1 + Y_{secondary}) \left\{ e n_{plasma} \sqrt{\frac{kT_i}{2\pi m_i}} \right\} \frac{\rho_s}{R} \sqrt{1 + \frac{(1-F)}{F}}, \quad (V.7)$$

where  $k$  is the Boltzmann constant,  $T_i$  is the temperature of the ions, the factor of  $\rho_{sheath}/R$  is due to geometric concentration of the ions as they fall in from the sheath edge to the radius of the multiwire structure, and the factor of 2 arises from the fact that the wires collect only a tiny fraction of the ions falling into the structure, and thus they effectively see two “beams” of ions, one falling radially into the structure and one streaming radially outwards. An important thing to note in Eqn. V.7 is that due to the multi-wire effects, the current collection expressed by Eqn. V.7 depends upon the ratio  $F$  of the voltage near the array to the total voltage, rather than directly on the total voltage. The fraction  $F$  must be calculated numerically, accounting for the effects of the field of each wire upon the voltage on all of the other wires; for a 20-m radius structure with 5, 10, 25, and 50 wires biased to 100 kV each, the fraction  $F$  is 0.59, 0.73, 0.87, and 0.93, respectively.

The total power for a system of  $N_{sats}$  tether systems using multiwire tether structures is thus

20. Mott-Smith, H.M., Langmuir, I., “The Theory of Collectors in Gaseous Discharges,” *Phys. Rev.*, 28, p. 727-763, October 1926.

$$P_{System} \approx 4n_{wires} F_{BELT} \frac{r_w}{R} (1 + Y_{secondary}) \left\{ e n_{plasma} \sqrt{\frac{kT_i}{2\pi m_i}} \right\} \sqrt{\frac{1}{F}} \frac{V}{\eta_{multi-wire}} . \quad (V.8)$$

### V.E. Plasma Density

Eqn (8) shows that the ion current collected by an ES-RBR structure will depend strongly the local density of the ambient plasma. To estimate this current draw, we use Gallagher's Global Core Plasma Model<sup>21</sup> to calculate the plasma densities at local magnetic noon at the magnetic equator over the range of altitudes affected by the inner electron belt, assuming an average magnetic activity index of  $K_p = 3.0$ . The variation in plasma density over the equatorial range spanned by the belt are shown in Figure 14.

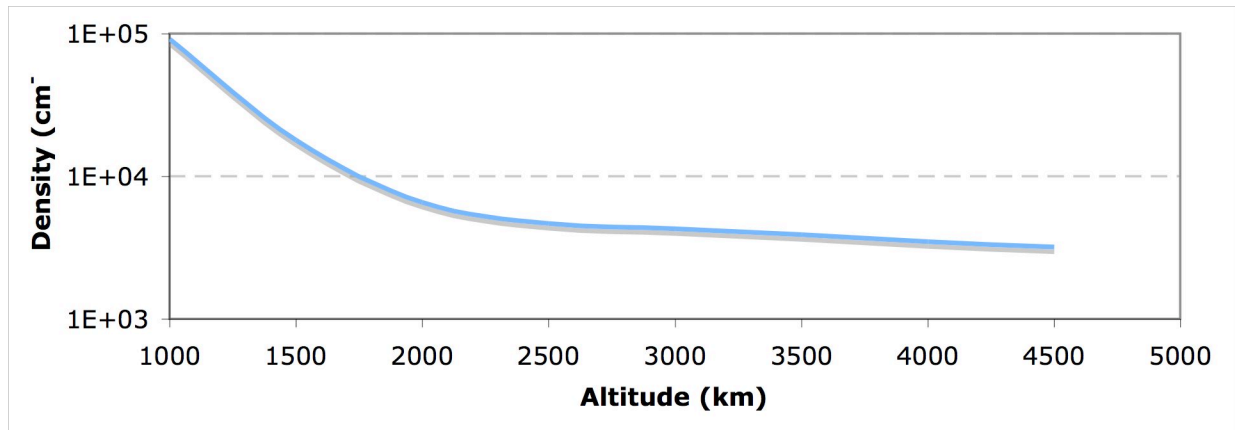


**Figure 14.** Plasma densities predicted by the Global Core Plasma Model for Local Magnetic Noon for 1 June 2002.

### V.F. ES-RBR System Power

Using the plasma densities in Figure 14, we have estimated the current and  $I^*V$  power requirements for a ES-RBR spacecraft with a 100-km long structure composed of 25 Molybdenum wires, each with a diameter of 0.2 mm (32 AWG), charged to a bias potential of -100 kV. The results are tabulated in Table 1. The power estimates summarized in Table 1 indicate that as long as the ES-RBR system's altitude is above about 2,000 km, the power requirements for a 250 km, 100 kV structure are in the range of 3-6 kW, which is quite reasonable for a spacecraft system.

**Table 1.** Electrostatic Structure Power Requirements.

Altitude (km)	Density (cm <sup>-3</sup> ) Magnetic Local Noon	Current, Radial Beam Model(A)	Beam Model Power (kW)
1000	9E+04	0.804	80.4
1500	2E+04	0.157	15.7
2000	7E+03	0.058	5.8
2500	5E+03	0.041	4.1
3000	4E+03	0.038	3.8
3500	4E+03	0.034	3.4
4000	4E+03	0.031	3.1
4500	3E+03	0.028	2.8

21 Gallagher, D.L., Craven, P.D., "Global Core Plasma Model", *J. Geophys. Res.*, 105(A8) pp 18,819-833, August 1 2000.

## V.G. System Sizing for Earth and Jovian Radiation Belts

We can now use the results of this and the prior section to estimate the number of ES-RBR spacecraft required to perform remediation of trapped energetic particle fluxes in the radiation belts around the Earth as well as in a region near one of Jupiter's moons.

### *Earth's Inner Belt*

Earth's inner electron belt extends roughly between 2,000 and 4,000 km altitude at the magnetic equator. To estimate the size of the ES-RBR system required to remediate the flux of energetic electrons in this region to 1% of its initial level within a period of 30 days, we can use Eqns. (V.4) and (V.5) to first estimate the size of the plasma sheath that will form around the multi-wire electrostatic structure. The variation of the sheath size with applied bias voltage at an altitude of 3,000 km, where noon-time plasma densities are on the order of  $4 \times 10^9 \text{ m}^{-3}$ , is shown in Figure 15. We can then use Eqns. (IV.6) and (V.6) to estimate the number of satellites required to remediate the radiation belt. Figure 16 shows the variation with bias voltage of the number of ES-RBR spacecraft required to remediate the 1 MeV electron flux to 1% within 30 days, assuming each spacecraft deploys a 100-km long, 25-wire electrostatic structure. This analytical model predicts that only 4 ES-RBR spacecraft would be required if the structures are biased to 100 kV. This estimate is somewhat optimistic, due to the fact that this simplified analytical model neglects the fact that the orbital dynamics of the spacecraft and the rotation of the geomagnetic field with the Earth result in the spacecraft spending only a part of their orbit within the region we wish to remediate. These higher-order refinements will be addressed through numerical simulations in the following sections. Nonetheless, these simplified analytical methods indicate that the number of electrostatic spacecraft required to remediate the Earth's inner belt, and the amount of power required for each spacecraft, are both well within reasonable and affordable levels.

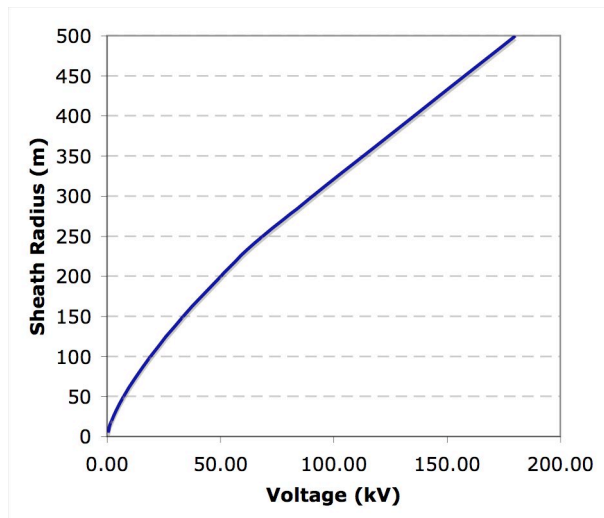


**Figure 15.** Variation of plasma sheath radius around the electrostatic structure with applied bias voltage.

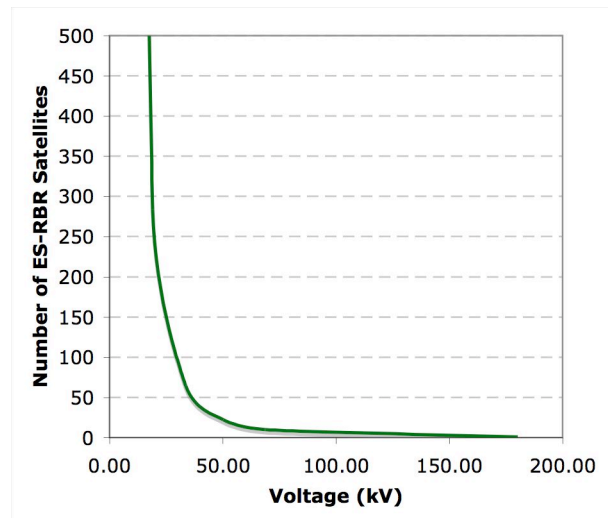


**Figure 16.** Number of ES-RBR systems required to remediate Earth's inner belt to 1% of original flux within 30 days, as a function of bias voltage.

### Remediating the Jovian Radiation Belts Around Europa's Orbit

Europa, the smallest of the four Galilean moons of Jupiter, is believed to have a water ocean below its icy surface, and it has a thin atmosphere containing oxygen. As a result, Europa is thought to be one of the most likely places in our solar system to host primitive extraterrestrial life, and might in the distant future be capable of supporting human habitation. Europa's orbit, however, lies near the outer edge of Jupiter's inner radiation belt, where the trapped energetic particle fluxes are quite intense. Pioneer 10's instruments measured electron fluxes at Europa's orbit range of over  $10^8 \text{ cm}^{-2}\text{s}^{-1}$  for particles with energies  $>0.16 \text{ MeV}$ , and over  $10^6 \text{ cm}^{-2}\text{s}^{-1}$  for particles with energies  $\geq 9 \text{ MeV}$ .<sup>22</sup> Because Europa's thin atmosphere blocks only a tiny portion of this flux, these radiation levels would pose an extreme challenge for any manned exploration or settlement of Europa's surface.

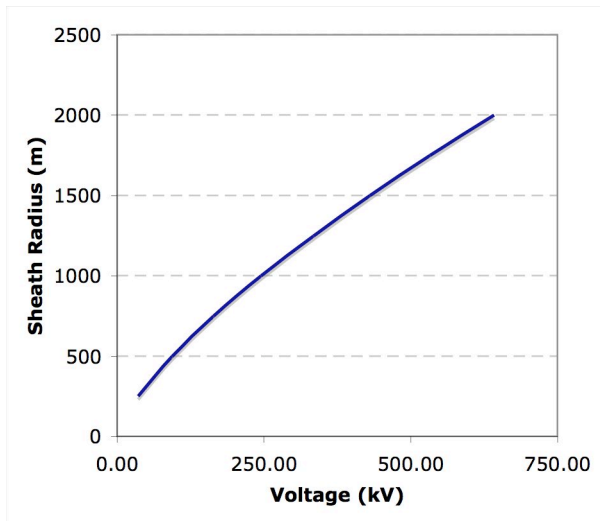


**Figure 17.** Variation of plasma sheath radius around the electrostatic structure with applied bias voltage.

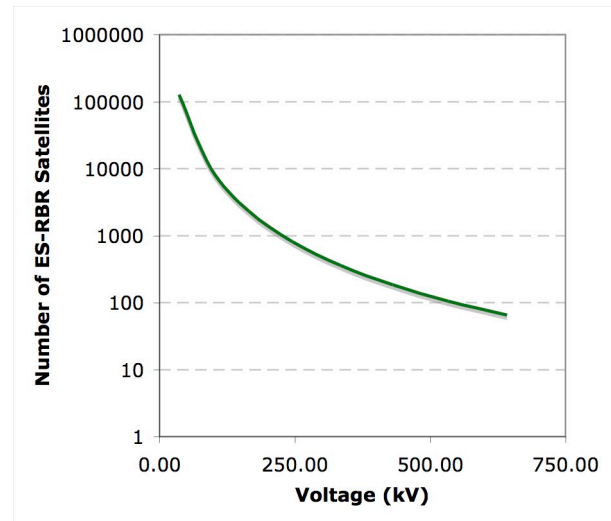


**Figure 18.** Number of ES-RBR systems required to remediate a 12,000-km wide section of Jupiter's radiation belt around Europa's orbit to 1% of original 1 MeV particle flux within 90 days, as a function of bias voltage.

We can investigate the feasibility of utilizing the electrostatic remediation technique to reduce radiation flux levels on Europa's surface by considering a system of  $N$  ES-RBR spacecraft, each with a 1000-km long tether, placed into orbit around Jupiter at altitudes that span a 12,000 km wide region around Europa's orbit. Again, we can use Eqns. (V.4) and (V.5) to first estimate the variation with bias voltage of the size of the plasma sheath that will form around the electrostatic structure. Europa orbits out at the edge of the Io plasma torus, where the plasma densities are relatively low, on the order of  $100 \text{ per cm}^{-3}$ , and the plasma temperatures are relatively warm, around  $20 \text{ eV}$ .<sup>23</sup> As a result of the low density and high temperature of the plasma, the sheath that forms around the electrostatic structure can be quite large, as shown in Figure 17. Because

22. Bolton, S.J., *et al.*, "Jupiter's Inner Electron Belts," *Jupiter*, Eds. Bagenal, Dowling, and McKinnon, Cambridge University Press, 2004, p. 676.

23. Thomas, N., *et al.*, "The Io Neutral Clouds and Plasma Torus," *Jupiter*, Eds. Bagenal, Dowling, and McKinnon, Cambridge University Press, 2004, p. 563.

the densities are so low, even though the tether length is 10x larger than that considered for the Earth belt remediation system, the power levels required for each spacecraft will still be on the order of a few kW. Because the scale of the Jovian radiation belts is so many times larger than Earth's radiation belts, the number  $N$  of ES-RBR spacecraft required to remediate even a "small" swath of the Jovian belts, as predicted by Eqns. (IV.6) and (V.6), is extremely large, approaching 'reasonable' levels of less than 100 only if the bias voltages exceed 0.5 MeV, as shown in Figure 18. This certainly would be a tremendous engineering challenge, and the costs would be commensurate with the challenge. However, if such a system could make Europa habitable for a human civilization in the far future, its costs may be justified by the benefits.

## VI. TETHER-PARTICLE INTERACTION FREQUENCY

For the remediation of the Earth's natural radiation belts, a high-voltage tether system is proposed to reduce the trapped energetic particle fluxes in the Van Allen radiation belts. The high-voltage tether structure will produce an intense electric field that will scatter charged particles into the loss cone where they will precipitate into Earth's atmosphere and dissipate their energy through collisions with atmospheric particles. In order for these particles to be scattered by the tether, they will need to pass within the tether's sphere of influence with a reasonable frequency. This model simulates the motion of the energetic particles and the electrostatic tether in order to determine the likelihood of interactions between the trapped particles and the tether system.

### VI.A. Particle Motion

The motion of energetic electrons and protons trapped in Earth's radiation belts is complicated. Particles gyrate around field lines, bounce up and down the field lines, and drift azimuthally around the Earth. The frequencies of these various motions depend on a particle's mass, energy, and orbital distance (L-shell). The motion of trapped electrons and protons was calculated using the equations below for a set of L-shell values and pitch angles.

#### *Particle Bounce Motion*

The trajectory of a particle's bounce motion is characterized by its pitch angle  $\alpha$ , which is a measure of the particles parallel to perpendicular velocity, and its L-shell parameter, which is the particle's equatorial distance from Earth in Earth radii. Using these two parameters, the particle's bounce period was calculated using:<sup>24</sup>

$$\tau_B \approx \frac{LR_E}{(W/m)^{1/2}} (3.7 - 1.6 \sin \alpha_{eq}) \quad (\text{VI.1})$$

where  $W$  is the particle's energy,  $m$  is the particle's mass, and  $R_E$  is the radius of the Earth (6371 km). The bounce period is the amount of time it takes the particle to travel from one mirror point, to the other mirror point, and then back to the first mirror point. In one bounce period, the particle will pass through the equator twice.

#### *Particle Drift Velocity*

In addition to gyrating and bouncing, trapped particles drift azimuthally around the Earth. The angular drift velocity is due to the magnetic field drift velocity, and can be approximated using:

$$\langle v_d \rangle \approx \frac{6L^2W}{qB_E R_E} (0.35 + 0.15 \sin \alpha_{eq}) \quad (\text{VI.2})$$

where the drift velocity of the particle depends on the particle charge  $q$ , particle energy  $W$ , and L-value, but not on the mass of the particle.

---

24. Baumjohann W., Treumann, R.A., *Basic Space Plasma Physics*, Chapter 3: Trapped Particles, Imperial College Press, 1996.

### VI.B. Particle Sample

The particles that we would most like to remediate are the high-energy (>1MeV) electrons and protons in the inner radiation belts (L=1.3-1.7) that pose the greatest potential hazard to spacecrafts. Given these L shell values, the loss cone angle for particles in this region can be calculated using:

$$\sin^2 \alpha_\ell = \frac{\cos^6 \lambda_E}{(1 + 3\sin^2 \lambda_E)^{1/2}} \quad (\text{VI.3})$$

where  $\lambda_E$  is the latitude at which a given L-shell intersects the Earth's surface:

$$\cos^2 \lambda_E = \frac{1}{L} \quad (\text{VI.4})$$

Thus, given a particle's L-shell value, the loss cone angle can be calculated and used as the minimum pitch angle value for particles in the sample. The pitch angles in the sample ranged from  $\alpha_\ell$  to 90 degrees for given values of L.

The bounce frequency for each particle was calculated using Eqn. (VI1) for specified L-shell and energy values. In this model, electrons with energies of 1 MeV and protons with energies of 10 MeV were considered.

### VI.C. Tether Motion

The orbital period of the tether around the Earth was calculated using:

$$\tau_T = \sqrt{2\pi \frac{(LR_E)^3}{\mu}} \quad (\text{VI.5})$$

where  $\mu = GM$ , the standard gravitational parameter ( $\mu = 3.986 \times 10^{14} \text{ m}^3/\text{s}^2$  for orbit around the Earth). Using Eqn. (VI2), the velocity of the tether was obtained for each specified L-shell.

### VI.D. Interaction Model

The model calculates the number of interactions that each particle in the sample has with the tether in a specified time period (nominally 24 hours), and stores this information in an array along with information regarding the particle's L-shell value, pitch angle, and bounce frequency. For a given time period, the program outputs 1) the range of tether interactions encountered by particles in the sample, 2) the number of particles that interacted with the tether at least once, 3) the number of particles that interacted with the tether at least five times, and 4) the number of particles that do not interact with the tether. The program then outputs 5) the mean number of interactions for sample particle in the given time period, 6) the mean bounce frequency value for the sample, and 7) the mean pitch angle value for the sample. The final value output is 8) the total number of particles considered in the sample. This program considers electrons with energies of 1MeV and protons with energies of 10 MeV.

Results for the interaction model are given below. Tables 1 and 3 give values for the mean number of interactions between the tether and trapped electrons and protons, respectively, for given L-shell values, along with percentages for the number of particles interacting and not interacting with the tether in each sample. Table 4 provides the same information but this time

the L-shell value is held constant at L=1.5 and the time period is varied from 1 day to 15 days. Tables 3 and 5 list the average values used for the trapped electrons and protons, respectively. Plots of the number of interactions vs. L-shell are given in Figure 19 and Figure 20 for varying time periods and particle energies.

**Table 2.** Electron interactions with the Tether System in one day.

L-Value	Mean # of Interactions	≥ 1 Interaction	No Interactions
1.3	13.4	98%	2%
1.4	11.6	98%	2%
1.5	10.2	98%	2%
1.6	8.9	98%	2%
1.7	7.9	97%	3%

**Table 3.** Average parameters for 1 MeV electrons

L-Value	Interactions (1 day)	Bounce Freq. (s <sup>-1</sup> )	Pitch Angle (Degrees)	Particles in Sample	Flux (El./cm <sup>2</sup> -s)
1.3	13.4	21.9	63.2	11238	2.88E5
1.4	11.6	20.1	60.6	12345	1.44E6
1.5	10.2	18.5	58.7	13178	1.97E6
1.6	8.9	17.2	57.1	13835	1.84E6
1.7	7.9	16.0	55.9	14370	1.32E6

**Table 4.** Proton interactions with the Tether System in one day.

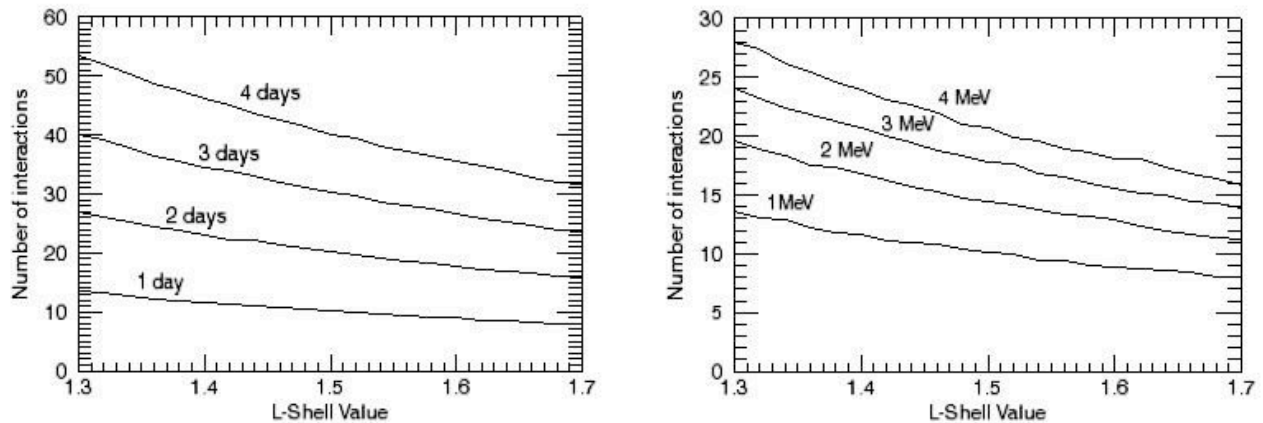
L-Value	Mean # of Interactions	≥ 1 Interaction	No Interactions
1.3	1.0	75%	25%
1.4	0.9	69%	31%
1.5	0.8	62%	38%
1.6	0.7	56%	44%
1.7	0.6	49%	51%

**Table 5.** Proton interactions with the Tether System for L = 1.5.

Days	Mean # of Interactions	≥ 1 Interaction	No Interactions
1	0.8	62%	38%
2	1.6	85%	15%
5	4.0	95%	6%
10	8.0	97%	3%
15	11.8	98%	2%

**Table 6.** Average parameters for 10 MeV protons.

L-Value	Interactions (1 day)	Bounce Freq. (s <sup>-1</sup> )	Pitch Angle (Degrees)	Particles in Sample	Flux (Pr./cm2-s)
1.3	1.0	1.62	63.2	11238	8.43E2
1.4	0.9	1.48	60.6	12345	6.48E3
1.5	0.8	1.37	58.7	13178	3.22E4
1.6	0.7	1.27	57.1	13835	6.07E4
1.7	0.6	1.18	55.9	14370	3.35E5


**Figure 19.** Average number of tether interactions (left) for 1 MeV electrons, (right) in 1 day

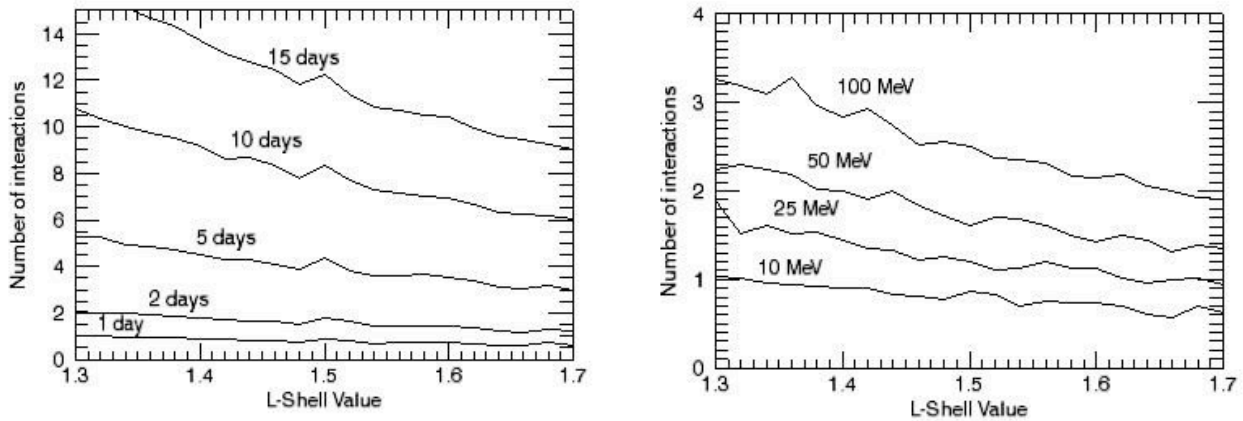


**Figure 20.** Average number of tether interactions (left) for 10 MeV protons, (right) in 1 day.

### VI.E. Analysis

While protons have an order of magnitude larger drift velocity and orbit the Earth  $10^1$  more times per day compared to electrons, the electrons, on average, cross the equator  $10^4$  times in one orbit compared to protons, which cross the equator  $10^2$  times per orbit. Thus, the electrons interact with the tether an order of magnitude more times that the protons interact with the tether. Looking at Table 2 and Table 4, this order of magnitude difference can be observed in the mean number of interactions. Nearly all the electrons will interact with the tether in one day (97%-98%) where as only 49% - 75% of protons interact with the tether in one day. However, over longer time periods (Table 5) most of the protons will eventually interact with the tether system (98% in 15 days).

The mean number of interactions found using this model is in agreement with the value estimated in the simplified analytical method used in Section IV. While some of the particles were found to be in resonance orbits, the motion of the tether ensures that all particles eventually interact with the tether system.

The number of interactions was found to increase with higher particle energy. According to the study by Minor<sup>15</sup> the change in pitch angle and its standard deviation decrease with increased energy. This suggests that remediation of energetic protons could take longer than remediation of energetic electrons.

## VII. ENERGETIC PARTICLE DECAY CALCULATIONS

To predict the efficiency of tether based remediation efforts, we developed a simulation tool to investigate the expected interaction and decay rates of energetic electrons with electrostatic structures in orbit around the Earth. This tool incorporates results from several different models, including data from ESA's Space Environment Information System (SPENVIS) and pitch angle scattering results calculated using a model of the interaction of energetic electrons with a high voltage tether structure's sheath.<sup>15</sup> Using these models, the tool calculates the number of particles that would interact with the tether in a given orbit, monitors the change in pitch angle observed during each interaction, and explores remediation timescales by observing the time required for particles' pitch angles to be scattered into the loss cone where the particles are lost to Earth's atmosphere. Figure 21 illustrates how the various models are combined to enable calculation of the effect of a given ES-RBR system on radiation belt fluxes.

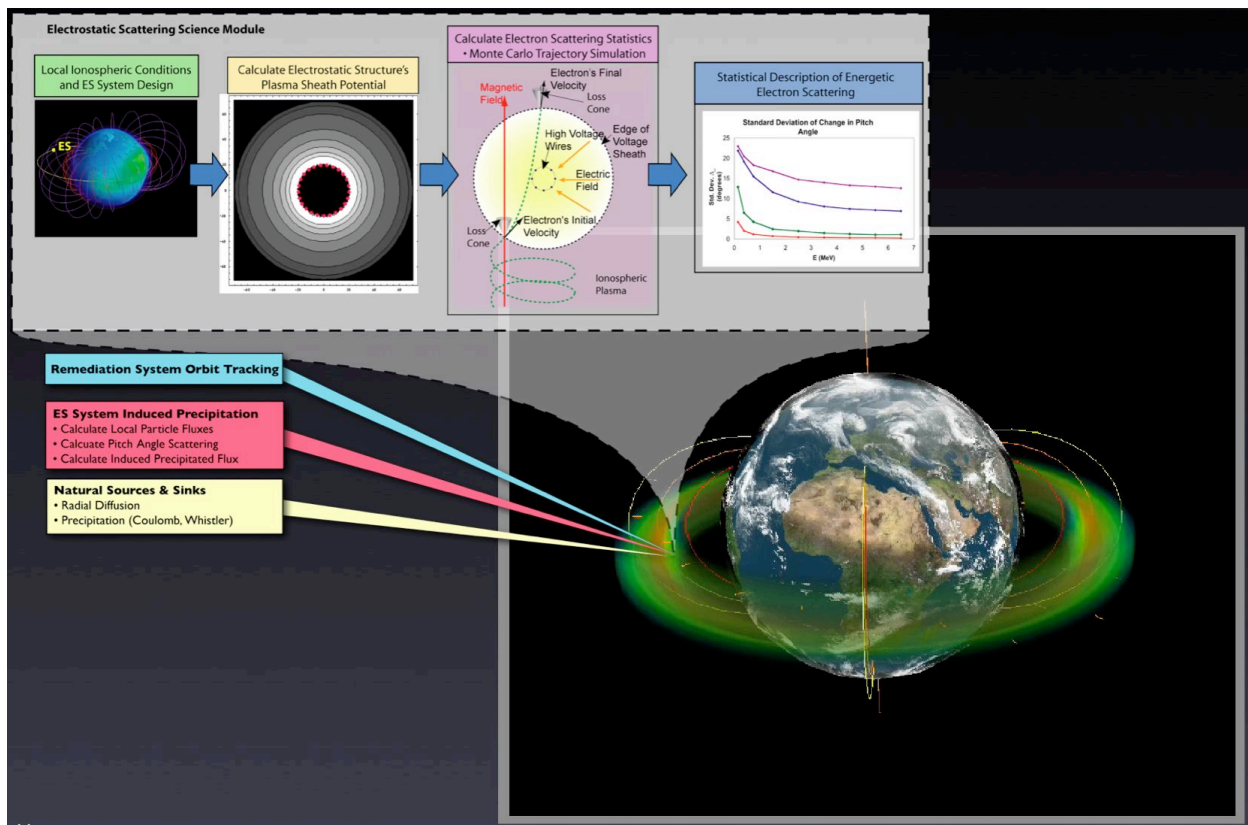


**Figure 21.** Illustration of the models combined in the ES-RBR simulation tool.

This section discusses the following: 1) determination of the initial particle flux in the radiation belt region suggested for remediation, 2) calculation of tether orbits and the particle flux encountered by the tethers in the given orbits, 3) discussion of the use of magnetic flux tubes to compare the radiation belt flux to the flux experienced by the tether in its orbit, 4) computation of the rate at which radiation belt particles interact with the tether, 5) simulation of the changing particle pitch angle distribution from particle-tether interactions, and 6) estimation of particle decay rates utilizing the above calculations and results. **These initial results consider > 1 MeV electrons residing in the inner radiation belt.** In this section, we will look at ES-RBR system

performance without considering the effects of natural source and sink terms. In the following section, we will add these terms to the models to obtain more accurate results.

### VII.A. Initial Particle Flux

To calculate the initial density of particles within Earth's inner radiation belt, we used ESA's Space Environment Information System (SPENVIS) website,<sup>25</sup> an interface to several space environment models including natural radiation belt models. The SPENVIS trapped particle flux model is a compilation of several proton and electron models including: AP-8,<sup>26</sup> CRRESPRO,<sup>27</sup> SAMPEX/PET low altitude model,<sup>28</sup> AE-8,<sup>29</sup> CRRESELE,<sup>30</sup> and ESA-SEE1 model, an update of AE-8 MIN.<sup>31</sup>

The AP-8 model consists of maps containing omnidirectional, integral proton fluxes in the energy range 0.1 MeV to 400 MeV in the Earth's radiation belts, and the AE-8 model contains omnidirectional, integral electron flux maps for the energy range of 0.04 MeV to 7 MeV. The maps are based on data collected in the early sixties to mid-seventies from over 20 satellites. In these models, flux values are stored as a function of L-value, energy, and  $B/B_{eq}$ , where  $B_{eq} = 0.311653/L^3$ . The CRRESPRO and CRRESELE models were developed by the Air Force Research Laboratory (AFRL) and are based on data collected by the CRRES satellite. The ESA-SEE1 model is an update to the AE-8 MIN model representing a major improvement to the AE-8 model at high energies  $>2$  MeV; the ESA-SEE1 model is based on CRRES electron spectrometer flux data at five energies and at six L-values and is not just an extrapolation of unknown validity like the previous version of AE-8.

Using the SPENVIS trapped particle flux model, forty-one omnidirectional electron fluxes were obtained for L-values ranging 1.3 to 1.7, an integral energy value of  $>1$  MeV, and  $B/B_{eq}$  value of 1, resulting in a particle flux profile for  $>1$  MeV electrons along the magnetic equator (Fig. 1). The particle flux profile was taken at  $8.7^\circ$  S,  $249.2^\circ$  E for altitudes from  $\sim 1,900$  km to 4,500 km. Flux values were determined every 64 km providing data points at L-value intervals of 0.01 along the magnetic equator.

---

25. www.SPENVIS.com

26. Sawyer, D. M., and J. I. Vette, AP-8 Trapped Proton Environment for Solar Maximum and Solar Minimum, *NSSDC/WDC-A-R&S 76-06*, 1976.

27. Meffert, J. D., and M. S. Gussenhoven, CRRESPRO Documentation, PL-TR-94-2218, *Environmental Research Papers, 1158*, Phillips Laboratory, 1994.

28. Heynderickx, D., M. Kruglanski, V. Pierrard, J. Lemaire, M. D. Looper, and J. B. Blake, A Low Altitude Trapped Proton Model for Solar Minimum Conditions Based on SAMPEX/PET Data, *IEEE Trans. Nucl. Sci.*, *46*, 1475, 1999.

29. Vette, J. I., The AE-8 Trapped Electron Model Environment, *NSSDC/WDC-A-R&S 91-24*, 1991.

30. Brautigam, D. H., and J. T. Bell, CRRESELE Documentation, PL-TR-95-2128, *Environmental Research Papers, 1178*, Phillips Laboratory, 1995.

31. Vampola, A. L., Outer Zone Energetic Electron Environment Update, Final Report of ESA/ESTEC Contract No. , 1996

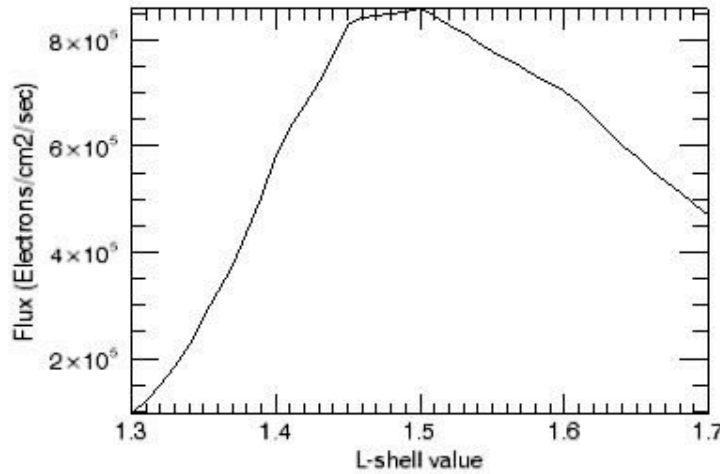


**Figure 22.** Equatorial electron flux profile in the inner belt region.

### VII.B. Tether Orbit

For these initial calculations, the tethers are put in a slightly inclined orbit with a perigee of 2000 km and an apogee of 4400 km in order to effectively survey the radiation belt region of interest. The orbital generator in SPENVIS was used to obtain tether position coordinates for a nominal one-year mission duration. Coordinates were calculated at 60-second intervals for five 4-day segments, the maximum segment length allowed by the SPENVIS orbital generator. Segments were calculated at one-month intervals to obtain a variety of orbital coordinates. The model cycles through the 30,000 tether positions for calculations exceeding 20 days. Orbital input parameters are listed in Table 1.

**Table 7.** Electrostatic System Orbital Parameters.

Apogee	4400 km
Perigee	2200 km
Inclination	8.70°
Ascending Node	339.20°
True Anomaly	0.00°
Eccentricity	0.11
Period	2.59 hrs

These orbital coordinates were then input into the ESA-SEE 1 and the AP-8 models to obtain the trapped electron and proton fluxes for each time step along the tether orbit. Particle flux values were obtained for 30 energy values ranging from 0.04 to 7 MeV for electrons and from 0.1 to 400 MeV for protons. Initially, we only consider electron fluxes for particles with energies >1 MeV, the same energy range considered for the radiation belt particle flux. The orbits of the tethers span L-shells from 1.27 to 1.83; only when a tether is in the region of interest (1.3-1.7) are the particle-tether interactions calculated.

### VII.C. Magnetic Flux Tubes

To aid in comparing the density of particles in the radiation belts to the density of particles encountered by the tether, we employ the use of magnetic flux tubes. A magnetic flux tube encloses a single set of field lines with a closed contour and all physical quantities of the tube, such as field strength and density, are assumed constant over the tube cross-section and only vary spatially along the length of the tube. Thus, by considering a flux tube of  $1 \text{ cm}^2$  at each of the 41 L-shell values for which initial particle fluxes were obtained (see §1), an orbiting tether, within the region of interest, can be associated with one of these 41 flux tubes for each time step (Fig. 2).

The number of energetic particles in a magnetic flux tube can be found by multiplying the integral electron flux by the full particle bounce period for a given L-value and energy (Voss *et al.*, 1998).

$$N(E, L) = 2\pi \int_0^{\pi/2} j_{eq}(\alpha_{eq}, E) \tau_b(\alpha_{eq}, E) \cos(\alpha_{eq}) \sin(\alpha_{eq}) d\alpha_{eq} \quad (\text{VII.1})$$

In the above equation,  $j_{eq}$  is the differential, directional, electron flux at the magnetic equator as a function of the equatorial pitch angle  $\alpha_{eq}$ . The particle bounce period  $\tau_b$  is the time it takes each particle to travel along the flux tube exactly twice. Using flux values obtained from SPENVIS and calculating the particle bounce period, the number of **electrons with energies > 1MeV** in a  $1\text{-cm}^2$  cross-sectional area perpendicular to the magnetic field can be determined for each of the 41 equatorial<sup>32</sup> flux tubes.

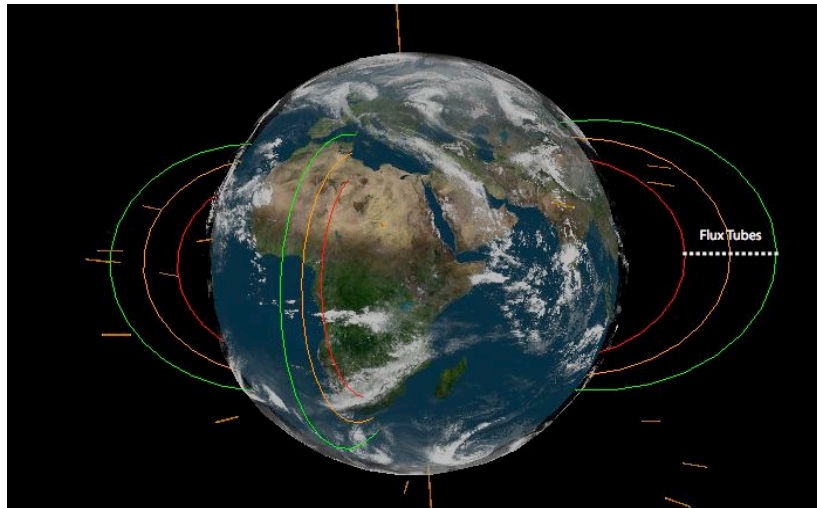


**Figure 23.** Flux tube locations w.r.t. magnetic field lines at  $L=1.3, 1.5,$  and  $1.7$ .

At each orbital time step, the tether is associated with one of the 41 equatorial flux tubes nearest to tether's midpoint field line location. The flux experienced by the tether is mapped back to the magnetic equator by multiplying the measured flux by the ratio of the magnetic field magnitude at the equator to the magnetic field magnitude at the location of the tether. The number of particles in the tether's magnetic flux tube can then be determined using the method described

32. Throughout this section *equatorial* refers to the magnetic equatorial plane unless otherwise specified.

above (Eq 1). The number of particles in the tether’s flux tube is assumed to be the number of particles that will interact with the tether in a 1-cm<sup>2</sup> area at the location of the tether. This is a reasonable approximation because one tether spans  $2.0 \times 10^{11}$  flux tubes, so the average number of particles passing through the tether sheath does not require a given flux tube to remain in one position for full bounce period.

**VII.D. Interaction Rate**

The percentage of particles interacting with the tether for a given time step is computed by multiplying the number of particles that interact with the tether in one 1-cm<sup>2</sup> equatorial flux tube by the ratio of the tether interaction cross-section area,  $A_T$ , to the cross-sectional area of the equatorial radiation belt for the given L-shell,  $A_{RB}(L)$ .

$$A_T = N_T(2\rho_{sheath}L_T) \tag{VII.2}$$

$$A_{RB}(L) = \pi[(R_E(L + 0.01))^2 - (R_EL)^2] \tag{VII.3}$$

In Eq 2,  $N_T$  is the number of tether systems in orbit,  $\rho_{sheath}$  is the sheath radius of the tether, and  $L_T$  is the tether length. For the purposes of these calculations, we assume 25 orbiting tethers each with a length of 100 km and a sheath radius of 100 m (Fig. 3). In Eq 3,  $R_E$  is the radius of the Earth and L is the L-shell value. By multiplying the particle-tether interactions for one flux tube by the ratio of the number of flux tubes that cover the tether’s area to the number of flux tubes that cover the cross-sectional area of a small sub-region of the radiation belts, we can obtain an average number of interactions per flux tube per unit time.

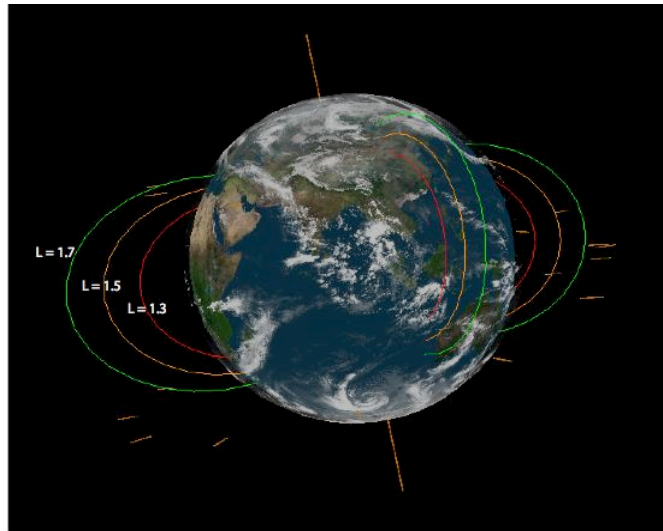


**Figure 24.** 25 Electrostatic tether structures in orbit around the Earth.

Computing the average number of particle interactions per flux tube per unit time allows the immense energetic particle population to be modeled as to a much smaller sample, allowing for easier calculations while still accurately representing the physical situation. To obtain the number of particles interacting with the tether in each orbital time step, the average number of interactions is multiplied by 60 seconds, the time interval between orbital data points.

To test the validity of this model, results are compared with Global System Interaction Model results described by Minor (2004). Using a system of 10 tethers of length 100 km and sheath radius of 100 m, Minor predicted that it would take 1653 seconds to obtain a 10% interaction rate for 1 MeV electrons in a 1000 km wide radiation belt centered at  $L=1.5$ . Assuming the same model set up as Minor (2004), we compute an 11% interaction rate in 1653 seconds. These results assume that the tether encounters the same particle flux as the flux passing through the equatorial magnetic flux tubes.

If the particle flux predicted by the SPENVIS model for the orbital parameters described in §2 is applied to these calculations, then we calculate an interaction rate of 9%. This discrepancy can be explained by the variation in flux values resulting from the tether's orbital inclination. The location of the tether in its orbit significantly affects the amount of flux the tether encounters. The more inclined the orbit above the magnetic equatorial plane, the greater the difference between the equatorial flux and the flux observed by the tether.

### VII.E. Pitch Angle Scattering

In order to accurately determine particle decay rates, an understanding of tether-particle pitch angle scattering is essential. Building on the work of Minor,<sup>15</sup> we investigate the changing pitch angle distribution and analyze the rate at which energetic particles are scattered into the loss cone

Limiting our particle sample to those within a  $1\text{-cm}^2$  equatorial flux tube enables us to track the change in particle pitch angle for each electron interaction with the tether at every time step. In our model, the equatorial flux tubes can have up to 100,000 particles, each with an initial pitch angle value  $\alpha$  randomly assigned in the range

$$\alpha_{Loss} \leq \alpha \leq (\pi - \alpha_{Loss}) \quad (\text{VII.4})$$

where  $\alpha_{Loss}$  is the loss cone value for particles at the given L-shell. To accurately model particle scatter into the loss cone, the pitch angle of each particle in an equatorial flux tube needs to be assigned a value, and the change in pitch angle needs to be followed throughout every time step.

For each step, particles interacting with the tether were assigned a change in pitch angle  $\Delta\alpha$  according single event scattering results presented by Minor. In his report, Minor provides a mean and standard deviation of pitch angle change for 9 energy and 2 L-values. Values used in our initial calculations are  $\mu = -0.48$  and  $\sigma = 11.2$ , which correspond to an L-shell of 1.5 and an energy of 0.75 MeV. After the change in pitch angle is added to the pitch angle values of the interacting particles, any particles scattered into the loss cone, represented by

$$\alpha \leq \alpha_{Loss} \quad \text{or} \quad \alpha \geq (\pi - \alpha_{Loss}), \quad (\text{VII.5})$$

are considered lost to the atmosphere and are removed from the system. The pitch angle values of the remaining particles are stored and used the next time the tether is in the given flux tube.

A plot of the pitch angle distribution with time for a 10% particle interaction rate is shown in Figure 25. Each distribution is separated by 45 hours with a total simulation time of just over 11 days. The red box represents the initial, uniform pitch angle distribution described by Eq (VII.4). In the first time step (the orange curve), the sides of the distribution are dramatically reduced; these particles lost to the Earth's atmosphere. For successive time steps, the amount of loss decreases as the particles with pitch angles near the center of the distribution must randomly walk to the sides in order to be lost. Between the fifth and sixth time steps (the purple and pink

curves, respectively), only a very small decrease in the number of particles is observed. This decrease in the number of particles lost with time can also be observed in Figure 26 for a 347 day run.

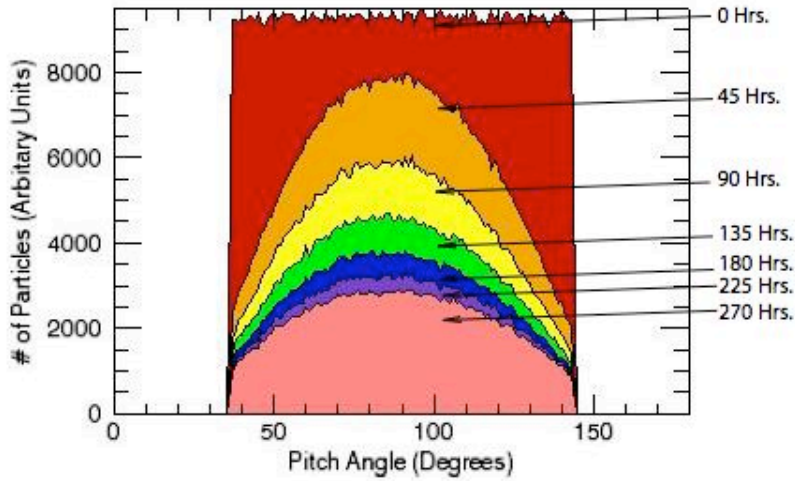


**Figure 25.** Evolution of an initial ‘top-hat’ pitch angle distribution for a 10% interaction rate for equal time steps.

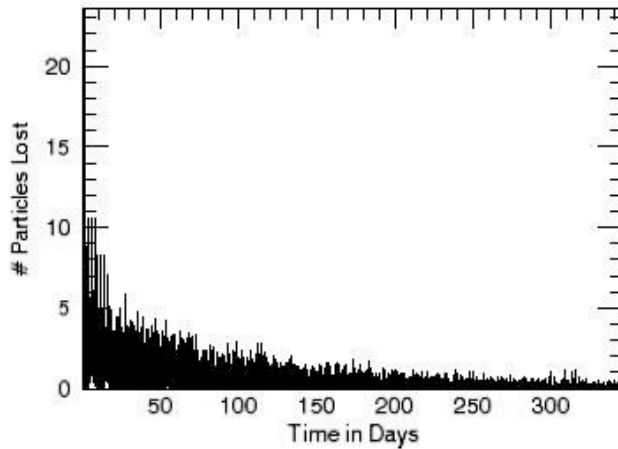


**Figure 26.** Number of particles removed from the belt at each time step.

**VII.F. Particle Decay Rate**

The decay rate of particles in the radiation belts is calculated for 50,000 time steps. For each time step, the number of particles lost are subtracted from the total number of particles in a given flux tube. The particles in all flux tubes are summed and divided by the total, initial, energetic electron population. The percentage of particles remaining after each time step is recorded in the program; the results are plotted in Figure 27.

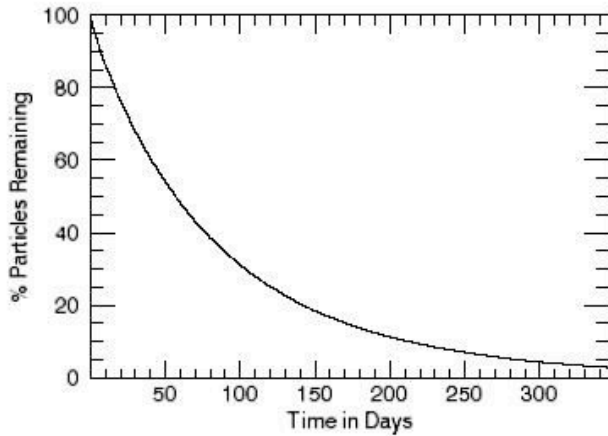


**Figure 27.** Decay of particle fluxes in the inner belt region for all L-shell values combined.

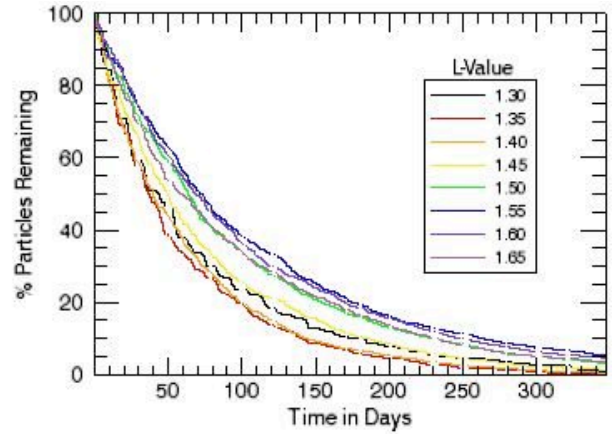


**Figure 28.** Decay of particle fluxes in the inner belt region for discrete L-shell values.

After 347 days, 97.3% of the Earth's natural radiation belts at altitudes between 1,900 km and 4,500 km is remediated. All 41 flux tubes experienced some loss, and the decay rate for a few selected flux tubes is shown in Figure 28.

The orbits of the tethers passed through L-shells ranging from 1.27 to 1.83, and therefore, they were not always in the region of interest (1.3-1.7). The tethers were outside this range for 12,828 out of 50,000 time steps, resulting in remediation occurring only 74.34% of the time. Taking these orbital considerations into account, we might expect the same degree of remediation in 258 days if the tethers spend their entire orbit within the region of interest.

To obtain a diffusion coefficient that describes the decay of the radiation belt electron population due to remediation by the system of tethers, we use

$$\frac{N_{eTotal}(t)}{N_{eInitial}} = \Omega_e(t) = e^{-\gamma_e t} \quad (\text{VII.6})$$

where  $N_{eInitial}$  is the initial number of electrons in all 41 flux tubes and  $N_{eTotal}(t)$  is the total number of electron remaining in the flux tubes at a time  $t$ . By plotting the natural log of the particle decay rate  $N(t)/N_{Initial}$ , a linear least squares fit can be used to find the diffusion coefficient  $\gamma$  (Fig. 7). The diffusion coefficient fit for Figure 27 was  $\gamma = -0.01 \text{ days}^{-1}$ .

Comparing these results to those obtained by Minor, we find our calculations predict a much larger remediation time. Minor concluded that 90% of the radiation belts would be remediated after  $\sim 25$  days, and he found a diffusion coefficient fit of  $\gamma = -0.087 \text{ days}^{-1}$ . These differences might be explained by the inclusion of the tether orbital motion, which is inclined and is not always in the magnetic equatorial plane. This could result in smaller fluxes at the tether's position compared with equatorial flux values.

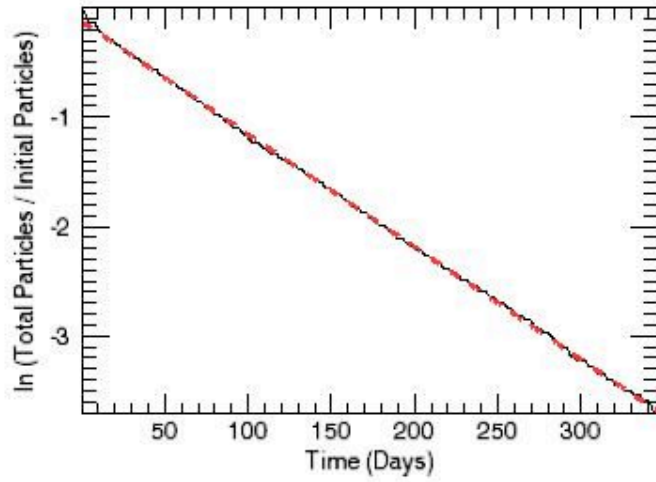


**Figure 29.** Linear least-squares fit (red dashed line) for the decay of energetic particles in the radiation belts.

## VIII. RADIATION REMEDIATION SIMULATIONS

To further refine our radiation belt remediation (RBR) predictive model, natural source and sink terms were included. These models were run for energetic electrons and protons in the Earth's radiation belts and the expected energetic particle remediation timescales were calculated for both species. Diffusion coefficients describing the decay of the radiation belt electron and proton population were also determined to compared to results previously predicted by Minor (2004).

### VIII.A. Tether Orbits

A slightly different orbital configuration is used in the following calculations compared to previous simulations. The tethers are placed in an equatorial orbit and remain within  $8.7^\circ$  of the magnetic equator throughout their orbits. A constellation of 25 tethers is used with the tether systems in one of two possible orbits: 15 of the tethers are place in an orbit with a perigee of 1900 km and an apogee of 4400 km, these tethers cover L-shells from  $L=1.3$  to  $1.7$ , the remaining 10 tethers are placed an orbit with a perigee of 3000 km and an apogee of 400 km in order to concentrate remediation at higher L-shell ( $L = 1.5 - 1.7$ ).

The orbital generator in SPENVIS was used to obtain tether position coordinates for a nominal one-year mission duration. Coordinates were calculated at 60-second intervals for five 4-day segments, the maximum segment length allowed by the SPENVIS orbital generator. Segments were calculated at one-month intervals to obtain a variety of orbital coordinates. For calculations exceeding 20 days, the model cycles through the 30,000 SPENVIS-generated tether positions. Orbital input parameters are listed in Table 1.

**Table 8.** ES-RBR Remediation System Parameters Used In Analysis

Number of Tether Systems	15	10
Apogee	4400 km	4000 km
Perigee	1900 km	3000 km
Inclination	$0.00^\circ$	$0.00^\circ$
Ascending Node	$0.00^\circ$	$0.00^\circ$
True Anomaly	$0.00^\circ$	$0.00^\circ$
Eccentricity	0.13	0.05
Period	2.57 hrs	2.71 hrs

These orbital coordinates were then input into the ESA-SEE 1 and the AP-8 models to obtain the trapped electron and proton fluxes for each time step along the tether orbit. Particle flux values were obtained for 30 energy values ranging from 0.04 to 7 MeV for electrons and from 0.1 to 400 MeV for protons. In this analysis we consider electron fluxes for particles with energies  $>1$  MeV and proton fluxes  $>7$  MeV.

### VIII.B. Electron Decay Rate

The decay rate of electrons in the radiation belts is calculated for 23,000 60-seconds time steps. For each time step, the number of particles lost are subtracted from the total number of particles

in a given flux tube. The particles in all flux tubes are summed and divided by the initial energetic electron population. The percentage of particles remaining after each time step is recorded and used in subsequent calculations. The results plotted in Figure 30 consider remediation effects resulting solely from a constellation of 25 orbiting tethers; these graphs do not account for natural source and sink terms.

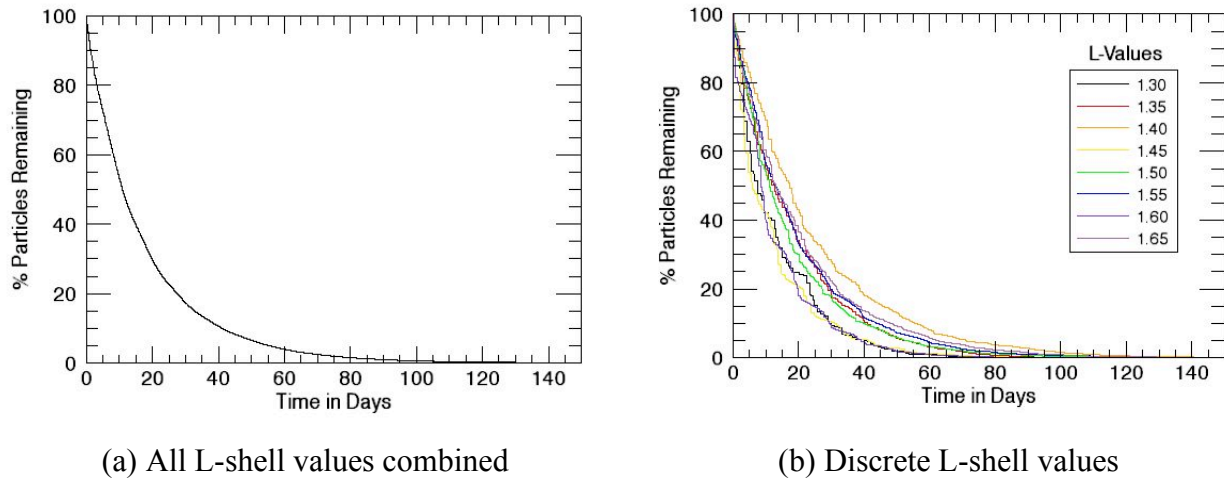


**Figure 30.** Decay Rate for Electrons in the Radiation Belts ( $L=1.3$  to  $1.7$ ), Natural Source and Sink Terms Not Included.

After 105 days, less than 1% of the Earth's natural radiation belts remain. After 150 days, 99.8% of the of the Earth's natural radiation belts at equatorial altitudes between 1,913 km and 4,464 km have been remediated. All 41 flux tubes experienced some loss, and the decay rate for selected flux tubes is shown in Figure 30(b).

The orbits of the tethers passed through L-shells ranging from 1.26 to 1.83 and the tethers are, therefore, not always in the region of interest (1.3-1.7). The tethers were outside this range for 6,600 out of 115,000 orbital time steps (we consider 5 orbits of 23,000 time steps each), resulting in remediation occurring 94.26% of the time. Taking these orbital considerations into account, we might expect the same degree of remediation,  $\sim 99\%$ , in 98 days if the tethers spend their entire orbit within the region of interest; again, these calculations do not include natural source and sink terms.

The diffusion coefficient that describes the decay of the radiation belt electron population due to remediation by the system of tethers is obtained using

$$\frac{N_{e_{Total}}(t)}{N_{e_{Initial}}} = \Omega_e(t) = e^{-\gamma_e t} \quad (\text{VIII.1})$$

where  $N_{e_{Initial}}$  is the initial number of electrons in all 41 flux tubes and  $N_{e_{Total}}(t)$  is the total number of electron remaining in the flux tubes at a time  $t$ . By plotting the natural log of the particle decay rate  $N(t)/N_{Initial}$ , a linear least squares fit can be used to find the diffusion coefficient  $\gamma$  as shown in Figure 31. The diffusion coefficient fit for Figure 30 was  $\gamma = -0.039 \text{ days}^{-1}$ .

Comparing these results to those obtained by Minor,<sup>15</sup> we find our calculations predict a much larger remediation time. Minor concluded that 90% of the radiation belts would be remediated

after ~ 25 days, and he found a diffusion coefficient fit of  $\gamma = -0.087 \text{ days}^{-1}$ . These differences might be explained by the inclusion of the tether orbital motion, which is inclined to the magnetic equatorial plane and not always in the L-shells of interest. This could result in smaller fluxes at the tether's position compared with magnetic equatorial flux values.

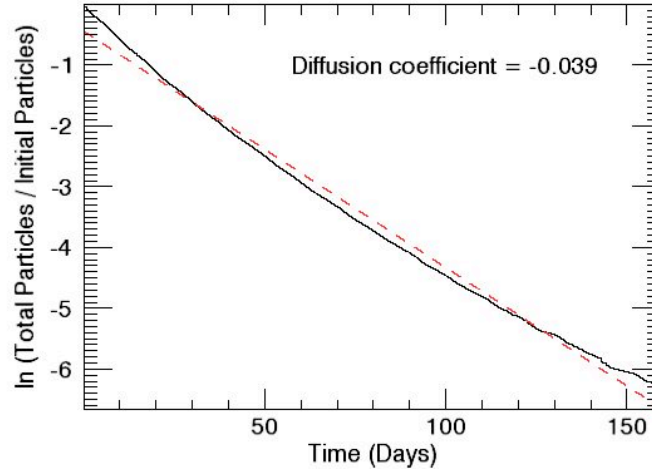


**Figure 31.** Linear Least Squares Fit (red dashed line) for the Decay of Energetic Electrons in the Radiation Belts.

In order to compare these results to the natural loss rate, an understanding of electron sources and sinks in the inner radiation belt is essential. To begin, we disregard the source term and study the natural electron sink term, comparing the natural decay rate to the RBR case. In our model the natural sink term is obtained using particle precipitation lifetimes.<sup>33</sup> Inward radial diffusion has also been included in the model; the radial-diffusion velocity,  $v_r$ , defined as the motion of the logarithmic half-minimum, is given by,

$$v_r = 1.6 \times 10^{-6} L^8, \tag{VIII.2}$$

where  $L$  is the L-shell value and  $v_r$  is given in terms of  $R_E/\text{day}$ .<sup>34</sup> Frank found that the inward-diffusion velocities for two separate events were the same at the same L-values, suggesting that the process of radial diffusion is a fairly typical one.<sup>35</sup>

Including the natural sink term and inward radial diffusion, the decay rate for electrons in the radiation belts is again calculated for 23,000 600-second time steps. For each time step, natural particle losses are added to the number of particles lost due to remediation. The total number of particles lost is then subtracted from the current number of particles in the flux tube. Particles that diffuse inward are subtracted from the outer flux tube and added to the number of particles trapped in the preceding flux tube. The graphs in Figure 32a show the decay rate for energetic particles trapped in the inner radiation belts due to natural sinks (blue dotted line) and due to

---

33. Abel, B., and R. M. Thorne, Electron scattering loss in Earth's inner magnetosphere, 1. Dominant physical processes, *J. Geophys. Res.*, 103, 2385-2396, 1998.  
 34. Hess, W. N., *The Radiation Belt and Magnetosphere*, Blaisdell Publishing Company, Waltham, Massachusetts, 1968.  
 35. Frank, L. A., *Inward Radial Diffusion of Electrons  $E > 1.6 \text{ Mev}$  in the Outer Radiation Zone*, Univ. of Iowa Report 65-13 (1965).

RBR effects (black solid line). In Figure 32, an energetic particle source term has not been included.

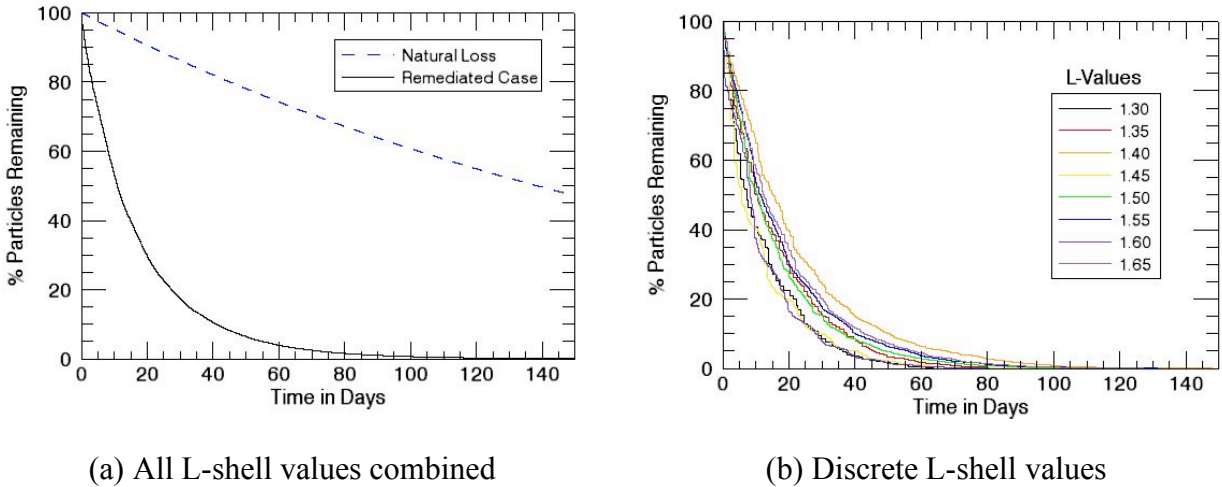


**Figure 32.** Decay Rate for Electrons in the Radiation Belts (L=1.3 to 1.7), Natural Sink Terms Included, Source Terms Not Included.

Using a linear least squares fit as described above, a diffusion coefficient  $\gamma$  was obtained for both the natural loss case and the radiation belt remediation case. Figure 33 illustrates the order of magnitude increase in electron precipitation using a radiation belt remediation system. The natural loss diffusion coefficient is  $\gamma = -0.005 \text{ days}^{-1}$  (blue line) while the diffusion coefficient due to a tether-based radiation belt remediation system is  $\gamma = -0.044 \text{ days}^{-1}$  (black line). These results suggest that a constellation of orbiting tethers has tremendous potential for effectively remediating Earth’s natural radiation belts, however to assess the true efficiency of the system, the rate at which energetic particles enter into the radiation belts and become trapped must also be taken into account.

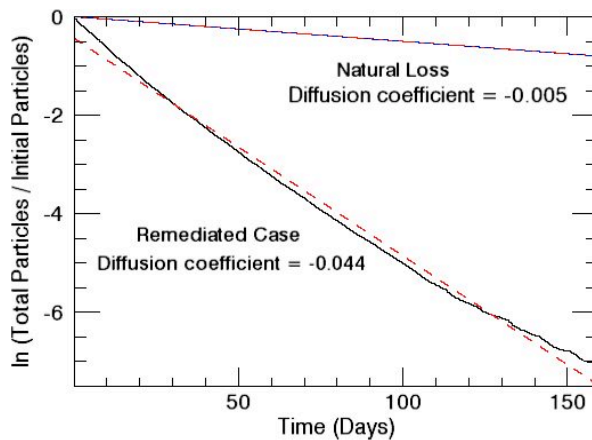


**Figure 33.** Linear Least Squares Fit (red dashed line) for the Decay of Electrons in the Radiation Belts due to Natural Loss (blue line) and Remediation (black line).

To characterize the behavior of energetic electrons in the inner radiation belts we rely on data obtained by the Solar, Anomalous, and Magnetospheric Particle Explorer SAMPEX, a spacecraft that measures energetic electrons from a low-altitude, 520-675 km, 82-degree inclined orbit.<sup>36</sup> Daily electron fluxes for 2-6 MeV electrons were obtained for the 12-year period from July 1992 to March 2004 (courtesy of A. Lui). Data for the inner radiation belt and the slot region ( $L = 1.2 - 2.5$ ) from July 2002 to March 2004 is plotted in Figure 34 and in Figure 35 data for the inner radiation belts ( $L = 1.2 - 1.9$ ) is plotted for January 2000 to March 2004.

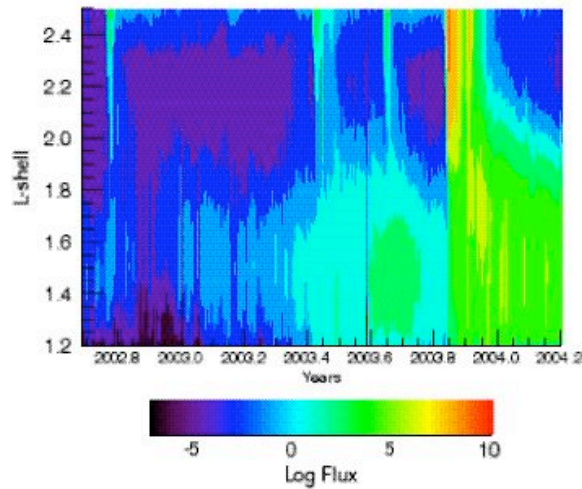


**Figure 34.** Logarithmic Value of the 2-6 MeV Daily Averaged Electron Fluxes from July 2002 to March 2004 (in  $\text{cm}^{-2} \text{s}^{-1} \text{sr}^{-1} \text{MeV}^{-1}$ )

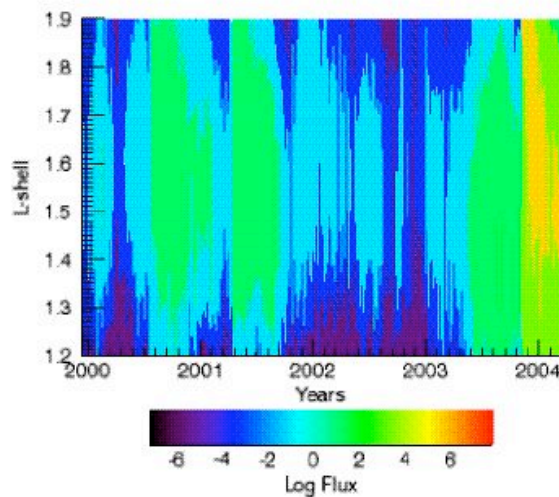


**Figure 35.** Logarithmic Value of the 2-6 MeV Daily Averaged Electron Fluxes from Jan 2000 to March 2004 (in  $\text{cm}^{-2} \text{s}^{-1} \text{sr}^{-1} \text{MeV}^{-1}$ )

36. Baker, D. N, S. G. Kanekal, X. Li, S. P. Monk, J. Goldstein, and J. L. Burch, An extreme distortion of the Van Allen belt arising from the ‘Halloween’ solar storm in 2003, *Nature*, 432, 878, 2004.

The SAMPEX data, discussed in greater detail in Baker *et al.*<sup>36</sup> and Zheng *et al.*,<sup>37</sup> indicate the source of energetic electrons in the inner radiation belts is not a slow, constant source but a rather a rapid injection of particles followed by a period of decay. Baker *et al.* and Zheng *et al.* suggest such a rapid injection of particles into the inner belts may result from significant geomagnetic storms. The sources are sporadic events with massive storms occurring approximately six times between 1992 and 2004.

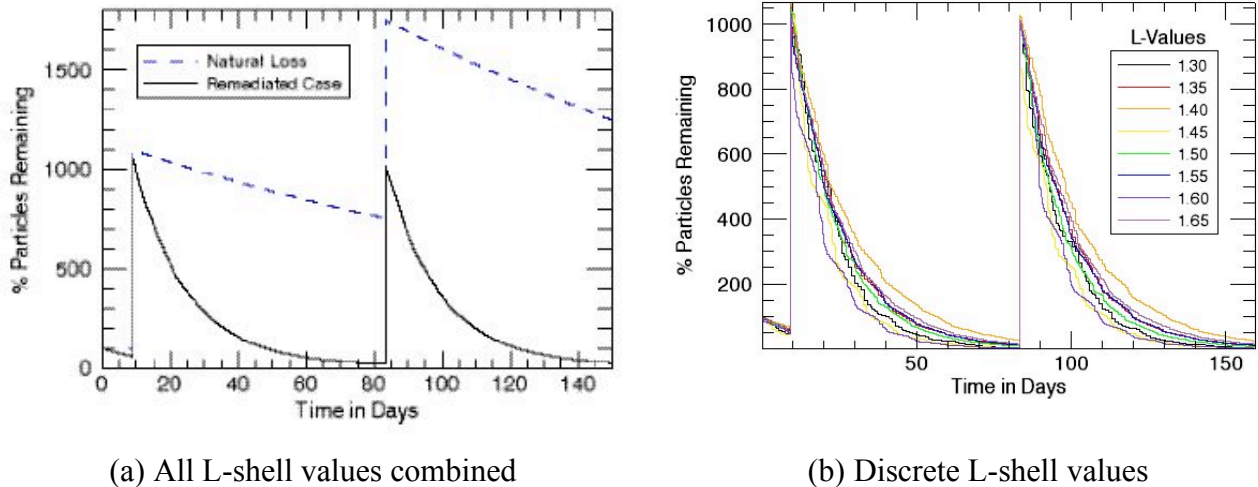
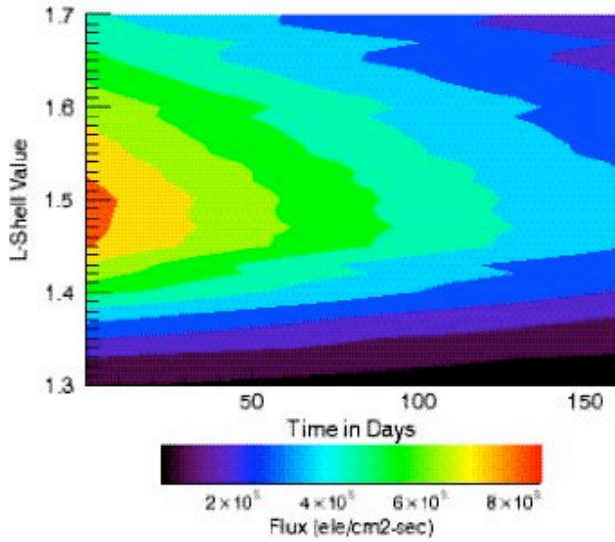


**Figure 36.** Electron flux in the inner belt region during a solar active period, natural source and sink terms included.

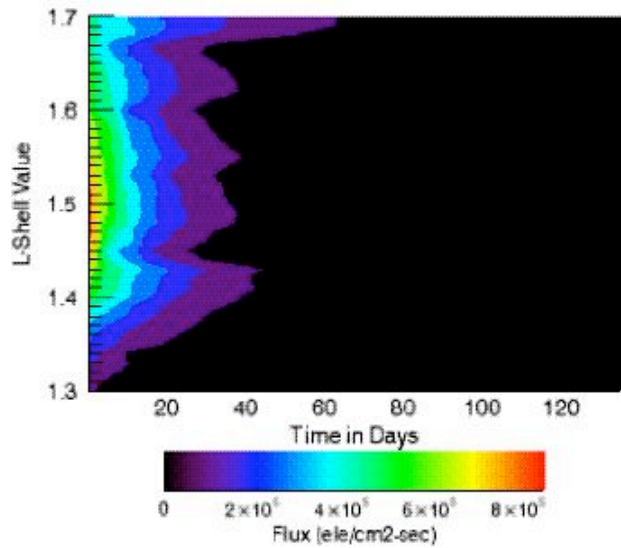
To add a discrete source term that imitates the natural variation in the inner radiation belt energetic particle population, we assume two large solar events, one occurring nine days and one occurring 83 days after the start of the simulation. The large storms depicted in Zheng *et al.*<sup>37</sup> increase the number of particles trapped in the inner belts by roughly an order of magnitude. In our model, each geomagnetic storm injects 10 times the initial number of particles over L-shells 1.3 to 1.7. The first injection occurs at  $t = 9$  days after the start of remediation and the second storm injects the same number of particles at  $t = 83$  days after the start of remediation.

Figure 36 clearly shows the advantages of radiation belt remediation. The remediated case (black line) clears the radiation belts almost an order of magnitude more quickly than natural particle precipitation (blue line). Even with the inclusion of a significant source term, the ES-RBR system is able to reduce the energetic particle population quickly, bringing the energetic particle population below natural levels within 50 days after a large geomagnetic storm. These results are depicted below in Figure 37 through Figure 40 using contour plots to illustrate way the energetic particle population decays with time for both the natural loss case and the ES-RBR case. Figure 37 and Figure 38 start with the current, initial energetic electron flux values and assume a period of minimal solar activity, and therefore no significant geomagnetic storms. The second two figures, Figure 39 and Figure 40, assume a solar active period and include two large scale geomagnetic events.

37. Zheng, Y., A. T. Y. Lui, X. Li, M. C. Fok, Characteristics of 2-6 MeV electrons in the slot region and inner radiation belt, *J. Geophys. Res.*, 111, A10204, 2006.



**Figure 37.** Electron fluxes in the inner belt during a solar quiet period, without remediation.



**Figure 38.** Electron fluxes in the inner belt during a solar quiet period, with ES remediation.

SAMPEX data for the spring 2001 solar storm was also used to compare the effects of radiation belt remediation with natural particle decay after a large injection of energetic particles. Figure 41 shows the actual SAMPEX data for the storm and the following particle decay. Figure 42 illustrates the impact that a constellation of 25 tethers would have on the 2001 solar storm. In Figure 41 the contour lines are in log flux. The initial particle fluxes are lower compared with Figure 39 and Figure 42 because the SAMPEX data measure 2-6 MeV electrons, while the model addresses flux values for > 1 MeV electrons.

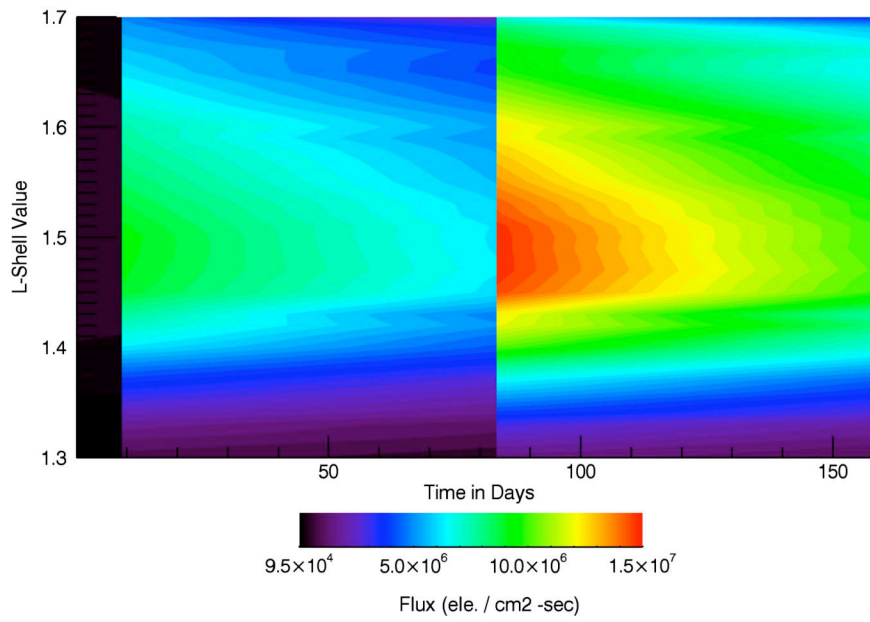


**Figure 39.** Electron fluxes in the inner belt during a solar active period, without remediation.

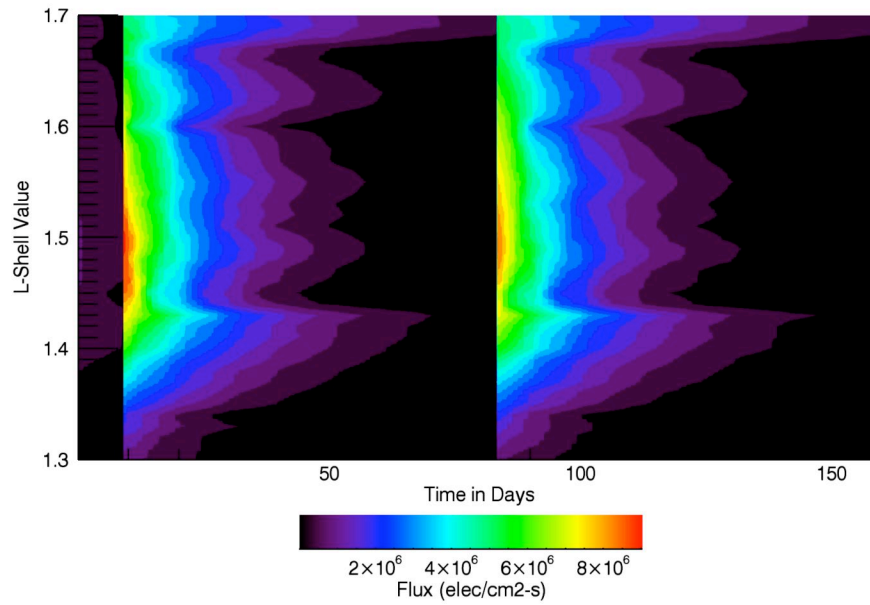


**Figure 40.** Electron fluxes in the inner belt during a solar active period, with ES remediation.

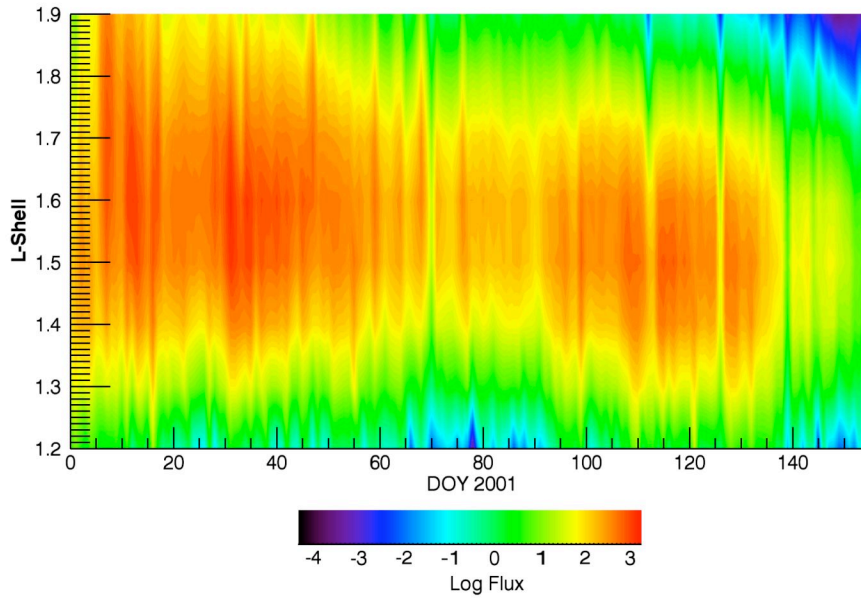


**Figure 41.** Electron fluxes in the inner belt measured by SAMPEX during the Spring 2001 storm.

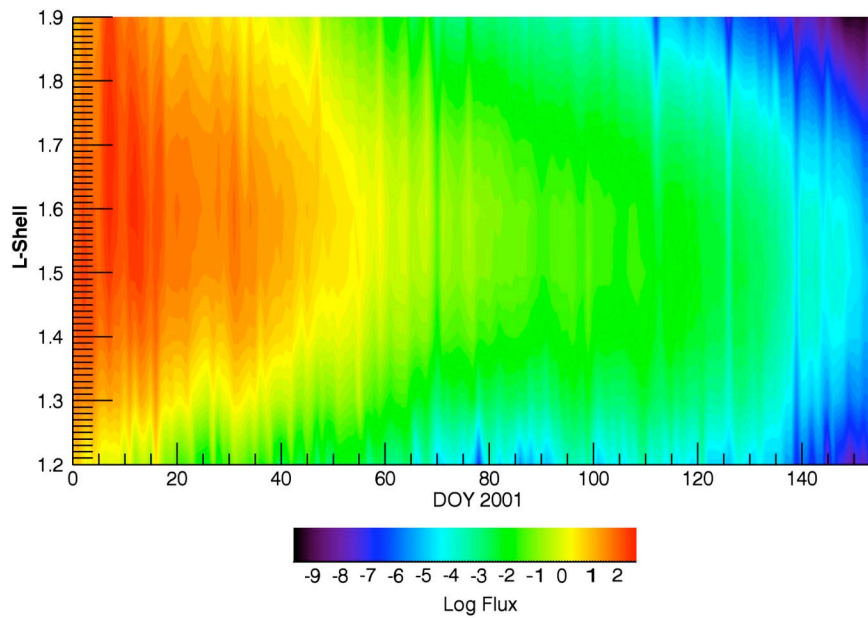


**Figure 42.** Electron fluxes in the inner belt during the Spring 2001 storm, with ES remediation. (note color scale is different than in Figure 41)

### VIII.C. Proton Decay Rates

The decay rate of protons in the radiation belts is calculated for 23,000 time steps. Each time step was 6000 seconds compared to the electron case where each time was 600 seconds. This time step was increased due to the much slower decay of radiation belt protons. Results for the remediation of energetic protons in the radiation belts are plotted in Figure 43; these results do not include the natural source and sink terms.

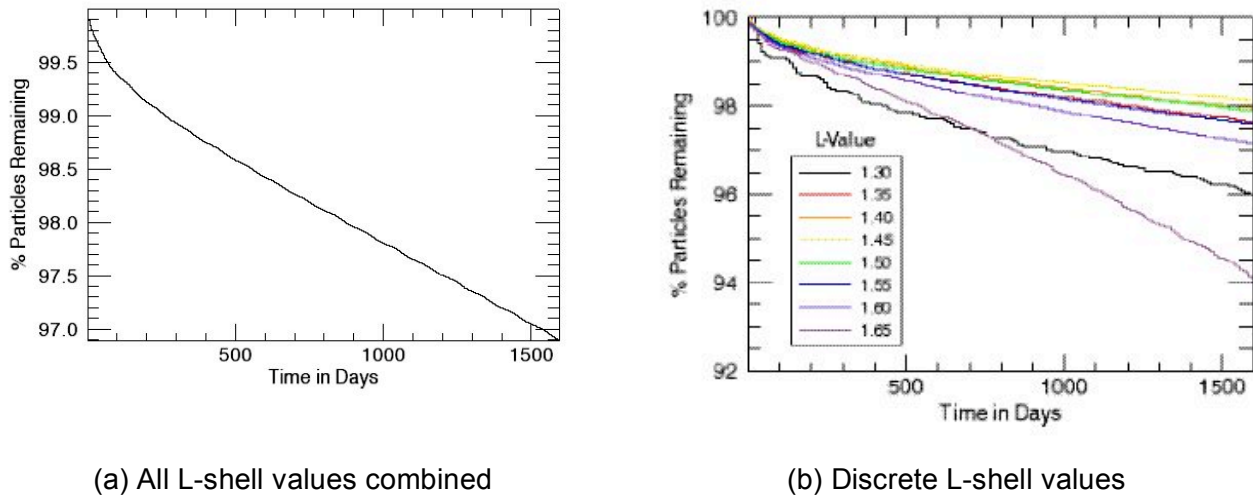


**Figure 43.** Decay of protons in the inner belt region ( $L=1.3$  to  $1.7$ ), with ES remediation but no source or sink terms.

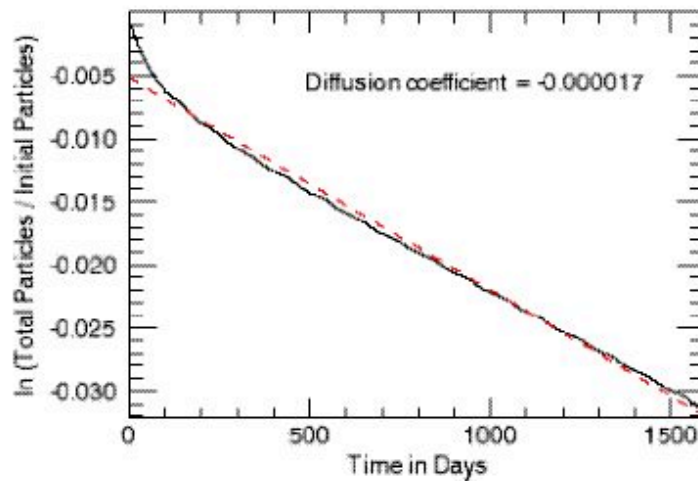
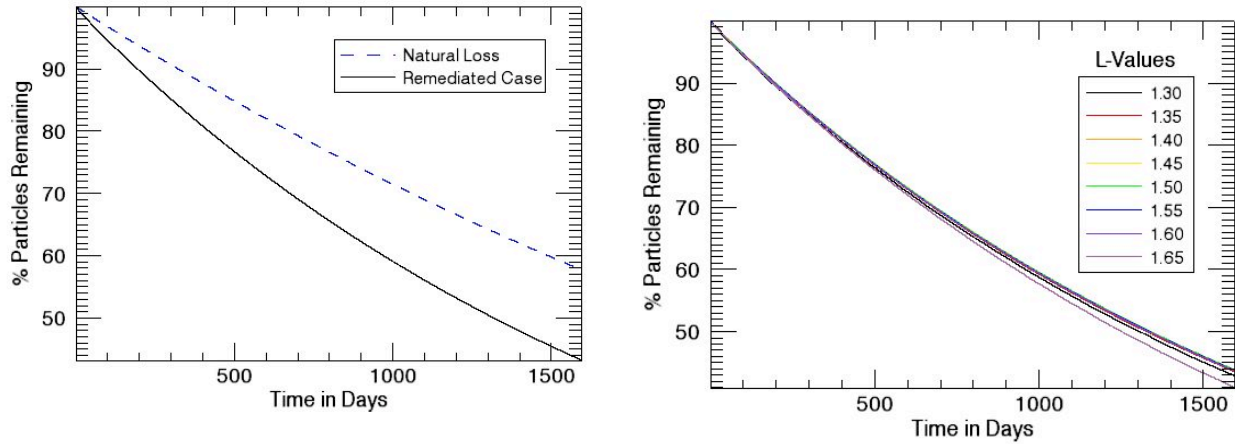


**Figure 44.** Linear least-squares fit (red dashed line) for the decay of energetic protons in the radiation belts.

A natural sink term was then added in the same manor as described in the electron section. For a 10 MeV proton the average particle lifetime in the radiation belts is  $1.7 \times 10^8$  seconds or  $\sim 5$

years.<sup>38</sup> The plots in Figure 45a show the decay rate for energetic protons trapped in the inner radiation belts for particle decay resulting from natural sinks (blue dotted line) and for particle decay due to RBR effects (black solid line). In Figure 45 and Figure 46, an energetic particle source term has not been included.



(a) All L-shell values combined

(b) Discrete L-shell values

**Figure 45.** Decay rate for protons (L=1.3 to 1.7) during solar quiet periods, natural sink terms included.

Using a linear least squares fit, a diffusion coefficient  $\gamma$  was obtained for both the natural loss case and the radiation belt remediation case. Figure 46 illustrates the slight increase in proton precipitation using a radiation belt remediation system. The natural loss diffusion coefficient is  $\gamma = -0.000034 \text{ days}^{-1}$  (blue line) while the diffusion coefficient due to a tether-based radiation belt remediation system is  $\gamma = -0.00052 \text{ days}^{-1}$  (black line). These results suggest that while a constellation of orbiting tethers has tremendous potential for effectively remediating Earth’s natural electron radiation belts, the protons in the radiation belts might be more difficult to remediate.

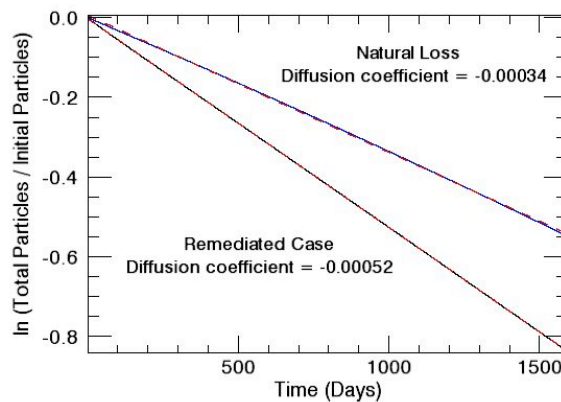


**Figure 46.** Linear Least Squares Fit (red dashed line) for the Decay of Protons in the Radiation Belts due to Natural Loss (blue line) and Remediation (black line).

38. Hess, W. N., The Radiation Belt and Magnetosphere, Blaisdell Publishing Company, Waltham, Massachusetts, 1968.

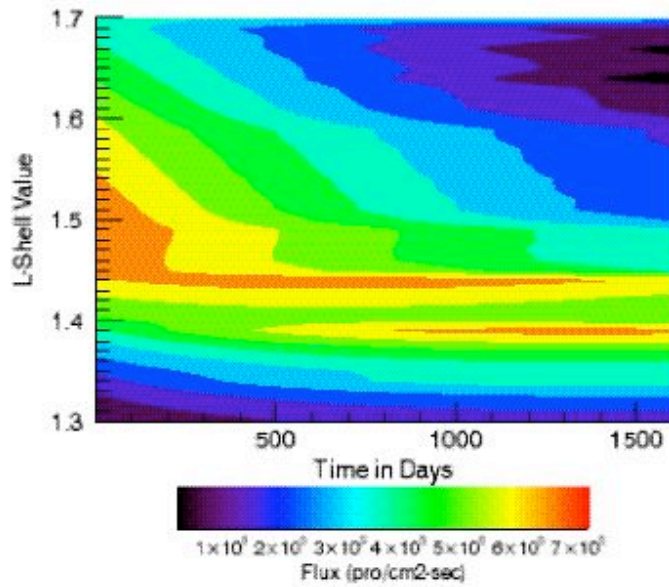


Figure 47. Proton fluxes in the inner belt region during solar quiet period, with no remediation.

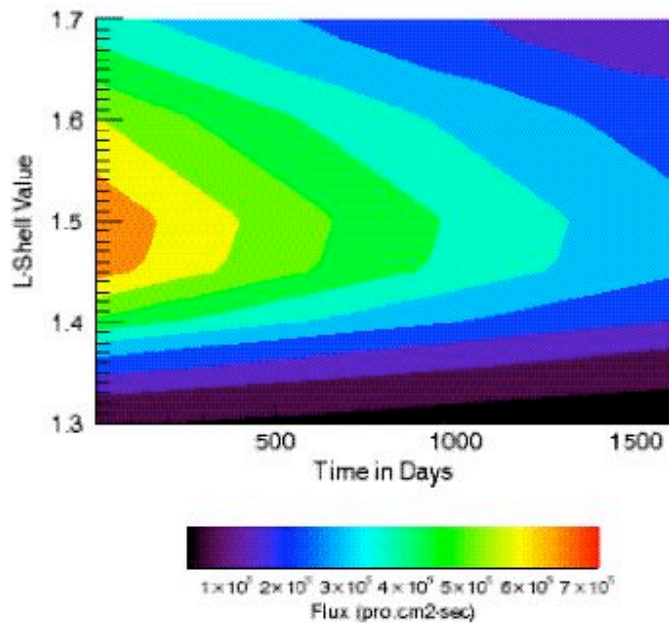


Figure 48. Proton fluxes in the inner belt region during solar quiet period, with ES remediation.

## IX. EVALUATION OF ENVIRONMENTAL EFFECTS OF ELECTROSTATIC REMEDIATION OF THE INNER ELECTRON BELT

The Van Allen Radiation Belts contain high-energy electrons and ions trapped by Earth's magnetic field. These energetic particles present a hazard to both human and robotic missions in Earth's orbit, degrading electronics and materials in spacecraft systems and causing biological damage in humans. Shielding spacecraft against intense Van Allen radiation is a major contributor to the high costs currently associated with space exploration and development. In order to mitigate these risks and costs, several efforts have been proposed to dramatically reduce the radiation fluxes in the Van Allen belts.

While the benefits of radiation belt remediation are apparent, a thorough investigation of possible deleterious effects must be undertaken before initiating any human control over the Earth's natural radiation belts. Here, we evaluate the potential consequences of using a system of multiple long, high-voltage tether structures to remediate the Earth's natural radiation belts. We consider effects both from increased particle precipitation during the initial period of remediation as well as possible adverse repercussions of a significantly reduced radiation belt.

### IX.A. Increased Particle Precipitation

The dumping of high-energy relativistic particles into Earth's atmosphere will increase energetic particle precipitation, resulting in ionization changes in the ionosphere. Enhanced particle precipitation can affect atmospheric chemistry and disrupt radio communications. In order to predict the magnitude and duration of such aftereffects, one must a) consider the characteristics of the remediation system to be used, b) determine the resulting particle precipitation rate produced by remediation efforts, c) compare the calculated remediation flux to the natural rate of particle precipitation, and d) evaluate the significance of the resultant environmental effects.

#### *Electrostatic Tether System Configuration*

In this analysis, we assume an electrostatic tether radiation remediation system composed of several long tether structures in low-inclined orbits. Each tether structure consists of multiple small wires distributed uniformly around a large-diameter cylinder. The wires are charged to a large negative voltage relative to the local quiescent plasma potential, creating an intense electric field around the tether with a nominal sheath radius between 10 and 200 m. The tether systems envisaged range in length from 10 to 100 km, and multiple tether systems would be used to create a constellation of orbiting electrostatic tethers.

For the initial calculations, a constellation of 25 tether systems was used. The tether systems are 100 km long and consist of a 20-m radius ring containing 25 evenly spaced, 50- $\mu\text{m}$  wires each with a surface potential of -100 kV. In order to effectively cover the region of the Van Allen belts to be remediated, the electrostatic tether systems are assumed to orbit with an inclination of  $8.7^\circ$ , a perigee of 2000 km, and an apogee of 4400 km. The tether's orbital position during the course of a year was obtained using the orbital generator on ESA's Space Environment Information System (SPENVIS) website<sup>39</sup>. Coordinates were calculated at 60-second intervals for five 4-day segments, the maximum segment length allowed by the SPENVIS orbital

---

39. [www.SPENVIS.com](http://www.SPENVIS.com)

generator. Segments were calculated at one-month intervals to obtain a variety of orbital coordinates. The input parameters for the electrostatic tether systems are listed in Table 1.

**Table 9.** Tether Constellation and Orbital Input Parameters

Tether systems in orbit	$N_T = 25$	Apogee	4400 km
Length of each tether	$L_T = 100$ km	Perigee	2200 km
Wire radius	$\rho_w = 50$ $\mu$ m	Inclination	8.70°
Radius of tether ring	$\rho_R = 20$ m	Ascending Node	339.20°
Sheath radius	$\rho_{sheath} = 100$ m	Eccentricity	0.11
Wire voltage	$\Phi_w = -100$ kV	Period	2.59 hrs

The calculated orbital coordinates were input into the ESA-SEE 1<sup>40</sup> and the AP-8<sup>41</sup> models to obtain the trapped electron and proton fluxes for each time step along the tether orbit. Particle flux values were obtained for 30 energy values ranging from 0.04 to 7 MeV for electrons and from 0.1 to 400 MeV for protons. Initially, we only consider electron fluxes for particles with energies >0.30 MeV. The orbits of the tethers span L-shells from 1.27 to 1.83; only when a tether is in the region of interest (1.3-1.7) are the particle-tether interactions calculated.

### Tether Induced Particle Precipitation

The increase in energetic particle precipitation is calculated over a 26-hour remediation period (10 orbits) for L-shells ranging from  $L = 1.30$  to  $1.70$  with a step size of 0.01 between L-values. For each 60-second interval during the 26 hours, the tether is associated with one of the 41 L-shells. The average particle precipitation flux for each L-shell is computed by determining 1) the rate at which radiation belt particles interact with the tether, 2) the change in pitch angle that results from tether-particle interactions, 3) the number of particles lost to the atmosphere in a given time period, and 4) the resulting flux observed at an altitude of 100 km.

### Interaction Rate

The percentage of particles interacting with the tether for a given time step and L-value is determined by multiplying the number of particles that interact with the tether in a 1-cm<sup>2</sup> equatorial flux tube (obtained using SPENVIS data) by the ratio of the tether interaction cross-section area,  $A_T$ , to the cross-sectional area of the equatorial radiation belt at the given L-shell,  $A_{RB}(L)$ .

$$A_T = N_T (2\rho_{sheath} L_T) \quad (IX.1)$$

$$A_{RB}(L) = \pi \left[ (R_E (L + 0.01))^2 - (R_E L)^2 \right] \quad (IX.2)$$

40. Vampola, A. L., Outer Zone Energetic Electron Environment Update, Final Report of ESA/ESTEC Contract No. , 1996.

41. Sawyer, D. M., and J. I. Vette, AP-8 Trapped Proton Environment for Solar Maximum and Solar Minimum, NSSDC/WDC-A-R&S 76-06, 1976.

Input parameters for Eqn. (IX1) are listed in Table 1. In Eqn. (IX2),  $R_E$  is the radius of the Earth and  $L$  is the L-shell value. By multiplying the number of particle-tether interactions for one  $1\text{-cm}^2$  flux tube by the ratio of the tether's area to the cross-sectional area of the given L-shell, we can obtain an average number of interactions in that L-shell per unit time.

### Pitch Angle Scattering

For each interaction with a high-voltage tether structure, particles experience a change in pitch angle. These small changes in pitch angle cause particles to randomly walk into the loss cone, where they are removed from the radiation belts via collisions with atmospheric particles. To accurately model particle scatter into the loss cone and the resulting precipitation, each electron within the flux tube is assigned a pitch angle value, and the change in pitch angle is computed and recorded for each particle encounter with the tether system. Electrons are randomly assigned an initial pitch angle value  $\alpha$  in the range

$$\alpha_{Loss} \leq \alpha \leq (\pi - \alpha_{Loss}) \quad (IX.3)$$

where  $\alpha_{Loss}$  is the loss cone value for particles at the given L-shell. For each step, particles interacting with the tether are assigned a change in pitch angle  $\Delta\alpha$  according single event scattering results obtained using the model presented by Minor.<sup>15</sup> The mean and standard deviation for  $\Delta\alpha$  are computed for  $E = 0.3$  MeV and for L-shell values of 1.3, 1.4, 1.5, 1.6, and 1.7. Once determined, the change in pitch angle is added to the initial pitch angle value of the interacting particle; any particles scattered into the loss cone, represented by

$$\alpha \leq \alpha_{Loss} \quad \text{or} \quad \alpha \geq (\pi - \alpha_{Loss}), \quad (IX.4)$$

are considered lost to the atmosphere and are removed from the system. The pitch angle values of the remaining particles are stored and used for the next tether encounter with the given flux tube. The number of particles lost to the atmosphere are counted and recorded for each time step.

### Precipitation Rate

The flux of precipitating energetic particles resulting from the presence of a tether system can be described in two ways: the localized enhanced flux at a tether's 100 km footprint, the location at an altitude of 100 km that maps back to the tether along a magnetic field line; the increase in flux averaged over an L-shell ( $L$  to  $L+0.01$ ) for all 25 tether systems in the constellation. Both the localized and average flux enhancements are computed over the course of 10 orbits (~26 hours) during the remediation period. Values represent the mean enhancement flux during this 1-day period.

The localized flux enhancement describes the increase in particle precipitation in the region directly below the tether, along a magnetic field line, at an altitude of 100 km. These values account for magnetic focusing and represent the maximum fluxes observed during the initial 10 orbits of remediation. In order to compute the precipitation flux at an altitude of 100 km, the equatorial precipitation rate, which was calculated above, is multiplied by the ratio of the magnetic field magnitude at 100 km,  $B_{100km}$ , to that at the equator,  $B_{eq}$ ,

$$\Phi_{100km} = \Phi_{eq} \left( \frac{B_{100km}}{B_{eq}} \right). \quad (IX.5)$$

At the latitude where the field line intersects the upper atmosphere  $\lambda_{100km}$ , the magnitude of the magnetic field is calculated using the following equations:<sup>42</sup>

$$B_{100km} = -B_{eq} \left( 2\hat{r} \cos \lambda_{100km} + \hat{\Theta} \sin \lambda_{100km} \right) (1/L)^3 \tag{IX.6}$$

$$\lambda_{100km} = \sin^{-1} \left( \frac{1}{\sqrt{L}} \right). \tag{IX.7}$$

This provides the precipitation flux at the top of the atmosphere for one tether system. Precipitation flux values are calculated at each L-shell and plotted in Figure 49. Note that since this graph depicts the localized increase in flux, at any given time only 25 locations above the Earth would experience an increase in particle precipitation of these magnitudes. The peak precipitation would occur at L=1.43 with a flux of  $2.0 \times 10^6$  electrons/s/cm<sup>2</sup>.

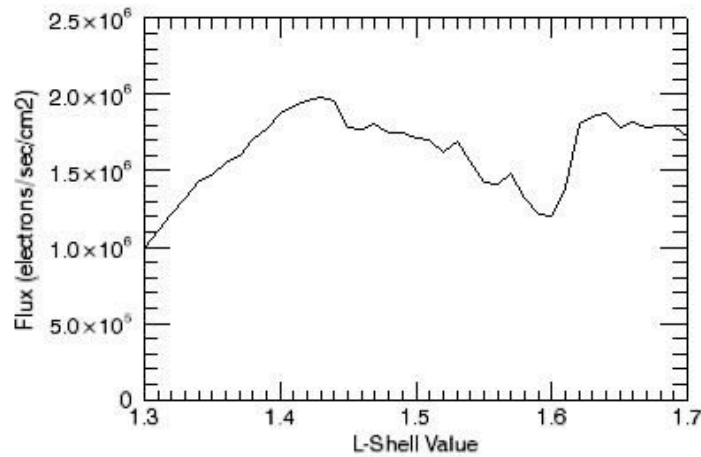


**Figure 49.** Localized increase in precipitation flux resulting from initial radiation belt remediation.

The average precipitation enhancement for each L-shell is calculated assuming a constellation of 25 tether systems. As with the localized enhancement, flux values are computed for a total of 10 orbits. During this ~ 26-hour period, the total number of particles scattered into the loss cone are summed for each L-shell. To obtain flux of deposited particles, the total number of particles lost in a given L-shell is divided by the cumulative time the tether systems spend in that L-shell and the area of the given L-shell (L to L+0.01). Values are then scaled to account for magnetic focusing as described above. Figure 50 shows the L-shell averaged particle enhancement flux for the initial day of remediation.

42. Schulz, M., Lanzerotti, L.J., *Particle Diffusion in the Radiation Belts*, Chapter 1: Adiabatic Invariants and Magnetospheric Models, Springer-Verlag, New York, 1974.

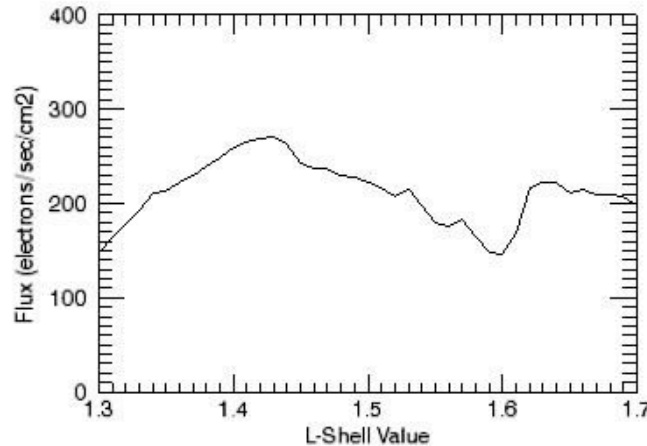


**Figure 50.** Increase in precipitation flux averaged over 26 hours and L-shell area resulting from initial radiation belt remediation.

#### *Natural Particle Precipitation Rate*

In order to determine the impact that the additional, tether-induced, particle precipitation has on the atmosphere, we compare the loss resulting from the tether systems to the natural precipitation flux. To do this, we use data collected by the second-generation Space Environment Monitor (SEM-2) onboard the NOAA Polar Orbiting Environmental Satellite (POES)<sup>§</sup>. The POES satellite, which orbits the Earth in a polar, sun-synchronous orbit at about 800 km altitude, contains a Medium Energy Proton and Electron Detector (MEPED) that monitors the intensities of charged particle radiation at high energies.

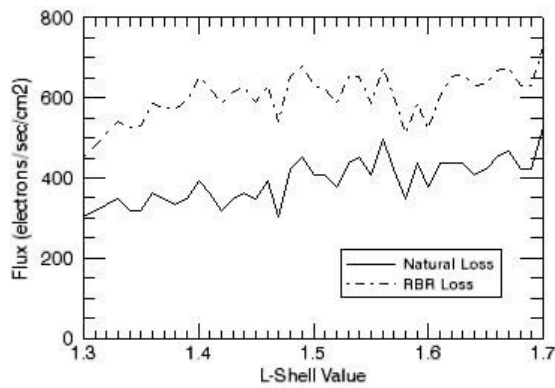
Two identical electron telescopes are included on the SEM-2: a 0° electron detector that observes along the Earth-center-to-satellite vector, and a 90° detector that observes in a direction perpendicular to the 0° detector. Precipitating electrons are monitored by the 0° detector when the satellite is pole-ward of approximately 35° geographic latitude and by the 90° detector when the satellite is at lower geographic latitudes. The electron telescopes measure energetic electron data for three energy ranges: 30 – 1100 keV, 100 – 1100 keV, and 300 – 1100 keV. POES data are given in 16-second time intervals from July 1998 to the present.

In our computations, data from the 0° detector 300 – 1100 keV channel was used for L-shell values  $\geq 1.50$ , and data from the 90° detector 300 – 1100 keV channel was used for L-shell values  $< 1.50$ . To construct a median baseline plot of precipitating electrons in the region from L=1.3-1.7, we randomly selected 12 days worth of data spanning the range of months and years for which POES data is available. The selected days are listed in Table 2. For each of these days, the median precipitation flux was computed for each L-value. The median was used instead of the mean due to occasional extremely large values, which could possibly represent cosmic ray impacts or other anomalies. The median flux values for each of the 12 days were then averaged to obtain the baseline precipitation flux as a function of L-value (Figure 51, solid line).

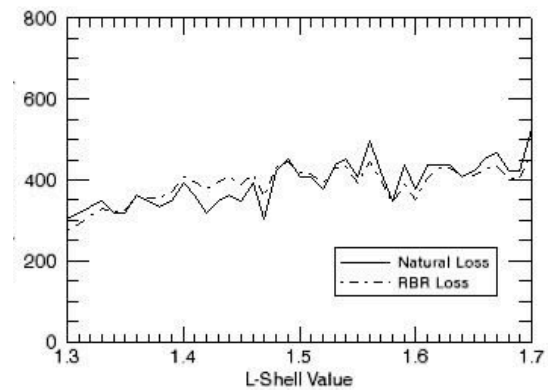
§. [http://www.ngdc.noaa.gov/stp/NOAA/noaa\\_poes.html](http://www.ngdc.noaa.gov/stp/NOAA/noaa_poes.html)

**Table 10..** NOAA data used for baseline precipitation flux

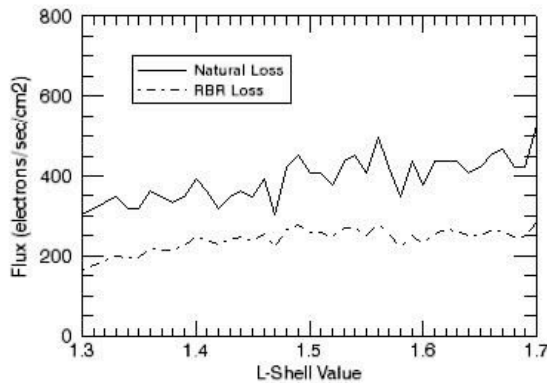
Day	Satellite
Jan. 6, 2000	NOAA-15
Aug. 6, 2000	NOAA-15
Nov. 29, 2001	NOAA-16
July 25, 2002	NOAA-17
Jan. 13, 2003	NOAA-16
Jan. 20, 2004	NOAA-16
Mar. 13, 2005	NOAA-16
Apr. 29, 2005	NOAA-16
June 13, 2005	NOAA-18
June 22, 2005	NOAA-18
Jan. 11, 2006	NOAA-18
Jan. 12, 2006	NOAA-15



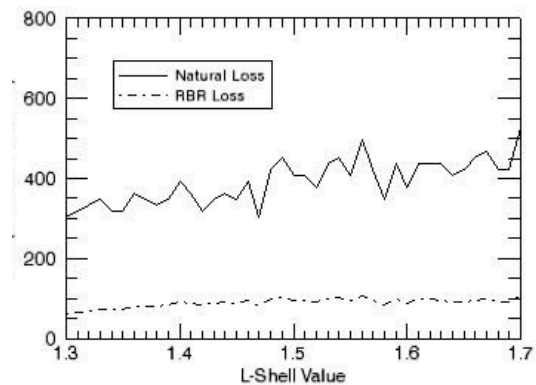
(a) Time = 0 days



(b) Time = 50 days



(c) Time = 100 days



(d) Time = 200 days

**Figure 51.** Natural precipitation flux (solid line) and combined precipitation flux (dotted line) plotted at four times during initial radiation belt remediation.

Once the natural flux of precipitating particles is determined, we can plot the combined precipitation flux, the flux resulting from remediation added to the natural particle flux, as a function of L-shell for different times after the beginning of remediation (Figure 51, dotted line). The baseline precipitation flux has been plotted on the same graph for comparison (Figure 51,

solid line). During the early stages of remediation, the combined precipitation flux is large than the natural levels, however, with time the remediated precipitation flux is reduced to a value below the current flux levels.

To determine the point at which the flux from the remediated system dropped below the typical value, we plot the decaying precipitation flux as a function of time (Figure 52). The natural particle loss for each flux tube is shown with a solid line and the combined remediated flux is drawn with a dotted line. At an L-value of 1.30 it takes just under 50 days for the RBR flux to drop below the current levels. At  $L = 1.50$ , it only takes  $\sim 30$  days.

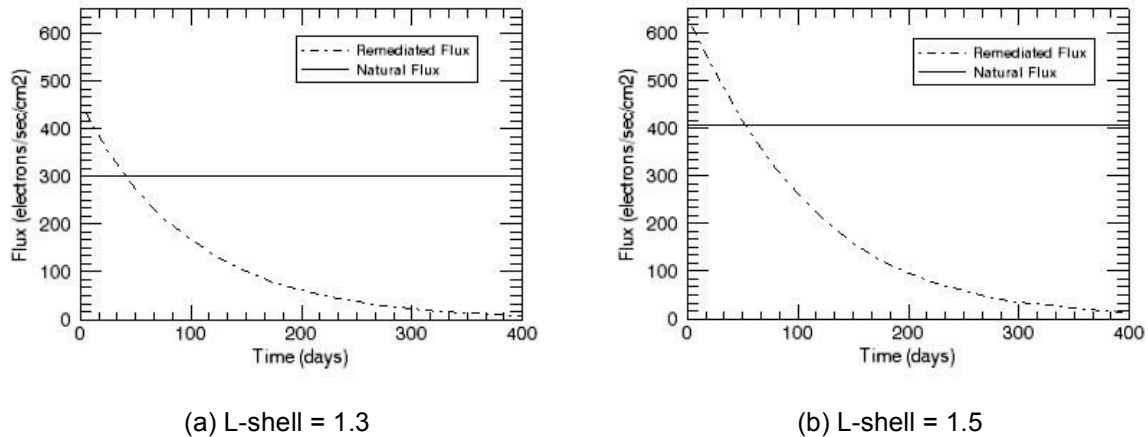


**Figure 52.** Decay of particle precipitation flux with time (dotted line) during radiation belt remediation for two L- values. The current, natural radiation belt precipitation flux is plotted with a solid line.

The flux drops below the typical value, on average, after about 40 days. After 60 days, the precipitating flux at all L-shell values has dropped below the ambient conditions. The flux at higher L-shells drops below the current precipitation flux first, and L-shell values between 1.4 and 1.5 are last to reduce the precipitation flux value below typical levels.

### Analysis of Environmental Effects

Even during the initial remediation period, the average change in precipitating flux is minimal compared to the natural level. The change in flux ranges from 35% to 85% of the typical, natural precipitation flux (Figure 53). These values are insubstantial when compared to Rodger *et al.*<sup>43</sup>, a recent paper exploring the atmospheric implications of radiation belt remediation after a theoretical high altitude nuclear explosion (HANE). In the case of a HANE event, the flux of precipitating energetic particles would be 1000 times greater than current conditions. While our increased precipitation values would not be as drastic as a HANE, some atmospheric effects could be similar to those discussed by Rodger *et al.* One possible atmospheric effect of RBR is neutral chemistry changes leading to  $\text{NO}_x$  enhancements and  $\text{O}_x$  depletions. For the case of HANE remediation, Rodger *et al.* found atmospheric changes to be significant during the period of precipitation, but they do not generally persist for a long duration. The magnitudes, time-scales, and altitudes of these changes were reported to be no more significant than those

43. Rodger, C.J., Clilverd, M.A., Ulich, Th., Verronen, P.T., Turnen, E., and N.R. Thomson, The atmospheric implications of radiation belt remediation, *Ann. Geophys.*, 24, 2025-2041, 2006

observed during large solar proton events. Rodger *et al.* also conclude that RBR operations would lead to unusually intense high-frequency (HF) blackouts for about the first half of the operation time, producing large-scale disruptions to radio communications and navigation systems.

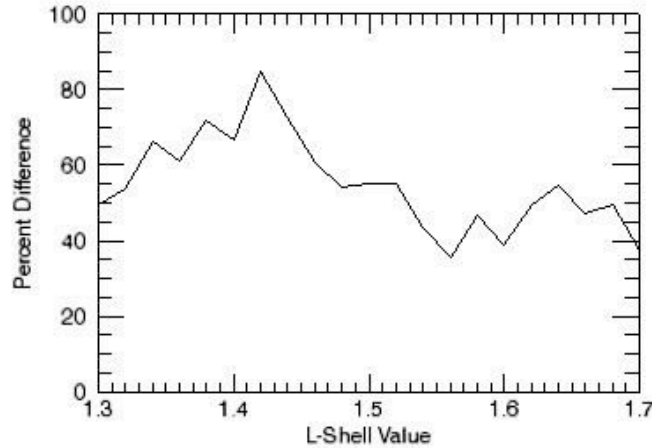


**Figure 53.** Percent change in L-shell averaged precipitation rate for initial radiation belt remediation.

Unlike Rodger *et al.*, who consider a greatly enhanced radiation belt population after a HANE event, we address remediation of a nominal natural energetic particle population in the radiation belts. The fluxes we expect are orders of magnitude smaller and our remediation time-scale is approximately 30 and 300 times longer than those considered by Rodger *et al.* They found that the HF disruption stopped having any significant effects about 80% of the way through the dumping time (either 1 day or 10 days), at which point, the 1 MeV population was roughly back to normal and only extremely energetic particles remained from the HANE event. Given the order of magnitude smaller fluxes we are considering in this study, the increased precipitation flux due to radiation belt remediation should not inflict any important or significant changes to atmospheric chemistry or communication disturbances.

To put the significance of the atmospheric effects of remediation in context, we compare the increase in precipitation flux to a solar flare event by determining the solar flare equivalent size of such an increase in particle flux. Solar flares are classified as A, B, C, M or X according to the peak flux in watts per square meter, W/m<sup>2</sup>. Each class has a peak flux ten times greater than the preceding one with nine subclasses ranging from 1 to 9 on a linear scale. X-class flares, which have a peak flux of order 10<sup>-4</sup> W/m<sup>2</sup>, are major events that can trigger planet-wide radio blackouts and long-lasting radiation storms. M-class flares are medium-sized and can cause brief radio blackouts that affect Earth's polar regions. C-class flares are small compared to X- and M-class events and result in few noticeable consequences on Earth. B- and A-class events are extremely small events with no noticeable consequences on Earth.

The peak localized change in flux during the initial period of RBR is  $\sim 2 \times 10^6$  electrons/sec/cm<sup>2</sup> (Fig 1). Assuming  $> 0.3$  MeV electrons,\* this gives a peak flux of  $9.6 \times 10^{-4}$  W/m<sup>2</sup>

\*. The convention is to measure the peak flux in the wavelength region 1 to 8 Å, however, we are currently considering particles with energies  $> 0.3$  MeV and wavelengths  $< 0.04$  Å.

corresponding to a X9 flare. However, if this is just for the region in a tether's magnetic footprint. When we consider the average flux over an L-shell, the peak average flux is  $1.3 \times 10^{-7}$  W/m<sup>2</sup>. This corresponds to a B1 type solar flare, which results in no noticeable consequences. If we consider the flux of particles with wavelength from 1 to 8 Å, the precipitation flux might be larger than for the 0.3 MeV case; however, the much lower energies of the particles (2 to 20 eV) will result in an even smaller peak flux (in W/m<sup>2</sup>).

#### Effects of Significantly Reduced Radiation Belt Fluxes

The effects of a significantly reduced radiation belt remain unclear. A few scientists theorize that the Van Allen belts offer some protection against solar wind, suggesting that a weakening of the belts could result in unforeseen harm to life on Earth if increased solar radiation reached Earth's surface. The radiation belts may influence the Earth's telluric current, which means that dissipating the belts could influence the behavior of Earth's magnetic poles. There is also a correlation between lightning events and particle precipitation; however, it is unknown how the reduction of the Van Allen belts will influence the global atmospheric circuit. More research into the planetary and biological effects of radiation belts are needed before much can be said with certainty regarding the potential deleterious effects of significantly reduced radiation belts.

#### **IX.B. Summary of Environmental Impact Assessment**

Analysis of the precipitation of energetic electrons from the Van Allen radiation belts into the upper atmosphere as a result of radiation belt remediation using a constellation of 25 100-km long electrostatic tether systems indicates that the precipitated flux is enhanced by a factor of less than two at the beginning of the remediation process, and will drop to natural levels within about two months. The anticipated secondary effects of this precipitation, including upper atmospheric NO<sub>x</sub> enhancement and high-frequency disruptions, will be short-lived and mild, less than a small solar flare event.

## X. TECHNOLOGY DEVELOPMENT AND VALIDATION PLAN

Before an Electrostatic Radiation Belt Remediation system could be fielded, several tests must be performed to verify the validity of the models used in predicting the potential performance of the system. Additionally, several key technologies must be developed.

### X.A. Model Uncertainties

Because the number of ES-RBR systems required to remediate a radiation belt is so strongly dependent upon the radius of the high-voltage sheath that develops around it in the plasmaspheric plasma, as expressed by Eqn. IV.26, the size and internal structure of the sheath created by the proposed multi-wire structure is critical to the feasibility of the concept. The most significant concern with regards to the multi-wire sheath size is the potential for the non-axisymmetric field created by the multiple-wire geometry to deflect infalling ions into trajectories that orbit within the sheath for a long duration before they either impact a wire or are kicked back out to the sheath edge. If a significant portion of ions that enter the sheath spend a long duration within the sheath, they will increase the charge density within the sheath, resulting in a significant reduction in the sheath radius. Due to the extreme computational cost of properly simulating just a single wire's sheath, determining whether this 'semi-trapping' of ions within the multi-wire sheath occurs and results in significant reductions in sheath size below the levels predicted by the models used herein will be most efficiently performed through experimentation.

### X.B. Phase A: Verification of Multi-Wire Sheath Potential Structure Model

Accordingly, the next step in the development of the ES-RBR concept should be testing to characterize the size and structure of a plasma sheath around a high-voltage multi-wire structure. Unfortunately, although it is possible to identify the location of the edge of the plasma sheath around a high-voltage object using standard Langmuir plasma probe techniques, measuring the potential within a high-voltage sheath using such probes is not possible. This is because plasma probe techniques rely upon the assumption of quasi-neutrality of the plasma near the probe. Within a high-voltage structure's sheath, the strong electric fields expel nearly all electrons from within the sheath, and thus the sheath region is far from quasi-neutral.

One method that could measure the internal potential structure of a multi-wire plasma sheath is electron-beam tomography, as illustrated in Figure 54. An multi-wire structure would be placed in a vacuum chamber, and immersed in a plasma generated by a hollow cathode device or other plasma source. The structure would then be biased to a large negative voltage, on the order of 10-20 kV. An electron beam with energies comparable to the bias potential on the structure would then be transmitted through the plasma sheath. On the other side of the electrostatic structure, a receiver, such as a

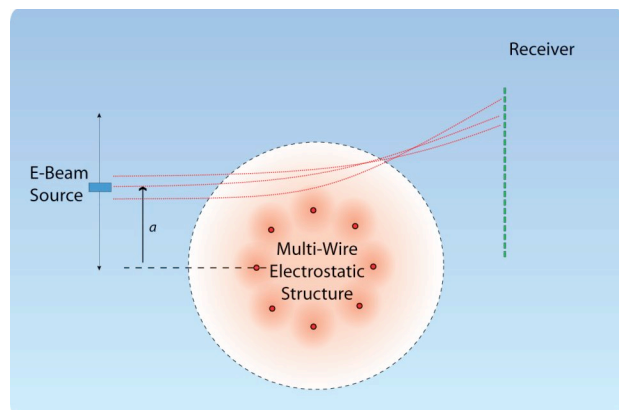


**Figure 54.** Concept for electron-beam tomography method to determine the potential structure inside a multi-wire electrostatic structure's plasma sheath.

segmented array of anodes, would be used to measure the deflection of the electron beam. By scanning the beam across the span of the sheath and observing the variation of deflection with the ‘impact parameter’  $a$ , sufficient information can be gathered to enable reconstruction of the potential structure inside the sheath.

### X.C. Technology Development

Provided the investigations of the high-voltage sheath structure correlate well with the models used to perform the remediation analyses, several key technologies would need to be developed to support electrostatic remediation experiments. The principal components needed would be high-voltage, high-power power supplies suitable for use in the space environment, a suitable multi-wire tether structure that can be wound onto a spool and later deployed and expanded using electrostatic forces, and a tether deployer designed to handle both the complex multi-wire structure and the very high voltages that must be applied to the tether.

### X.D. Phase B: On-Orbit Demonstration of Electron Precipitation by an Electrostatic Structure

With the technology components listed above, we would then pursue an on-orbit demonstration of precipitation of electrons from the radiation belt using an electrostatic structure. Figure 55 illustrates the CONOPS for a mission called the “Tethered Orbit-Raising and Radiation Remediation QUalification Experiment” (TOR<sup>3</sup>QUE) that could perform this demonstration on a relatively low-cost microsatellite platform. The TOR<sup>3</sup>QUE experiment would use a small launch vehicle, such as a SpaceX Falcon or Orbital Sciences Minotaur rocket to deliver a ~200 kg

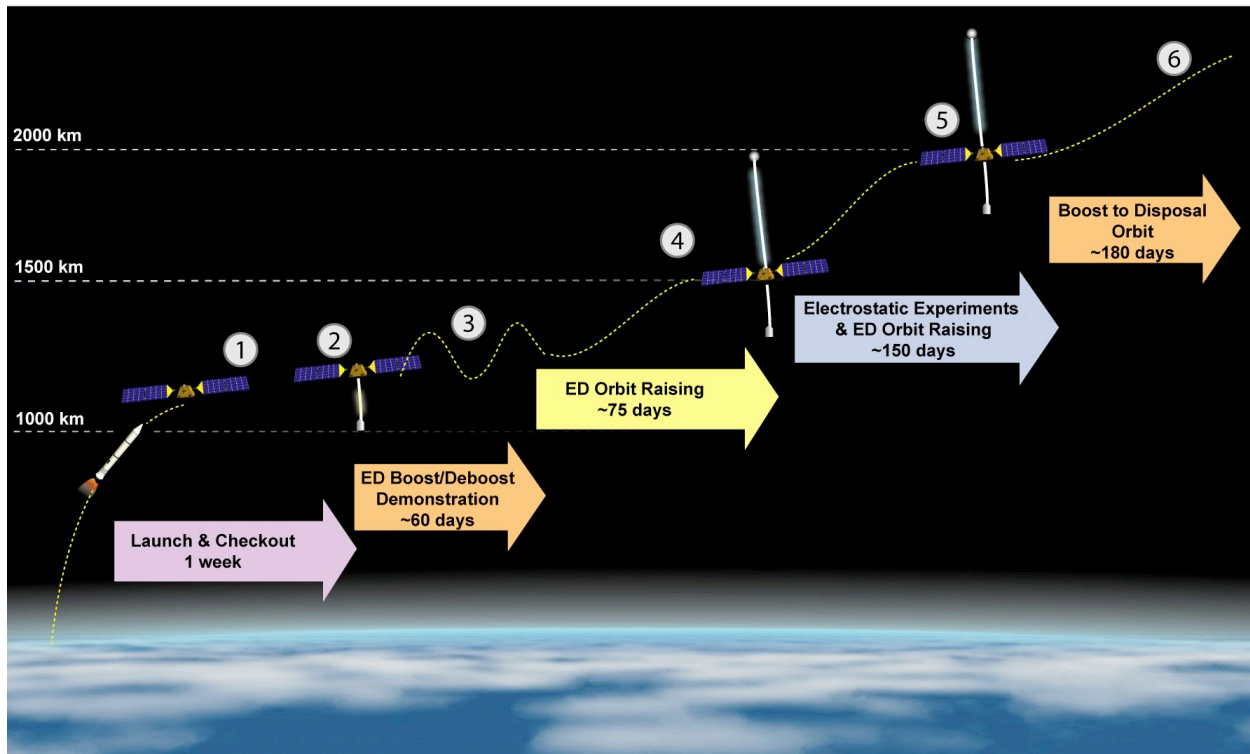


**Figure 55.** Mission concept for a “Tethered Orbit-Raising & Radiation Remediation QUalification Experiment” (TOR<sup>3</sup>QUE).

microsatellite with several hundred watts of power generation capability to a high-LEO orbit. The microsatellite would then deploy a 5-kilometer long conducting tether and use it in an electrodynamic thrust mode to raise its orbit up into the lower portion of the inner electron belt, at between 1500-2000 km altitude. Once it reaches a region of significant electron fluxes, it would deploy a second, multi-wire tether structure and energize it to a large negative potential.

Measuring the effects of a single, small electrostatic structure on the trapped electron fluxes in the inner belt directly would likely be difficult to impossible. However, the Trimpfi effect, illustrated in Figure 56, could provide a means for observing and quantifying the precipitation of electrons out of the belt caused by the electrostatic tether. As discussed in Section IX,

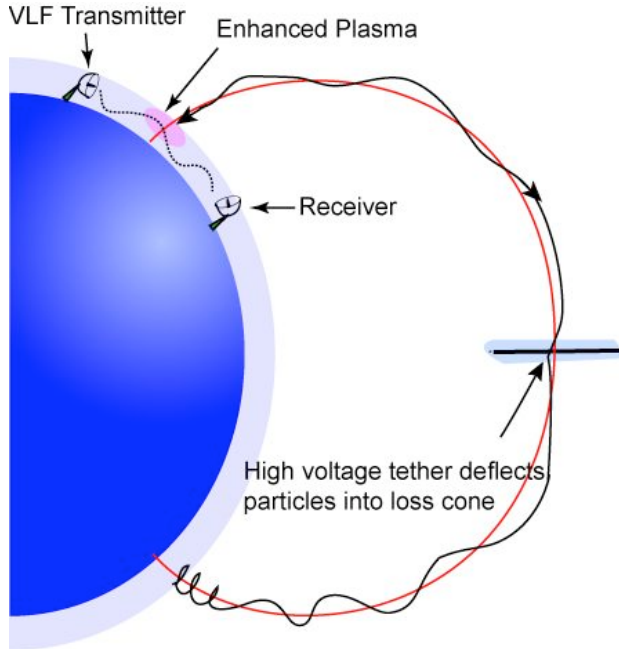


**Figure 56.** Detection of electron precipitation due to an electrostatic tether structure using the TRIMPI effect.

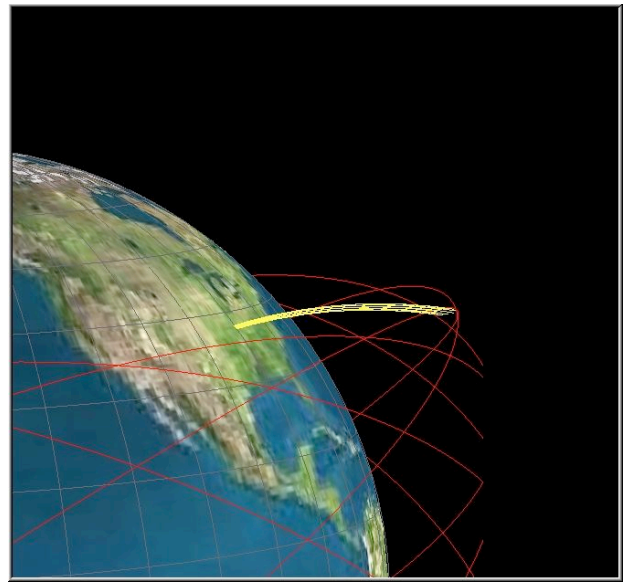


**Figure 57.** Example of a flux tube precipitating electrons will follow after scattering by an ES tether in a 28.5° orbit.

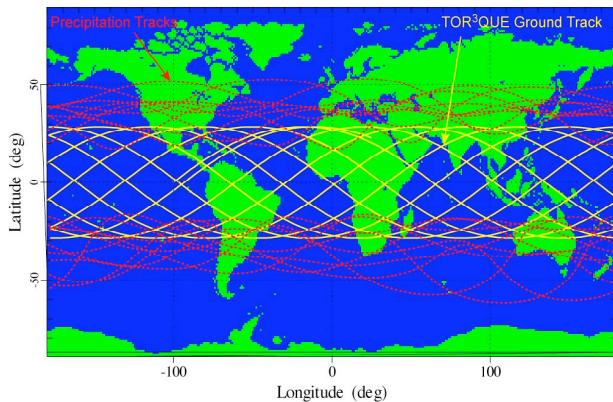


**Figure 58.** Precipitation tracks (red) that would be expected from a tether orbiting in a 28.5° orbit (yellow).

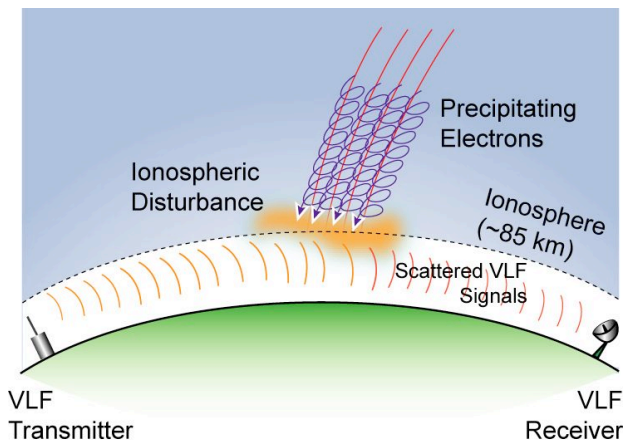


**Figure 59.** Principle of TRIMPI effect detection of electron precipitation

precipitation of electrons into the upper atmosphere will cause enhancement of plasma densities in the D-region. While these enhancements will be too small to be measurable during the daytime, during the nighttime the enhancements can be 10-100x background levels. As illustrated in Figure 57, the electrons scattered by the orbiting tether into the loss cone will follow the magnetic flux tubes down to the upper atmosphere, concentrating in a localized spot. As the tether moves in its orbit, this spot will scan across the surface of the Earth, following ground tracks as illustrated in Figure 58. Thus the precipitating electrons will be a beam of electrons tracing across the night sky leaving a trail of enhanced electron density that will persist for a few seconds, somewhat like an electron beam tracing across a phosphor screen in a CRT. The localized plasma densities caused by this precipitation will cause scattering of very-low-frequency (VLF) transmissions that pass through the disturbance, as illustrated in Figure 59. By observing such scattering using one or more VLF transmitter and several receivers at different locations, and by measuring the intensity of the VLF scattering, the precipitation of energetic electrons by the TOR<sup>3</sup>QUE system could be detected and quantified, providing verification of the feasibility of radiation belt remediation using electrostatic structures.

An additional benefit of this experiment approach is that the high-voltage, high-power microsatellite platform used for the mission could then serve as a flight-qualified building block for the modular system architecture discussed in Section III.A.

## **XI. CONCLUSIONS**

We have utilized both analytical methods and numerical simulations to investigate the feasibility of using long conducting structures biased to high voltages to scatter trapped energetic particles out of the radiation belts of Earth and Jupiter. Both approaches indicate that such remediation is feasible, and the number and size of ‘ElectroStatic Radiation Belt Remediation’ (ES-RBR) systems required to reduce electron fluxes in the Earth’s inner electron belt are both very reasonable. A system composed of 24 spacecraft, each of which has a 100-km long tether structure and a power supply on the order of 5 kW, could dramatically lower the radiation doses experienced by spacecraft and personnel flying in low Earth orbit. Investigation of the potential adverse ‘environmental impact’ of such a radiation belt remediation effort indicate that the anticipated side effects on the ozone layer and RF communications will be very mild and short-lived, comparable to a very weak solar storm. Remediation of the Jovian radiation belts is a much more challenging proposition due to its immense spatial extent, but remediation of a narrow band around one of the Galilean moons, such as Europa, may be feasible with a system composed of 100 ES-RBR spacecraft. Because the models used in these analyses rely upon several assumptions regarding the very complex physics of the high-voltage sheaths that form around a multi-wire tether structure in the presence of a plasma, near-term efforts to advance the technology readiness of this concept should focus upon verification of these assumptions through detailed experimental investigation of the size and structure of plasma sheaths around multi-wire structures. Should these investigations validate the models, the ES-RBR concept can then be demonstrated through a relatively low-cost microsat-class flight experiment that would measure the precipitation of energetic electrons into the upper atmosphere caused by a several-kilometer long high-voltage tether structure. The microsat hardware demonstrated in this flight could then serve as a flight-qualified building block for a modular architecture for constructing the two dozen 100-km long electrostatic structures required for an operational ES-RBR system. By dramatically reducing radiation fluxes in the LEO environment, such an ES-RBR system could enable many spacecraft to be built using lower cost, higher performance components while still providing reliable operations on orbit, and it could reduce health risks for many manned spaceflight missions.